PACKAGING OF RF MEMS SWITCHES AND PERFORMANCE IMPROVEMENT

A THESIS SUBMITTED TO
THE GRADUATE SCHOOL OF NATURAL AND APPLIED SCIENCES
OF
MIDDLE EAST TECHNICAL UNIVERSITY

BY

İLKER COMART

IN PARTIAL FULFILLMENT OF THE REQUIREMENTS
FOR
THE DEGREE OF DOCTOR OF PHILOSOPHY
IN
ELECTRICAL AND ELECTRONICS ENG.

SEPTEMBER 2019

Approval of the thesis:

PACKAGING OF RF MEMS SWITCHES AND PERFORMANCE IMPROVEMENT

submitted by **İLKER COMART** in partial fulfillment of the requirements for the degree of **Doctor of Philosophy in Electrical and Electronics Engineering Department, Middle East Technical University** by,

Prof. Dr. Halil Kalıpçılar
Dean, Graduate School of **Natural and Applied Sciences** ________________

Prof. Dr. İlkay Ulusoy
Head of Department, **Electrical and Electronics Eng.** ________________

Prof. Dr. Şimşek Demir
Supervisor, **Electrical and Electronics Eng., METU** ________________

Prof. Dr. Tayfun Akın
Co-supervisor, **Electrical and Electronics Eng., METU** ________________

Examining Committee Members:

Prof. Dr. Seyit Sencer Koç
Electrical and Electronics Engineering, METU ________________

Prof. Dr. Şimşek Demir
Electrical and Electronics Engineering, METU ________________

Prof. Dr. Özlem Aydın Çivi
Electrical and Electronics Engineering, METU ________________

Assist. Prof. Dr. Mehmet Ünlü
Electrical and Electronics Engineering, TOBB ________________

Assoc. Prof. Dr. Kutay İçöz
Electrical and Electronics Engineering, AGU ________________

Date:

I hereby declare that all information in this document has been obtained and presented in accordance with academic rules and ethical conduct. I also declare that, as required by these rules and conduct, I have fully cited and referenced all material and results that are not original to this work.

Name, Surname: İlker Comart

Signature :

ABSTRACT

PACKAGING OF RF MEMS SWITCHES AND PERFORMANCE IMPROVEMENT

Comart, İlker
Ph.D., Department of Electrical and Electronics Eng.
Supervisor: Prof. Dr. Şimşek Demir
Co-Supervisor : Prof. Dr. Tayfun Akın

September 2019, 115 pages

This dissertation presents a novel zero-level packaging method for shunt, capacitive contact RF MEMS switches where BCB acts as the adhesive interlayer between the cap and device wafers. Initially, the packaging concept is realized for 50 Ω CPW transmission lines. A microwave characterization procedure (circuit modeling) is performed by curve fitting five packaged CPW transmission line performances to the proposed circuit model. The circuit model consists of cascaded transmission line segments, in which lumped capacitances are utilized for modeling the discontinuities in the planar feedthrough regions. The microwave characterization procedure demonstrated 0.1 dB/transition with the implemented packaging approach. Afterward, shunt, capacitive contact RF MEMS switches are packaged by exactly the same package structure. Endurance analysis (shear strength tests), mechanical analysis (optical profiler measurements), actuation analysis (C-V measurements), RF performance analysis (S-parameter measurements), transient analysis (switching-time measurements), and lifetime analysis (lifetime measurements) assessed the overall performance of the BCB packaged RF MEMS switches. The packaging method demonstrated 18.3 MPa average shear strength. One of the five tested switches reached 26.9 MPa, which exceeded the counterpart packaging methods in this regard. Optical profiler measurements of the MEMS bridge before and after the packaging process presented 71 nm average center deflection. Actuation analysis presented consistent results with the optical profiler measurements where the actuation voltages increased 4.2 V in the average during the packaging process. The S-parameter measurements indicated negligible effect on the RF performance of the switch. The return loss and insertion loss at 35 GHz (operating frequency) in the upstate are 28 dB and 0.4 dB, respectively. Moreover, the isolation characteristics indicate 35 dB at 35 GHz for most of the packaged switches. The transient analysis showed 10 μs rise time and 8.5 μs fall time for the packaged RF MEMS switches. Lifetime measurement demonstrates 10.2 billion cycles without failure in the RF performance. A sensitivity analysis based on EM simulations presented the robustness and insensitivity of the package in terms of possible process variations. The dissertation also presents a novel piecewise wideband characterization method based on CPW transmission line measurements to demonstrate the dispersive nature of the utilized glass and high-resistivity silicon wafers.

Keywords: RF MEMS, switch, packaging, BCB, CPW, performance

ÖZ

RF MEMS ANAHTARLARIN PAKETLENMESİ VE BAŞARIM ARTIRIMI

Comart, İlker
Doktora, Elektrik ve Elektronik Mühendisliği Bölümü
Tez Yöneticisi: Prof. Dr. Şimşek Demir
Ortak Tez Yöneticisi : Prof. Dr. Tayfun Akın

Eylül 2019 , 115 sayfa

Bu tez paralel, kapasitif değeçli RF MEMS anahtarlar için, kapak ve bileşen alttaşlarının BCB ile birbirine yapıştırıldığı özgün bir sıfır-seviye paketleme yöntemini sunmaktadır. Paketleme yöntemi ilk olarak 50 Ω EDK hatların paketlenmesi için kullanılmıştır. Önerilen devre modeli ve paketlenen beş farklı EDK hattın ölçümlerinin birbirine uyumlanması ile paket yapısının mikrodalga karakterizasyonu yapılmıştır. Önerilen devre modeli birbirine seri bağlanmış iletim hatlarından oluşmakta olup, EDK üzerindeki düzlemsel geçiş bölgelerindeki süreksizlikleri modellemek için parazitik kapasitanslar kullanılmıştır. Mikrodalga karakterizasyon sonuçları her bir düzlemsel geçişin RF MEMS anahtarın toplam araya girme kaybına 0.1 dB ekleme yaptığı sonucunu vermiştir. Mikrodalga karakterizasyon adımlarından sonra, önerilen paketleme yöntemi paralel, kapasitif değeçli RF MEMS anahtarlara uygulanmıştır. Uygulanan dayanıklılık analizleri (kırma kuvveti testleri), mekanik analizler (optik profilometre ölçümleri), aktivasyon analizleri (C-V ölçümleri), RF başarım analizleri (S-parametresi ölçümleri), süreksizlik analizleri (anahtarlama zamanı ölçümleri) ve ömür analizleri (ömür sınama ölçümleri) kullanılarak paketlenen anahtarların başarımı değerlendirilmiştir. Uygulanan paketleme yöntemi ile kapakların RF MEMS anahtarlardan ortalama 18.3 MPa yatay kuvvet ile ayrıldıkları gözlemlenmiştir. Kırma testi uygulanan beş anahtardan bir tanesi 26.9 MPa seviyesinde dayanıklılık göstermiştir. Bu değerler benzeri paketleme yöntemlerinin ulaştığı seviyelerin üzerinde sonuçlar vermiştir. Paketleme sürecinden önce ve sonra uygulanan optik profilometre ölçümleri ile MEMS köprü yapısının ortalama 71 nm yukarı yönlü büküldüğü gösterilmiştir. Bu bükülme değerleri, gerçekleştirilen aktivasyon analizleri ile tutarlılık göstermektedir. Dokuz paketli anahtar ile gerçekleştirilen analizlerde, aktivasyon voltajları ortalama 4.2 V artış göstermiştir. S-parametre ölçümleri paket yapısının ihmal edilebilir etkisini ortaya koymuştur. Yukarı durumda 35 GHz çalışma frekansında geri dönüş kayıpları ve araya girme kayıpları sırasıyla 28 dB ve 0.4 dB olarak ölçülmüştür. Buna ek olarak, 35 GHz çalışma frekansında aşağı durum yalıtım seviyeleri birçok paketli anahtar için 35 dB seviyesinde gözlemlenmiştir. Süreksizlik ölçümleri paketli anahtarlar için 10 μs yükselme süresi ve 8.5 μs çökme süresi ortaya koymuştur. Ömür sınama testlerinde bir paketli anahtar RF başarımı bozulmadan 10.2 milyar kere çalışmıştır. Olası proses varyasyonları düşünülerek gerçekleştirilen ve EM benzetim sonuçlarına dayanan hassasiyet analizleri, paketleme yönteminin dayanıklılığını ve proses değişkenlerinden pek etkilenmediğini göstermiştir. Bu tez, paketleme yöntemine ve yapılan başarım analizlerine ek olarak, özgün, parçalı geniş bantlı bir karakterizasyon yöntemini de sunmaktadır. Bu yöntem ile RF MEMS anahtarların üretiminde ve paketlenmesinde kullanılan cam ve yüksek özdirençli silisyum alttaşların dielektrik sabitlerinin frekansa bağlılıkları gösterilmiştir.

Anahtar Kelimeler: RF MEMS, anahtar, paketleme, BCB, EDK, başarım

To milove and to Pera...

ACKNOWLEDGMENTS

Öncelikle doktora çalışmalarım boyunca bana sağladıkları olanaklar için tez danışmanım Prof. Dr. Şimşek Demir ve yardımcı tez danışmanım Prof. Dr. Tayfun Akın'a minnet duygularımı ifade etmek istiyorum.

TİK jürilerimde çalışmalarım ile ilgili beni motive ettikleri ve yol göstererek çalışmalarıma yön verdikleri için Prof. Dr. Seyit Sencer Koç ve Doç. Dr. Mehmet Ünlü'ye çok teşekkür ederim. Doç. Dr. Mehmet Ünlü'ye bütün doktora süreci boyunca bir eğitmen ve arkadaş olduğu için ayrıca teşekkürü bir borç bilirim.

Dr. Kağan Topallı'ya özellikle RF MEMS yapıların paketlenmesi konusunda ön ayak olduğu ve beni bu doğrultuda yönlendirdiği için minnettarım.

Doktora süreci içerisinde aynı ofisi paylaştığım ODTÜ RF MEMS grubu üyeleri Dr. Ömer Bayraktar, Dr. Ebru Sağıroğlu, Dr. Kaan Demirel, Özgehan Kılıç, Dr. Korkut Kağan Tokgöz, Dr. Orçun Kiriş, Savaş Karadağ ve Enis Kobal'a, geçirdiğimiz güzel zamanlar ve çalışmalarım sırasında sağladıkları destekten dolayı teşekkür ederim. ODTÜ RF MEMS grubunun üyesi değerli dostum Dr. Çağrı Çetintepe'ye ayrıca teşekkür etmek isterim. İhtiyaç duyduğunuz her acil durumda desteğini gönül rahatlağıyla isteyebileceğiniz biri olmasının yanında, iyi bir yol arkadaşı olduğu içinde kendisine minnettarım.

Doktora çalışması süresince ODTÜ MEMS Merkezi çalışanlarına teşekkür etmezsem büyük bir haksızlık yapmış olurum. Bu anlamda Orhan Akar, Dr. Ebru Sağıroğlu, Dr. Akın Aydemir'e süreç geliştirme çalışmalarında sağladıkları destekten dolayı teşekkür ederim.

Yalnızca doktora süresi boyunca değil, üniversite yaşamı boyunca ve ömrümün geri kalan süresince de yanımda olduklarını bildiğim ve her daim yanlarında olduğumu bilmelerini istediğim Aşır dostlarıma geçirdiğimiz ve geçireceğimiz güzel günler için teşekkür ederim. Onların olmadığı bir hayat eksik olurdu!

Elbette herkesten çok hep yanımda oldukları, desteklerini esirgemedikleri, koşarak yardımıma yetiştikleri için aileme teşekkür etmek istiyorum. Bir nebze olsun onları gururlandırabildimse, bu beni dünyanın en mutlu insanı yapar.

Sevgili karım, hayat arkadaşım Ferah Ceren Comart'a sabrı için teşekkür ederim. Onunla birlikte geçirmeyi tercih edeceğim zamanları çalışmalarıma ayırdığım ve bana bu konuda destek vermekten bıkmadığı için...

TABLE OF CONTENTS

LIST OF TABLES

TABLES

LIST OF FIGURES

FIGURES

LIST OF ABBREVIATIONS

ABBREVIATIONS	Descriptions
RF MEMS	Radio-Frequency Micro-Electro-Mechanical Systems
RF	Radio-Frequency
Au	Gold
Cr	Chrome
BHF	Buffered Hydrofluoric Acid
PR	Photoresist
Si_xN_y	Silicon Nitride
SiO_2	Silicon Oxide
Si	Silicon
BCB	Benzocyclobutane
TMAH	Tetramethylammonium Hydroxide
SEM	Scanning Electron Microscope
LPCVD	Low-Pressure Chemical Vapor Deposition
PECVD	Plasma Enhanced Chemical Vapor Deposition
DRIE	Deep Reactive Ion Etching
RIE	Reactive Ion Etching
CPW	Coplanar Waveguide
GCPW	Grounded Coplanar Waveguide
EM	Electromagnetic
C-V	Capacitance-Voltage
TEM	Transverse Electromagnetic
TL	Transmission Line

CAD	Computer-Aided Design
SPST	Single-Pole-Single-Throw
SOLT	Short-Open-Load-Thru
VNA	Vector Network Analyzer
ISS	Impedance Standard Substrate
DUT	Device Under Test
BCBt	Benzocyclobutane Thickness
BCBw	Benzocyclobutane Lane Width
SiNt	Silicon Nitride Thickness
cavd	Cavity Depth

CHAPTER 1

INTRODUCTION

Radio-Frequency Micro-Electro-Mechanical Systems (RF MEMS) define the devices, which have functionality in the RF domain due to the movability of their micrometer size mechanical members. The electrical signals may undergo significant changes owing to the mechanical movements of designed parts of the RF MEMS devices. The RF MEMS devices are so sensitive to mechanical movements and require advanced micromachining techniques during their fabrication. These fabrication techniques enabled precise fabrication with very low mechanical tolerances and led to the so-called low-loss and low-cost RF MEMS devices. Having relatively small sizes enables these devices to possess low insertion loss.

Furthermore, the utilization of high conductivity metals (i.e., Au, Cu) and low loss dielectric substrates (i.e., quartz, glass) supports this attribute. The fabrication of a large number of these relatively small size components on a single substrate favors low-cost nature. The definition itself unfolds the passive nature of the RF MEMS devices. Moreover, high linearity is also one of the defining attributes of these devices. The design of these devices is also rather dull compared to their counterparts in terms of performance. Due to their high electrical performance, more straightforward design, and low-cost, RF MEMS devices continue to be a key figure in telecommunications and space applications [1].

RF MEMS switch is the basic building block that enables the reconfigurability of the technology. The basic RF MEMS switch [2–8] has two operational states. In one of them, the switch enables the RF power propagation through itself and prevents it in the other. Although there are various kinds of switches, this dissertation focuses on the electrically actuated capacitive contact RF MEMS switches. Much more complicated devices such as phase shifters [9–13] owe their reconfigurability to the building block.

Despite their reliable attributes, RF MEMS technology has its shortcomings in terms of reliability. These reliability concerns appear due to process conditions and the operating environment of the device. Either process-related residues or environmental conditions might hinder the movability of the mechanical members and the functionality of the RF MEMS components. Especially the wafer residues, generated during the dicing operation at the end of the fabrication, degrades the performance of the RF MEMS components [14, 15]. Moreover, dielectric charging and stiction constitute disadvantageous operational conditions for capacitive RF MEMS switches. Humidity is one of the significant factors that aggravate these mechanisms [16, 17]. "RF MEMS devices thus should be protected against these external factors to maintain their reliable operation over a prescribed lifetime" [18]. A zero-level packaging approach integrates the packaging concept into the RF MEMS fabrication flow and protects the operating devices from external factors starting from the device fabrication processes. Thus, it presents a low-cost approach where commercial first- and second-level packaging concepts might have opted. Zero-level packaging approach offers the best protection possible before the end of the MEMS fabrication process cycle [19].

The zero-level packaging approaches can be categorized into two main groups: thin-film encapsulation and chip-capping. The thin-film encapsulation, as the name suggests, utilizes a thin dielectric [20, 21] or metal shell [22, 23] on top of the device to be packaged. This approach usually needs a second sacrificial layer which complicates the packaging process. Chip-capping, on the other hand, requires a cap to be bonded on top of the devices [24, 25]. Bonding methods may vary depending on the application and the device to be packaged. It is frequently encountered to have a bonding interlayer between the device wafer and the cap. Although there are many applied bonding methods in chip-capping, using polymers as the bonding interlayer is the predominant implementation [7, 18, 26–28]. The thin-film encapsulation and the chip-capping approaches will be discussed in detail in Section 1.1 and Section 1.2, respectively.

1.1 Thin Film Encapsulation

Thin-film encapsulation method employs a thin dielectric [29] or metal shell [23] on top of the device to be bonded instead of using a micromachined cap. Figure 1.1 presents a thin film (dielectric) encapsulated SPST RF MEMS switch. Figure 1.2 presents an SEM photo of the thin metal film package fabricated by XLIM Research Institute.

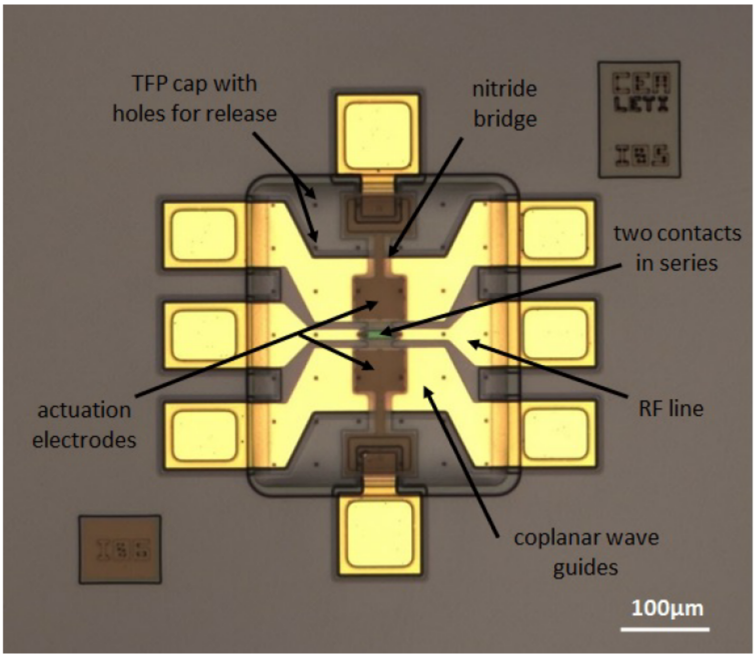

Figure 1.1: An SPST RF MEMS switch encapsulated with the thin film on top [29].

The RF MEMS bridge fabrication usually requires a sacrificial layer where the MEMS bridge is formed on top. Instead of removing this sacrificial layer and thus releasing the MEMS bridge, a second sacrificial layer is coated on top of the MEMS bridge. Then, a thin dielectric layer is deposited by the use of an LPCVD (Low-Pressure Chemical Vapor Deposition) or a PECVD (Plasma Enhanced Chemical Vapor Deposition) equipment on top of the second sacrificial layer. The thin dielectric layer is patterned in a perforated manner. Both sacrificial layers are removed by the use of this perforated structure of the thin shell. The releasing of the MEMS bridge takes place at this step. This perforated thin shell usually is made of Si_xN_y, SiO_2 or some other dielectric layer. As the last step, one more deposition seals the holes on the thin

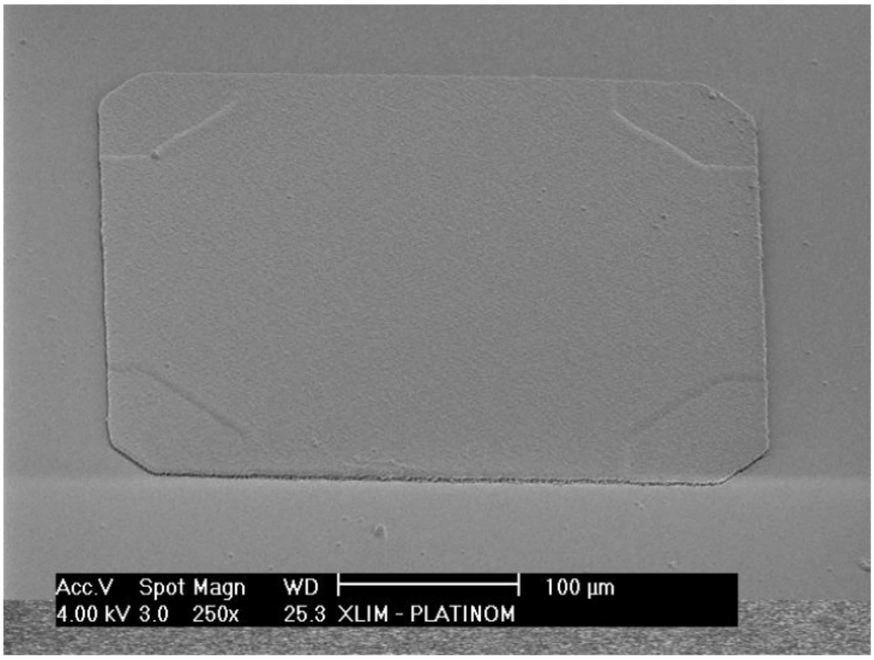

Figure 1.2: An SEM photo of the thin metal film package fabricated by XLIM Research Institute [23].

dielectric shell in a hermetic manner. Being hermetic is one of the most significant attributes of the thin-film encapsulation approach.

Nevertheless, because the dielectric deposition is the final step of the fabrication, the inside of the package, there exist the gases utilized in the deposition process. In other words, it is not possible to fully control the environment within the package and thus, the operational environment. This situation is the most significant drawback of the thin-film encapsulation method.

1.2 Chip Capping

A zero-level package can be realized either on die-level or wafer-level. The die-level approach increases the efficiency (throughput) of the package fabrication considerably by processing every single die separately during packaging. By the use of flip-chip bonders, individual treatment of the caps and RF MEMS devices becomes possible. The most significant drawback of the die-level packaging approach is its time-consuming nature. It takes a considerable amount of time while packaging a large number of components. Wafer-level packaging concept, on the other hand, enables packaging of all the components on a wafer simultaneously. Therefore, this method is much more suitable in term of production speed. "Availability of low-cost commercial packages for zero-level packaged devices also compounds advantages of the latter and makes it more attractive" [30, 31].

1.2.1 Die Bonding

Die bonding necessitates the usage of a die bonder or a flip-chip bonder. In this approach, the caps of the dies to be packaged are singulated before the bonding process [32]. The dies to be packaged can be packaged as a whole wafer, or they may be singulated before the packaging. Since there are individual caps for all of the components, individual packaging takes place. This method benefits from packaging all of the components one by one in terms of throughput. However, packaging individually is a lengthy process and the cost of the packages increase due to this treatment. Figure 1.3 presents a photo of the packaged Radant MEMS switch, where the caps are singulated before the packaging took place.

1.2.2 Wafer Bonding

Instead of treating caps individually, a patterned cap wafer is bonded onto the process wafer by the use of a wafer bonder. Therefore, the dies on a process wafer are packaged simultaneously, which provides a substantial decrease in the packaging time. Although there are various methods of wafer bonding such as anodic bonding, Si-Si eutectic bonding, Au-Au thermocompression bonding, using a bonding interlayer between the process and caps wafers is the most preferred approach. The bonding interlayer is usually chosen as a polymer, since the relatively easy compensation of the parasitic effects. Moreover, having a photo-definable polymer such as BCB or polyimide simplifies the packaging process considerably. Moreover, these interlayers provide a stable RF performance where the electrical permittivities do not alter much with the increasing frequency. The relatively low bonding temperatures (250

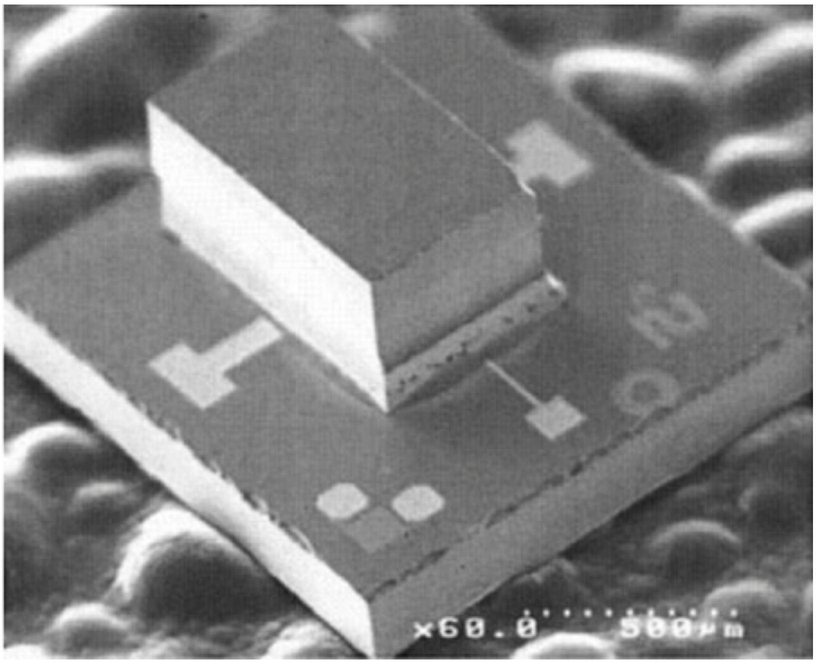

Figure 1.3: An SEM photo of the packaged Radant MEMS switch where the caps are bonded by die bonding [7].

°C) and the low outgassing of BCB also make it a right candidate for RF MEMS applications [15, 32–36].

1.3 Motivation of Dissertation

A zero-level packaging approach is proposed to package 35 GHz shunt, capacitive contact RF MEMS switches. The proposed packaging method utilizes chip-capping of the RF MEMS components by wafer bonding, where a BCB interlayer adheres the high-resistivity silicon cap wafer ($\geq$10 kΩ.cm) to glass device wafer. Planar feedthrough transitions carry the RF ports of the utilized CPW transmission lines, which forms the basis for the RF MEMS components, to outside of the package. The packaging concept and the fabrication of the RF MEMS components evolved together to complement each other. [37] presents an early version of the developed switch fabrication process. One of the most crucial problems is the plastic deformation limit of the MEMS bridges (fixed-fixed beam), which endure the harsh process conditions during the wafer bonding. The peak temperature of the BCB bonding process reaches

(250 °C), and the wafers stay around 1 hour at the peak temperature during the wafer bonding. A novel fabrication scheme is designed in order for the MEMS bridges to overcome the packaging process. Instead of utilizing a metal fixed-fixed beam as the MEMS bridge, the structural Au layer of the MEMS bridge is sandwiched between a top and bottom silicon nitride layer. Therefore, a thermally strong and stable mechanical structure is attained. A more elaborate description of the RF MEMS switch fabrication process, including the packaging steps is included in Chapter 2.

One of the defining features of a package is its ability to protect the RF MEMS components against hindering environmental conditions such as dust, process-related residues, and humidity. Moreover, by providing the required environment within, the package directly influences the operating conditions and lifetime of the components. The BCB provides semi-hermeticity for the package, where humidity is the dominant factor in disturbing the RF, transient, and lifetime performance of the RF MEMS components [38]. The humidity increases the charging induced effects considerably [39, 40]. The step-up coverage of the BCB layer (10 µm thickness) on 1 µm thick gold layer also supports the semi-hermeticity of the package. BCB may be considered hermetic provided that the width of the lanes increase [41, 42]. The trade-off factor in BCB width is the increased insertion loss of the RF MEMS components by the increased planar feedthrough length. The BCB lane width in the proposed packaging method is 200 µm, and this provides the semi-hermeticity of the package. The reliability analysis of the packaged RF MEMS switch based on lifetime measurements demonstrates this behavior of the package.

One of the significant features of the packaging process scheme is the dicing step (die singulation) following the wafer bonding process. The dicing process consists of three steps, where the die singulation takes place at the last one. The unused spaces (Si strips) of the high-resistivity Si cap wafer between adjacent RF MEMS devices are removed in the first dicing step. Therefore, the RF ports of the packaged devices become accessible via RF probes. In other words, the RF measurements of the packaged components can be performed after the first step of the dicing scheme. This approach sets apart the zero level packaging method from similar studies, which utilizes grinding cap singulation process to define the pad window openings [43]. The Si cap wafer is singulated by a dicing step in the orthogonal plane to the one in the first dicing steps. The last step includes the dicing of the glass device wafer, by which the packaged die singulation occurs.

Another significant feature of the developed packaging approach is the mechanical strength of the packages. The endurance of the package is as muscular as its weakest point in terms of shear strength. The adhesion between the BCB layer and the Au layer (CPW metallization layer) lacks the necessary strength. The adhesion of silicon nitride, on the other hand, is better with both BCB and the gold. Therefore, a silicon nitride mid-layer between the BCB and the Au layer strengthens the mechanical endurance of the package. The developed BCB package distinguishes from similar work in term of shear strength [32, 43]. The shear strength of the proposed BCB package proves almost comparable with the results in [44], which complements the BCB bonding approach with silver epoxy bonding. In other words, the utilization of a silicon nitride layer instead of gold for the bonding of the BCB layer increased the shear strength of the BCB bond and the package itself.

Although only CPW transmission lines and RF MEMS switches were packaged, larger modules or subcircuits can also be packaged with the proposed method. The planar feedthrough structure of the package can be applied to any components. There is no limitation to the packaging method in terms of the size of the component to be packaged. On the other hand, having thicker metal layers may disturb the hermeticity of the package. The step-up coverage of the BCB layer might not be sufficient with thicker metallization.

A zero-level package not only supposed to protect the component from being packaged but also have an insignificant effect on the RF performance of the switch. The design of the package, along with the RF MEMS components account for this idea and compensation factors needs to be addressed. The design of the planar feedthrough transitions provides 50 Ω characteristic impedance along the CPW transmission lines and thus slightly disturbs the RF performance of the switch. Before the implementation of the package to RF MEMS switch, CPW transmission lines were packaged to assess the performance analysis of the package. A circuit model is proposed for microwave characterization of the package along with the CPW transmission lines. The microwave characterization of the BCB package is more comprehensive compared with the similar studies [45]. The performance of the package, especially the effects of the planar feedthrough regions, is obtained. The optimized package presented ∼0.05 dB/transition insertion loss. The BCB packaged 35 GHz shunt, and capacitive RF MEMS switch presented ∼0.4 dB insertion loss at the operating frequency. According to the optical profiler measurements of the three MEMS bridges before and after the packaging, the center deflection is only 71 nm in the average. The RF performance of the BCB packaged RF MEMS switch support this measurement results as well. There is an insignificant change in the performance of the RF MEMS switch in the upstate.

The circuit modeling of the BCB packaged 50 Ω CPW transmission lines were conducted for 1-40 GHz band at 35 GHz single frequency. Therefore, the characterization procedure does not take the dispersive effects into account. Both the CPW structure and the materials have dispersive nature [46]. "The knowledge of material properties such as the frequency-dependent permittivity is crucial to allow for a proper design procedure of most electronic applications" [47]. In order to obtain information on the dispersive behavior of the utilized wafers (high-resistive silicon and glass) [48], a piecewise wideband characterization procedure is developed within the context of this dissertation. Various CPW transmission lines were designed on glass and high-resistivity silicon wafers and utilized as test structures. The novel method depends on the measurement results of the CPW transmission lines (test structures). The characterization procedure divides the whole frequency band into 2 GHz windows, and do circuit modeling at center frequencies of each window based on a closed-form transmission line model. Among the transmission line model parameters, the electrical permittivity of the utilized substrates was extracted for each window center frequency from the effective permittivity of the transmission line. Conformal mapping techniques play a crucial role in extracting the electrical permittivity of the substrates from the effective permittivity of the transmission line models [49–52]. The extraction method does not depend on propagation constant by a formulation [53]. Furthermore, the same procedure was applied to EM simulation results where the CPW transmission lines were simulated using ANSYS HFSS EM simulator. The dispersive nature of the glass and high-resistive silicon were demonstrated in comparison with the EM simulation results.

A zero-level package has a crucial role in providing an appropriate operating environment within, for the packaged component. In this regard, the packaging is directly related to the reliability of the RF MEMS components. Performing lifetime tests with the packaged RF MEMS components reveals the ability of the package to some extent since the package provides and preserves the operational environment. The zero-level package is not solely responsible for the lifetime performance of the RF MEMS component. Nevertheless, the crucial role it possesses has an undeniable significance. The 35 GHz BCB packaged shunt, capacitive contact RF MEMS switch reached 10.2 billion cycles during the lifetime tests in hot switching conditions [18]. The lifetime measurements took 472 hours in total, and the packaged switch remained in the downstate for 236 hours during the tests.

A zero-level package needs to be robust and should provide identical performance for packaged components. In order to verify the insensitivity of the BCB package against probable process variations, EM simulations were performed. By perturbing process-related parameters such as BCB thickness, BCB lane width, $\mathrm{Si_xNi_y}$ thickness, cavity depth, and BCB relative permittivity in EM simulations, a sensitivity analysis of the BCB package was obtained. As a result of the investigation, the BCB package and the packaging process proved to be insensitive against process variations.

1.4 Overview of the Thesis

This thesis includes seven separate chapters. This chapter (Chapter 1) presents an overview of RF MEMS technology, RF MEMS zero-level packaging and a wide-band characterization method for investigating the dispersive behavior of the utilized substrates (glass and high-resistivity silicon) for the fabrication and packaging of RF MEMS components. Chapter 2 starts with an overview of the description of the wafer-level BCB packaging methodology for RF MEMS components. Then it elaborates on the fabrication steps of the RF MEMS switch and the BCB package as a complete process cycle. Chapter 3 provides information on the microwave characterization of the BCB package based on the performance of the BCB packaged CPW transmission lines. The proposed circuit models the packaged CPW transmission lines and the planar feedthrough regions within the 1-40 GHz frequency band. Chapter 4 describes the application of the BCB package on a 35 GHz shunt, capacitive contact RF MEMS switch. It then focuses on the performance analysis of the BCB packaged switch in various forms and compares the analysis results of the RF MEMS switch before and after the packaging. Chapter 4 includes the endurance analysis based on shear force tests, mechanical analysis based on optical profiler measurements, actuation analysis based on C-V measurements, RF performance analysis based on S-parameter measurements, transient analysis based on switching-time measurements, and reliability analysis based on lifetime measurements of the BCB packaged RF MEMS switch. Chapter 5 provides a sensitivity analysis of the BCB package depending on the EM simulation results. This chapter gives information on the sensitivity of the BCB packaging process with respect to BCB thickness, BCB lane width, Si_xNi_y thickness, cavity depth, and BCB relative permittivity variations. Chapter 6 presents a wideband characterization method based on CPW transmission line measurements aiming to investigate the dispersive (frequency-dependent) behavior of the electrical permittivity of the utilized substrates. Finally, Chapter 7 presents the conclusions, summarizes the dissertation and expresses the possible future work for this study.

CHAPTER 2

PACKAGING METHODOLOGY AND PROCESS DESCRIPTION

This chapter presents a complete switch fabrication process, which gives zero-level packaged capacitive contact RF MEMS switches as an end product. A schematic of the package structure would prove useful before going into any further detail. Figure 2.1 presents a conceptual drawing of the wafer level packaging approach for RF MEMS devices.

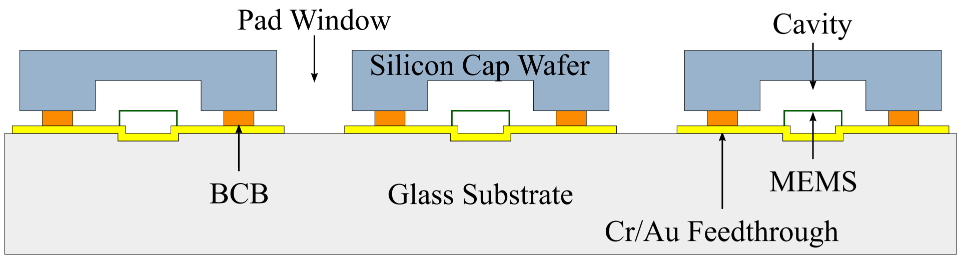

Figure 2.1: The conceptual drawing of a wafer level packaging approach for the RF MEMS devices using BCB bonding.

The packaging approach requires the bonding of a high-resistivity ($\geq$ 10 kΩ.cm) silicon cap wafer to a glass (device) wafer by using BCB as the adhesive interlayer. A complete process cycle, aiming packaged RF MEMS components, was attained by integrating the described BCB packaging approach with a previously developed switch fabrication process cycle. RF MEMS switch is the basic building block for the technology. However, the packaging method is not limited to RF MEMS switches. The packaging of more complex RF MEMS devices is also possible with identical procedures.

The complete fabrication process requires the utilization of seven masks. The BCB packaging process steps and the switch fabrication process steps are compatible with each other. Therefore, the BCB packaging concept is integrated well into the switch fabrication. The chapter provides detailed information on each step of the complete RF MEMS switch fabrication process cycle. Section 2.1 elaborates each process step of the switch fabrication. Section 2.2 then presents the details of the BCB packaging process steps integrated into the RF MEMS switch fabrication.

2.1 RF MEMS Switch Fabrication Process

The RF MEMS switch fabrication is a 4" surface micromachining process, and it requires the separate treatment of a glass wafer and a silicon wafer. The glass wafer process utilizes three of the masks. The Si wafer requires the remaining two.

The switch fabrication process needs no sacrificial layer. This feat is the most significant attribute of the switch fabrication process. Obtaining completely flat MEMS bridges becomes possible by excluding the sacrificial layer process completely. This type of approach provides mechanically more stable MEMS bridges. The suspended MEMS bridges experience high temperatures during the zero-level packaging processes. Therefore, mechanically stable bridges form the basis for the BCB packaging process.

Similar to their processing, separate sections will describe the glass wafer and the silicon wafer fabrication. Section 2.1.1 elaborates the glass wafer process steps. Section 2.1.2 presents the process steps of the silicon wafer. Finally, Section 2.1.3 gives detailed information on the Au-Au thermocompression wafer bonding of the glass wafer and the silicon wafer.

2.1.1 The Fabrication Steps for the Glass Wafer

The glass wafer contains the recess structure on itself, which defines the bridge height of the RF MEMS switch. Furthermore, the glass wafer is responsible for carrying the CPW transmission lines. This CPW transmission lines act as the basis for the RF

MEMS switch. The glass wafer also carries the $\mathrm{Si_xN_y}$ layer. This layer has two distinct duties. Firstly, it operates as the isolation dielectric under the MEMS bridge. Secondly, this layer increases the adhesion of the BCB ring to the Au layers during the wafer bonding.

The fabrication of the glass wafer consists of three main process steps. Figure 2.2 presents a demonstration of the glass wafer after the first process step. A Cr/Au layer is sputtered on the blank glass wafer as the first step of the process. Then, a photoresist layer is spin-coated and patterned by the use of a photolithography step. Afterward, the Cr/Au layer is etched by the use of wet etching process step. A BHF etching process shapes a recess on the glass wafer, whose depth determines the MEMS bridge height. MEMS bridge height is the distance between the bottom surface of the MEMS bridge and the top surface of the isolation dielectric under the bridge. Therefore, the depth of the recess is a critical parameter for the RF MEMS switch performance. The photoresist layer and the Cr/Au layer is stripped at the end of the first process step.

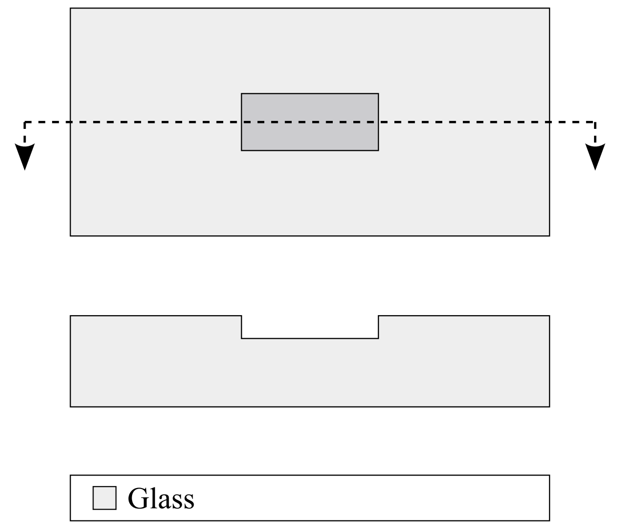

Figure 2.2: The formation of the recess on the glass wafer by BHF etching. Both the top view and the side views are indicated.

The second step requires the sputtering of Cr/Au (25 nm/1.15 µm) layers, on top of the formed recesses. The thin Cr layer under the Au layer improves the adhesion of the Au layer to the glass wafer. The Cr layer has no significant effect on the RF performance of the switches because the CPW trace thicknesses are in the order of two skin depths at the operating frequency. These metal layers form the ground and signal traces of the CPW transmission line, on where the RF MEMS switch constructed. Furthermore, these metal layers have a crucial role in the Au-Au thermocompression bonding step. Figure 2.3 presents the patterned Cr/Au layers on top of the recess, after the completion of the second process step. The Cr layer is not shown in Figure 2.3 since this layer is so thin compared to the Au layer. Furthermore, this layer is sputtered for the adhesion of Au layer to the glas wafer and it is not critical in terms of RF performance.

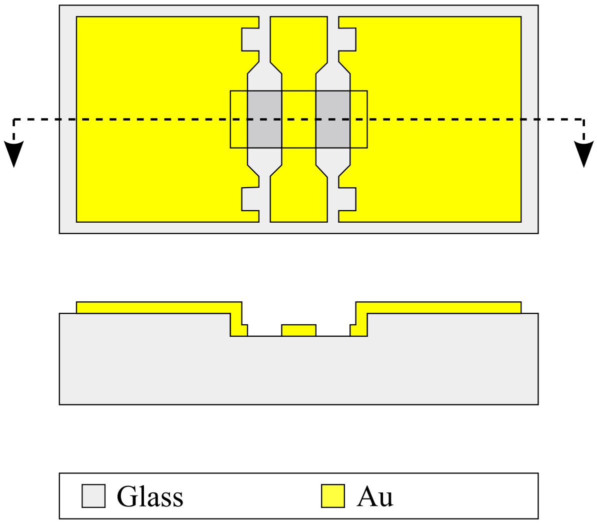

Figure 2.3: The sputtering and patterning of the Cr/Au layers, on which the RF MEMS switch is constructed. Both the top view and the side views are indicated.

As the third and last step with the glass wafer fabrication, a PECVD (Plasma Enhanced Chemical Vapor Deposition) process deposits the Si_xN_y layer. A wet etching process following a photolithography step patterns the Si_xN_y layer. This dielectric layer has two distinct responsibility within the RF MEMS fabrication process. First of all, the Si_xN_y layer acts as the isolation dielectric under the MEMS bridge. The thickness and type (relative electrical permittivity: ϵ_r) of the dielectric directly affect the upstate and downstate capacitances of the RF MEMS switch. Secondly, the same layer improves the adhesion of the BCB layer to the Au layer. Figure 2.4 presents the patterned Si_xN_y layer on the signal trace of the CPW transmission line and also as a

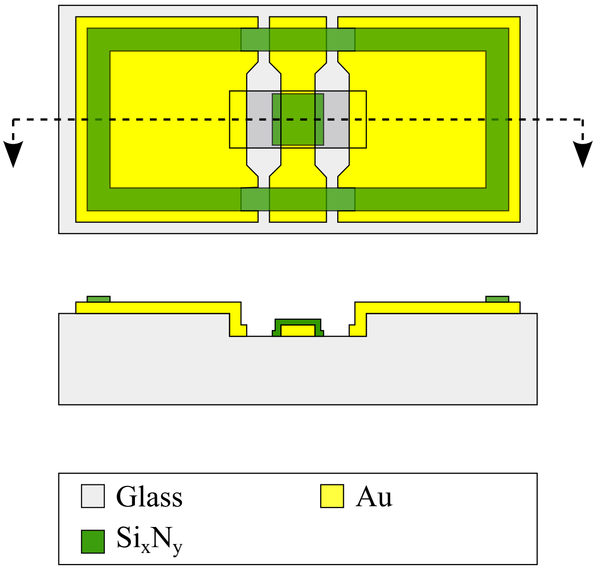

Figure 2.4: The deposition and patterning of the Si_xN_y layer by PECVD and wet etching, respectively. Both the top view and the side views are indicated.

ring around the RF MEMS bridge as a part of the BCB package.

2.1.2 The Fabrication Steps for the Structural Si Wafer

The complete switch fabrication process, including the packaging, requires two different Si wafers. The structural silicon wafer describes the one, which carries the MEMS bridge structures. The cap wafer similarly refers to the high-resistivity silicon wafer carrying the BCB rings. The Au-Au thermocompression bonding of the glass wafer and the silicon wafer forms the RF MEMS switch.

The separate treatment of the silicon wafer starts with the deposition of a Si_xN_y layer by the use of PECVD. Afterward, a sputtering process deposits a Au layer on top of the Si_xN_y layer. The deposition of a second Si_xN_y layer follows the sputtering of the Au layer. Having identical Si_xN_y layers under and on top of the Au layer is crucial. This sandwich structure (Si_xN_y/Au/Si_xN_y) acts as the MEMS bridge of the RF MEMS switch at the end of the fabrication. Thus, being stress-free is a crucial attribute for this sandwich structure. Figure 2.5 presents the first process step for the

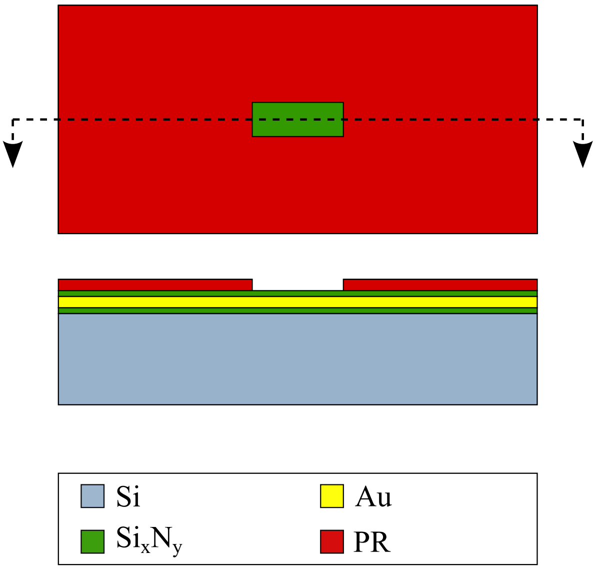

Figure 2.5: A patterned PR layer acts as a mask layer for the patterning of the top Si_xN_y layer. Both the top view and the side views are indicated.

silicon wafer. A photoresist (PR) layer acts as a mask for patterning the top Si_xN_y layer.

Figure 2.6 indicates the finalized MEMS bridge structure. A wet etching step following a photolithography step patterns the Au layer and the bottom Si_xN_y layer. The dumbbell shape and structure of the bridge provide stable mechanical operation.

2.1.3 Wafer Bonding of the Glass Wafer and the Structural Silicon Wafer

Au-Au thermocompression bonding is one of the most critical process steps of the entire switch fabrication. The quality of the bonding directly affects the mechanical behavior of the MEMS bridges. Furthermore, a possible misalignment between the glass wafer and the structural silicon wafer may degrade the RF performance of the switches. The Au-Au thermocompression bonding is performed at 320 °C for 1 hour under 4 kN force. Figure 2.7 presents the situation after the Au-Au bonding.

The structural silicon wafer is flipped during the wafer bonding and therefore, the top and bottom Si_xN_y layer on the MEMS bridge structure changed places as a result of

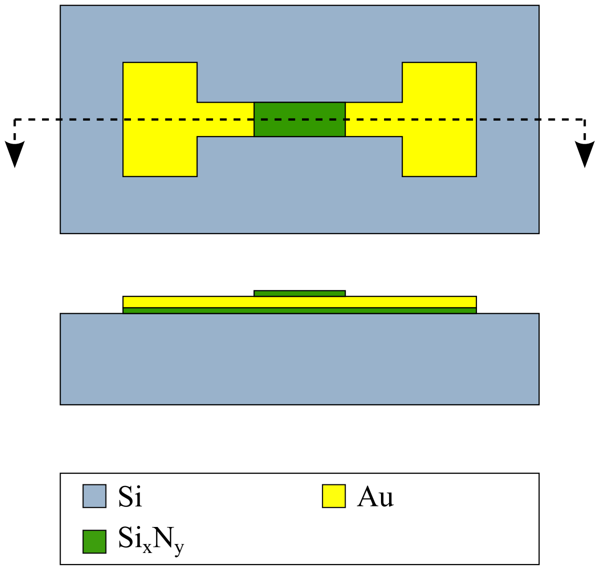

Figure 2.6: MEMS bridge at the end of the second process step for patterning the Au and bottom Si_xN_y layers. Both the top view and the side views are indicated.

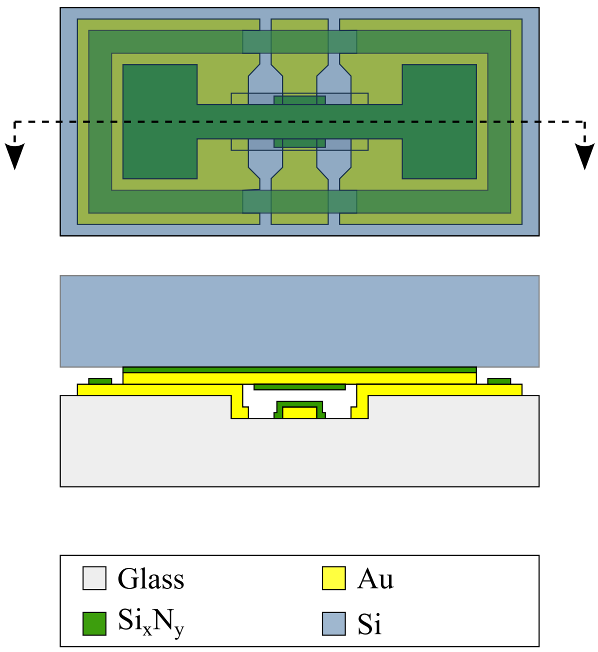

Figure 2.7: The Au-Au thermocompression bonding of the glass and structural silicon wafers. Both the top view and the side views are indicated.

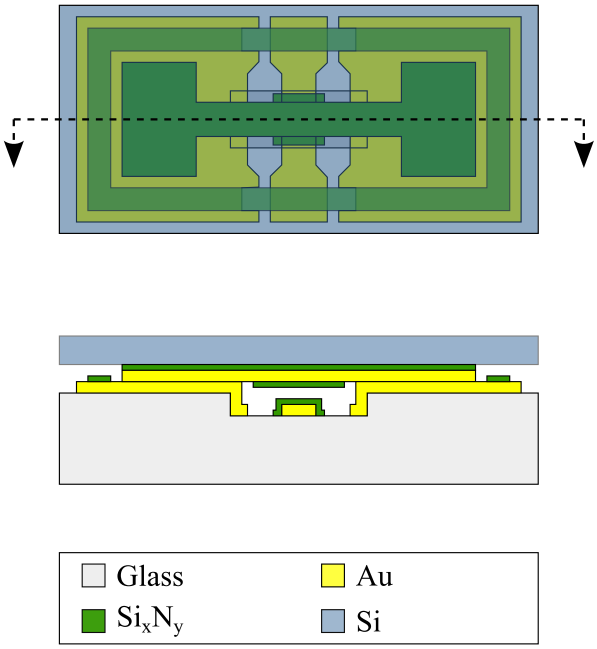

Figure 2.8: A DRIE step thins down the structural silicon wafer. Both the top view and the side views are indicated.

the bonding process. As indicated before, these Si_xN_y layers play a significant role in the mechanical stability of the suspended MEMS bridges.

Structural silicon wafer carries the MEMS structure. However, the silicon wafer itself is not a part of the final RF MEMS switch. Therefore, first of all, a DRIE process thins down the structural silicon wafer. Then secondly, a silicon dissolving process (TMAH) completely removes the structural silicon wafer. Figure 2.8 presents the bonded glass and structural silicon wafers after a DRIE step to decrease the thickness of the silicon wafer.

A TMAH solution dissolves and completely removes the remaining structural silicon wafer from the wafer stack. The suspended MEMS bridges at this step are ready for the optical profiler, C-V, and RF measurements in cleanroom environment. Figure 2.9 presents the suspended RF MEMS switch, after the complete removal of the structural silicon wafer.

This step finalizes the RF MEMS switch fabrication. The zero-level packaging is the

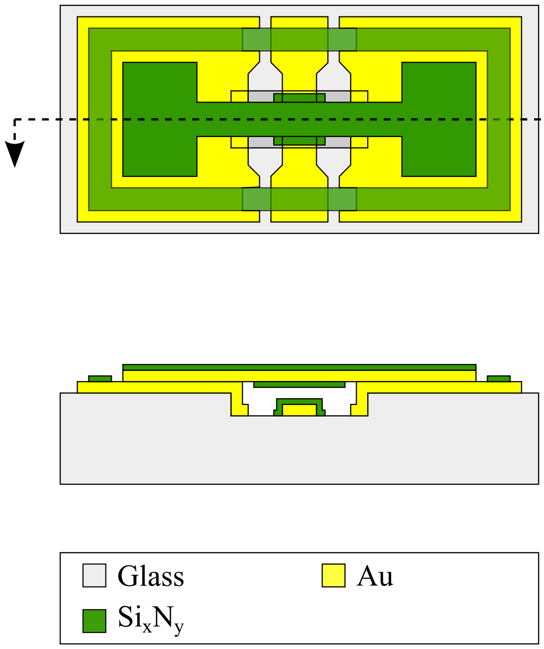

Figure 2.9: A TMAH process completely removes the thinned silicon wafer. Both the top view and the side views are indicated.

next critical step, for having a safe and controlled working environment for the RF MEMS switch.

2.2 BCB Packaging Process

The zero-level package structure depends on wafer bonding of a high-resistivity silicon cap wafer to the fabricated RF MEMS switches by using BCB as the adhesive interlayer. The cap wafer is chosen to be a high-resistivity ($\geq$ 10 kΩ.cm) silicon wafer for utilizing the capability of silicon in process. Moreover, utilizing a high-resistivity silicon improves the insertion loss performance comparably instead of a regular silicon wafer [28]. One of the significant aspects of the high-resistivity silicon and glass wafers are their matching thermal expansion coefficients (CTE). Having a successful wafer bonding with a high CTE mismatch between the wafers is hardly possible. In that regard it is likely that one of the wafers would be cracked at the end of the wafer bonding process.

2.2.1 Fabrication Steps for the High-Resistivity Silicon Cap Wafer

The BCB packaging process consists of two main process steps. First of all, the Cyclotene 4026-46 (photosensitive BCB) resist is spin-coated and patterned by a photolithography step. The coating of BCB is optimized to be the first process step since a polished flat wafer surface is critical in BCB spin-coating. This process step directly affects the quality of the BCB bonding at the end of the packaging process. Figure 2.10 presents the patterned BCB layer (BCB ring around an RF MEMS bridge) on a high-resistivity Si cap wafer.

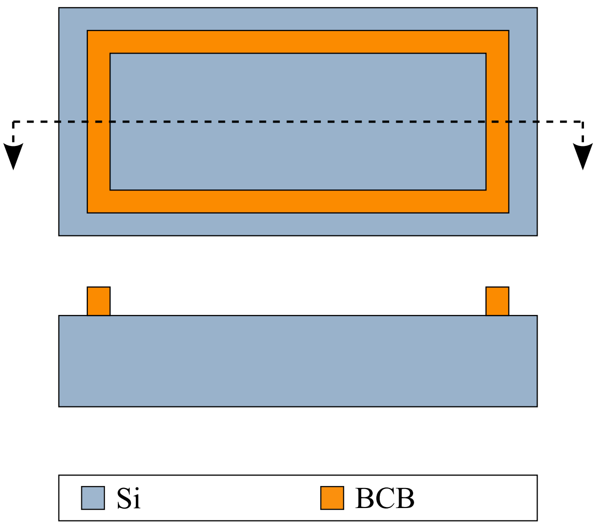

Figure 2.10: A photolithography step patterns the spin-coated BCB layer on top of the high-resistivity silicon cap wafer. Both the top view and the side views are indicated.

The second step in the BCB packaging process is the patterning of the cavities housing the RF MEMS devices and the dicing streets between adjacent RF MEMS devices. The depth of the cavities and the dicing streets is chosen to be 100 µm. The performance of the RF MEMS switches depends on the cavity depth. The impedance loading effect of the silicon cap might increase, provided that the depth of the cavities is low. Furthermore, the depth of the dicing streets is critical, as well. Die singulation step is realized by these dicing streets during the dicing of the BCB packaged RF MEMS switches. In other words, the dicing process at the end of the complete switch fabrication also becomes a part of the BCB packaging process. Figure 2.11 presents the result of the second step of the cap wafer fabrication, where a photolithography process step patterns a PR layer on top of the BCB ring. The PR layer protects the BCB layer during the DRIE process. Figure 2.12 presents the result of the DRIE process for forming the cavities and the dicing streets. The high-resistivity Si cap wafer is ready for BCB bonding, which is the next and final step in the complete RF MEMS switch fabrication process.

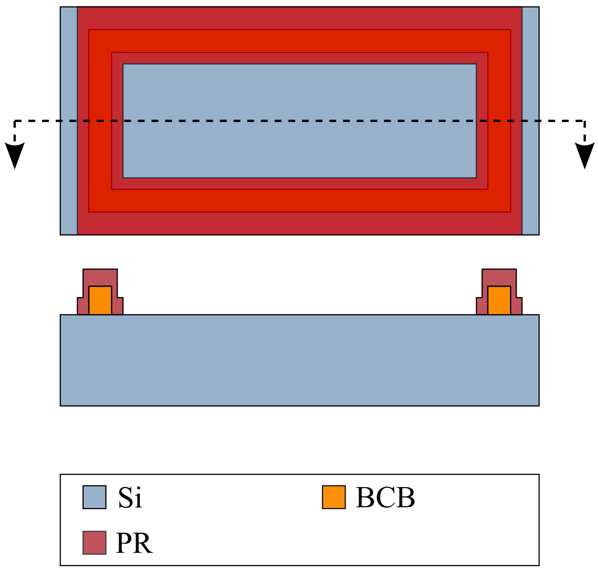

Figure 2.11: The patterning of the spin-coated photoresist layer on top of the BCB ring for protecting the BCB layer during the DRIE process. The top view and the side views are indicated.

2.2.2 BCB Bonding of the High-Resistivity Silicon Cap Wafer onto the Glass Device Wafer

The final step in the complete RF MEMS switch fabrication is the wafer bonding of the high-resistivity silicon cap wafer onto the glass device wafer by using BCB as the adhesive interlayer. Figure 2.13 presents a BCB packaged shunt, capacitive contact RF MEMS switch at the end of a complete fabrication cycle.

One of the crucial aspects of this process step is to obtain a void-free BCB layer during the BCB bonding process. Otherwise, this situation might significantly degrade the

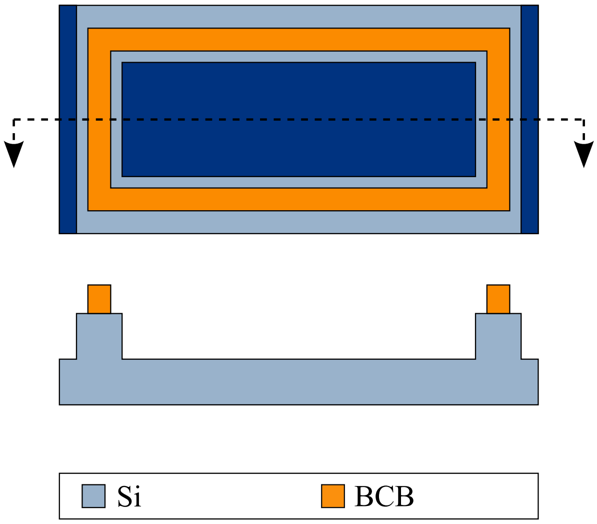

Figure 2.12: The formation of cavities, housing the RF MEMS bridges, and dicing streets after a DRIE process step. The top view and the side views are indicated.

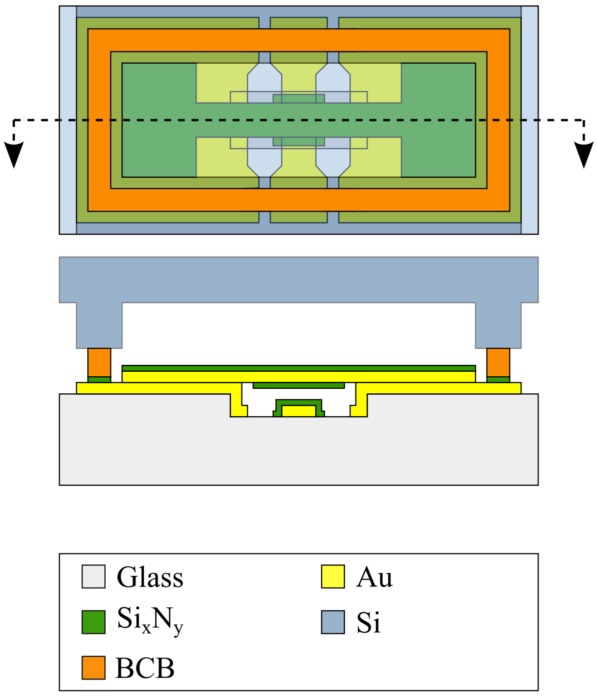

Figure 2.13: Wafer bonding of the high-resistivity Si cap wafer onto the glass wafer using BCB as the adhesive interlayer. The top view and the side views are indicated.

hermeticity level of the BCB (BCB is semi-hermetic). A 15-minute hard bake step at 210 °C solves the void problem in the BCB layer. The hard bake step is applied just before the bonding process.

The BCB bonding process takes place at 250 °C for an hour. The total bonding area on the utilized mask defines the bonding force accordingly. The packaging process takes place while the N_2 gas fills the bonding chamber at 1 atm pressure. This capability is one of the crucial attributes of the wafer bonder equipment.

At the end of the fabrication and packaging of RF MEMS switch, Figure 2.14 presents a photo of the BCB packaged RF MEMS switch on a 2€ coin along with a metric ruler.

Figure 2.14: A photo of the BCB packaged RF MEMS switch on top of a 2€ coin with a metric ruler.

Moreover, the cap of one of the BCB packaged RF MEMS switches is removed and SEM photos of the MEMS bridge is taken. Figure 2.15 and Figure 2.16 present a far-off and a close-up SEM photos of the same RF MEMS switch, respectively.

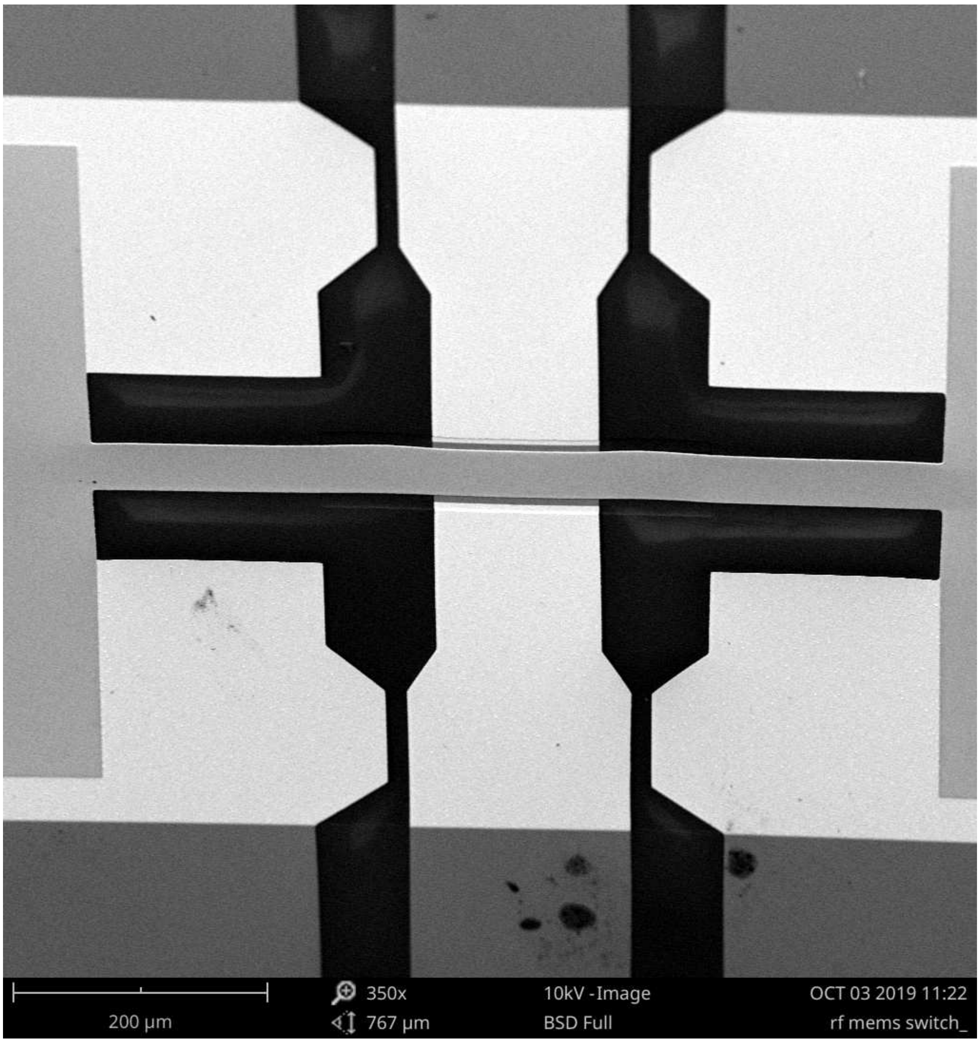

Figure 2.15: SEM image of a BCB packaged RF MEMS switch after the package is removed, where the BCB layer under the package is visible. The MEMS bridge seems to be distorted due to the charging of the glass wafer.

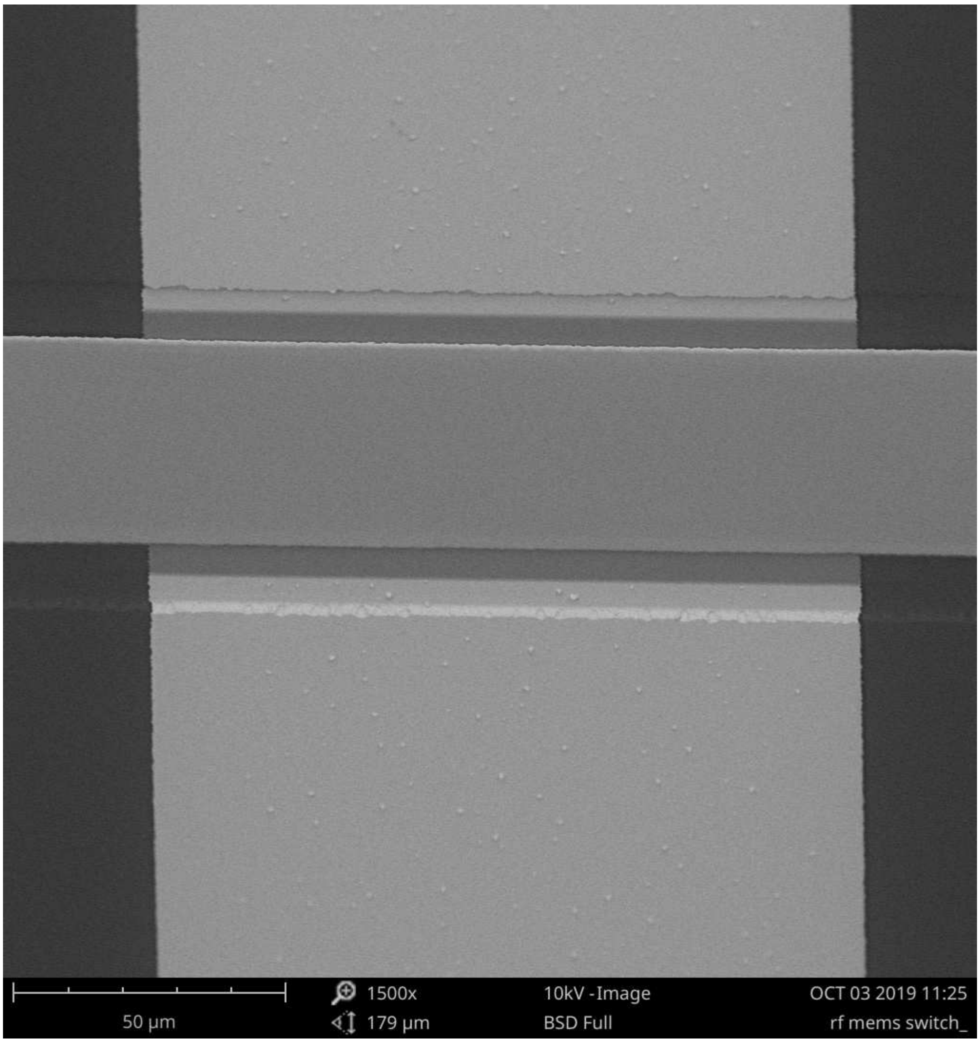

Figure 2.16: A close-up SEM image of a BCB packaged RF MEMS switch in Figure 2.14.

CHAPTER 3

MICROWAVE CHARACTERIZATION AND CIRCUIT MODELING OF THE BCB PACKAGE

In the ideal case, an RF package should not affect the RF performance of the packaged device at all. This aspect is one of the most significant attributes expected from an RF package. This request from an RF package is not fair though. The package absolutely will affect the RF performance of the device. Minimizing the package effects is one of the package designers duties.

This chapter focuses on the microwave characterization of the BCB package. Utilizing a mathematical model is a viable option for analyzing the distinct package effects. One possible way is to use a circuit model for characterizing the package effects. A design procedure is carried out by the use of ANSYS HFSS 3D EM simulator. 50 Ω CPW transmission lines are packaged to perform such a characterization. RF measurements are carried out with these components. Then, a circuit model fitting procedure is applied to these BCB packaged transmission lines for characterizing the RF effects of the package.

This chapter gives elaborated information on the performed characterizations and the results, where Section 3.1 focuses on the characterization procedure and the utilized circuit model, and Section 3.2 presents the characterization results and the circuit model parameters. The characterization results provide fitted circuit model performance along with RF measurement results. The circuit model parameter values will reveal the effect of each circuit segment distinctively.

3.1 Microwave Characterization Procedure

Chapter 2 describes the BCB packaging approach and the sections of the package. The BCB package utilizes the planar feedthrough transitions as the electrical connections between the packaged device and outside world. That is, CPW transmission lines are passing under the BCB package. This transmission line segment (planar feedthrough) is a critical part of the package structure design.

The characterization procedure of the BCB package is carried out by utilizing packaged 50 Ω CPW transmission lines. Figure 3.1 presents a 3D model of the packaged 50 Ω CPW transmission line. The dimensions of the planar transition regions are optimized based on EM simulation results of ANSYS HFSS. Figure 3.2 presents the top view of a planar transition region under the BCB ring, including the critical dimensions.

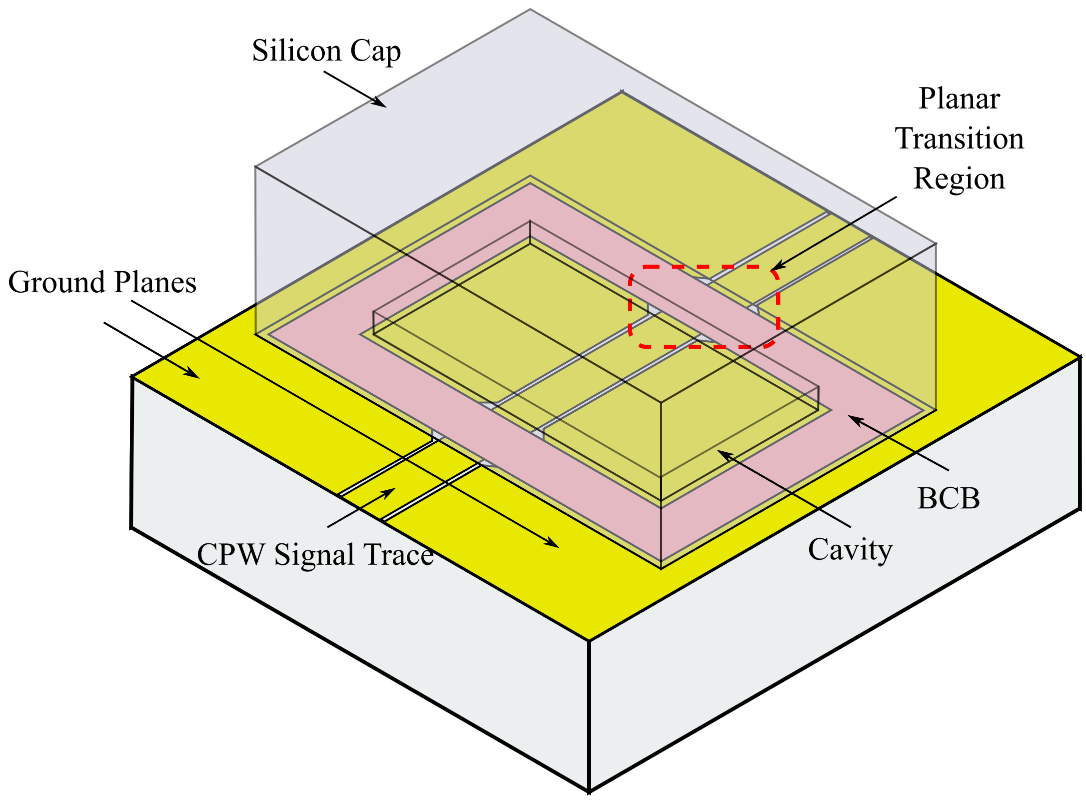

Figure 3.1: A 3D model of a BCB packaged CPW transmission line.

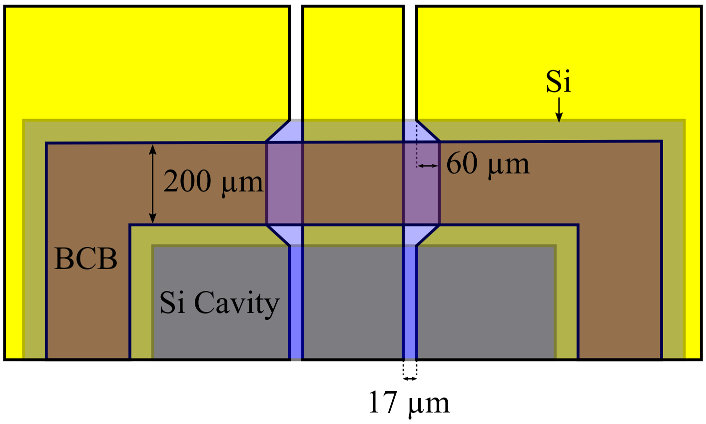

Figure 3.2: A top view of the planar transition regions under the BCB rings.

The BCB packaged 50 Ω CPW transmission line includes different line segments. 3D EM model demonstrates these different segments and RF ports, and they are the building blocks for the utilized circuit model of the system. The circuit model consists of cascaded transmission lines and capacitances between them. Figure 3.3 indicates the employed circuit model to characterize the BCB package.

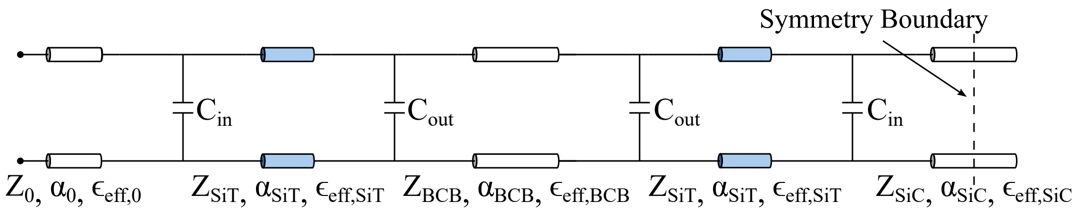

Figure 3.3: The circuit model schematics for the BCB packaged CPW transmission line. Only left half of the symmetric circuit is indicated.

The circuit model and the packaged CPW transmission line are symmetric structures. Therefore, Figure 3.2 presents only left half of the total circuit model. The leftmost transmission line in the circuit model indicates the CPW from RF port to the planar feedthrough. The transmission line parameters of this section are indicated as Z_0, α_0, and $\epsilon_{eff,0}$. The transmission line segment with Z_{SiT}, α_{SiT}, and $\epsilon_{eff,SiT}$ parameters define the entrance and the exit of the planar transition region where only high-resistivity Si substrate hovers over. The parameters of the transmission line section under the BCB ring are abbreviated as Z_{BCB}, α_{BCB}, and $\epsilon_{eff,BCB}$. Finally, Z_{SiC}, α_{SiC}, and $\epsilon_{\mathrm{eff,SiC}}$ defines the CPW transmission line under the package cavity. The $\mathrm{C_{in}}$ and $\mathrm{C_{out}}$ capacitances model the discontinuities on the ground traces of the CPW. These discontinuities violate the quasi-TEM assumption of the CPW transmission line. $\mathrm{C_{in}}$ and $\mathrm{C_{out}}$ model the entrance and the exit of the planar transition regions, respectively.

The characterization procedure includes the curve fitting of the circuit model response with the RF measurement results. The curve fitting is done utilizing the simplex optimization algorithm of the NI AWR Microwave Office. Directly performing optimizations with the circuit model in Figure 3.3 is not appropriate due to the high number of parameters in the circuit model. Thus, test structures such as CPW transmission lines are designed and fabricated to divide the optimizations into smaller parts. The individual circuit model components need independent optimizations to secure a physical model. In other words, the component parameters of a transmission line segment from Figure 3.3, require independent curve fitting to the response of the corresponding test structure. Otherwise, a mathematical model with no physical meaning may mislead the characterization results. Optimizations with different test structures provide the circuit model parameters for each transmission line segment with the applied optimization procedure.

The signal trace width and gap width (between the signal and ground traces) of the CPW at the RF ports are 180 µm and 23 µm, respectively. The leftmost transmission line in Figure 3.3 denotes this CPW. CPW transmission lines with the same dimensions are fabricated to make the circuit model optimization results more physical. Moreover, fabricated CPW transmission lines have three versions with different physical lengths. The lengths of the CPW transmission lines are fixed parameter values. The corresponding circuit models directly utilize these fixed physical lengths. By this way, simultaneous optimizations make the obtained circuit model more reliable. Other than fabricated test structures, applied mathematical boundaries limit the possible parameter values. For instance, a CPW transmission line segment in the planar feedthrough regions must be lossier than the CPW transmission line at the RF ports because the former has BCB and high-resistivity Si layers on top, instead of air. The tangent loss of both BCB and high-resistivity Si are higher than air. Therefore, α_0 defines the lower bound of all α_{SiT}, α_{BCB}, and α_{SiC} values. All these applied methods ensure more physical circuit model parameter values.

3.2 Microwave Characterization Results

Section 3.1 elaborated the applied procedures for increasing the reliability of the circuit model parameters. Utilizing RF measurement results also provides a more physical circuit model instead of EM simulation results. Moreover, employing more than one measurement result may prove useful considering a possible measurement problem. RF performances of five different packaged CPW transmission lines are measured. The curve fitting process utilized these measurement results simultaneously. This situation accounts for possible process variations on the same wafer as well. The placement on the wafer might vary CPW performances. Therefore, the optimizations somehow used an average response of the packaged CPW transmission lines.

A labeling strategy is utilized to label all of the packaged CPW transmission lines on the mask set. The first step requires the numbering of four quadrants of the mask set. Figure 3.4 indicates these quadrants on the utilized mask set.

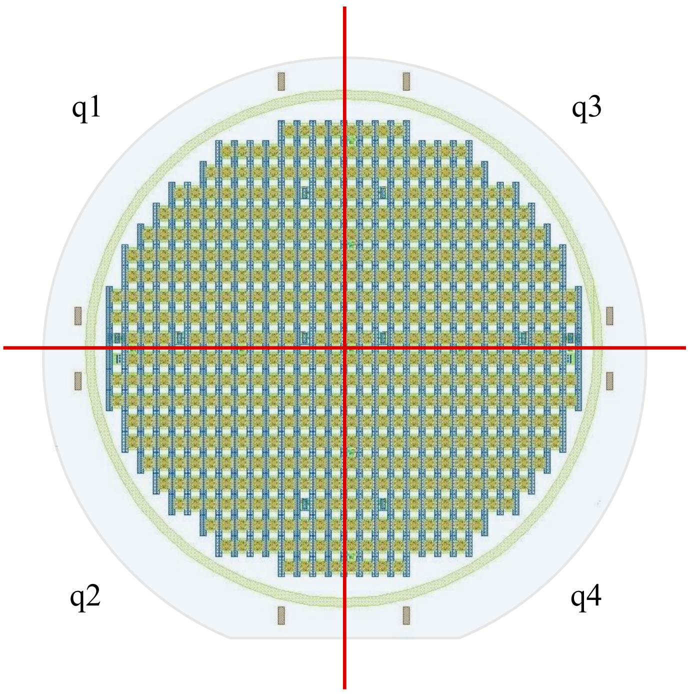

Figure 3.4: The numbers of each four quarters are indicated.

The quadrant number is the first indicator of a corresponding packaged CPW transmission line label. The second and third indicators are column numbers and row numbers. The columns are numbered, starting from 1 from the leftmost columns in all quarters. Likewise, the row numbers are starting from 1 from the uppermost rows in each column of each quarter. The label of a random switch may be q1c13r10, which says that the corresponding switch is in the first quadrant, on the 13$^{\text{th}}$ column and on the 10$^{\text{th}}$ row, which is close to the center in Figure 3.4. The same labeling strategy applies for the BCB packaged RF MEMS switches as well. The performance of these packaged switches will be presented in Chapter 5.

The RF measurements of five different BCB packaged 50 Ω CPW transmission lines (q1c13r9, q2c4r10, q2c7r2, q3c7r9 and q4c1r1) were conducted. The RF measurements were carried out using Agilent E8361A vector network analyzer and Cascade Summit 9000 probe station. The simultaneous curve fitting optimizations determined the parameters of the circuit model in Figure 3.3. Figure 3.5, Figure 3.6, Figure 3.7, and Figure 3.8 present the $|S_{11}|$, $\angle S_{11}$, $|S_{21}|$, and $\angle S_{21}$ of the measurement results of the BCB packaged 50 Ω transmission lines and the fitted circuit model simulation result, respectively.

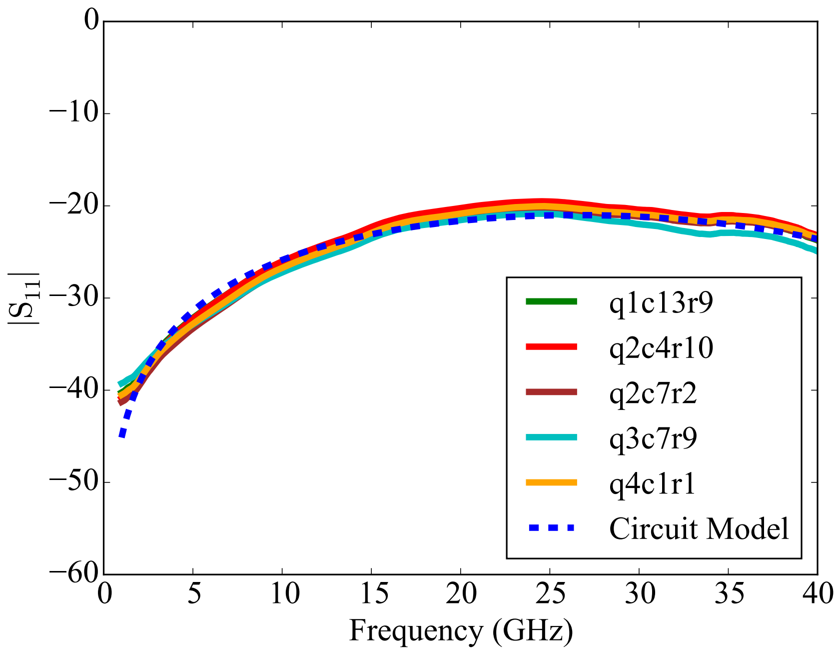

Figure 3.5: Return loss magnitude characteristics of the BCB packaged 50 Ω CPW transmission line measurements and circuit model.

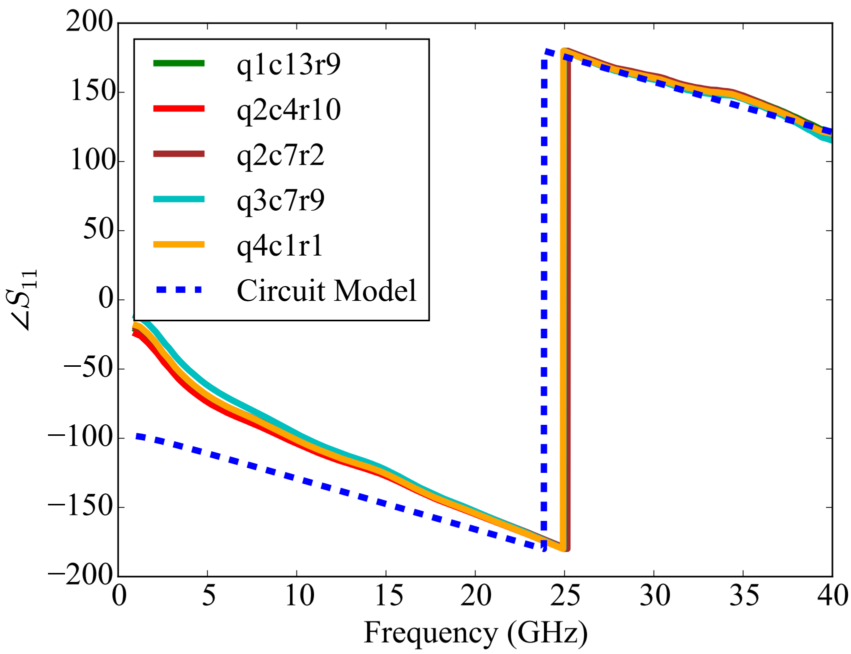

Figure 3.6: Return loss phase characteristics of the BCB packaged 50 Ω CPW transmission line measurements and circuit model.

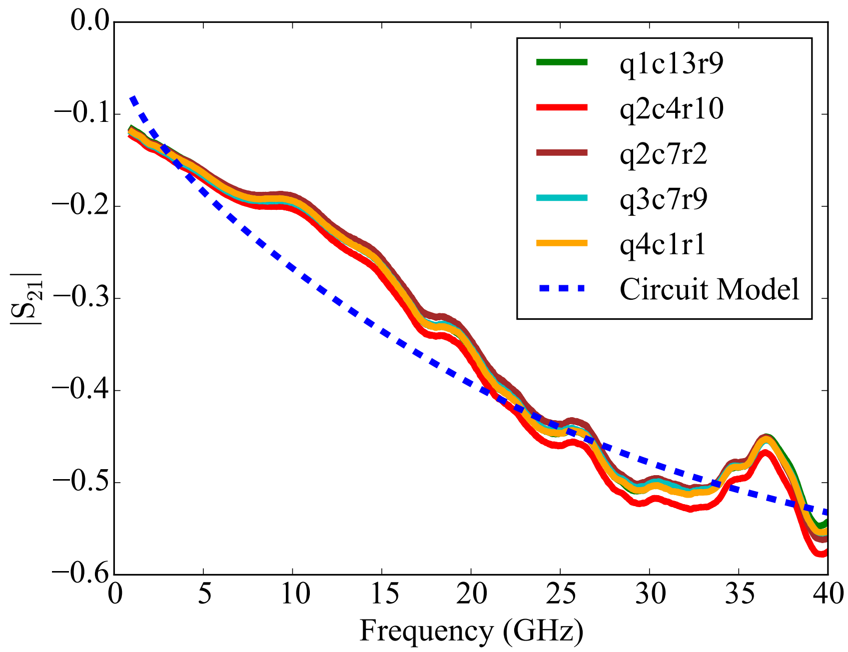

Figure 3.7: Insertion loss magnitude characteristics of the BCB packaged 50 Ω CPW transmission line measurements and circuit model.

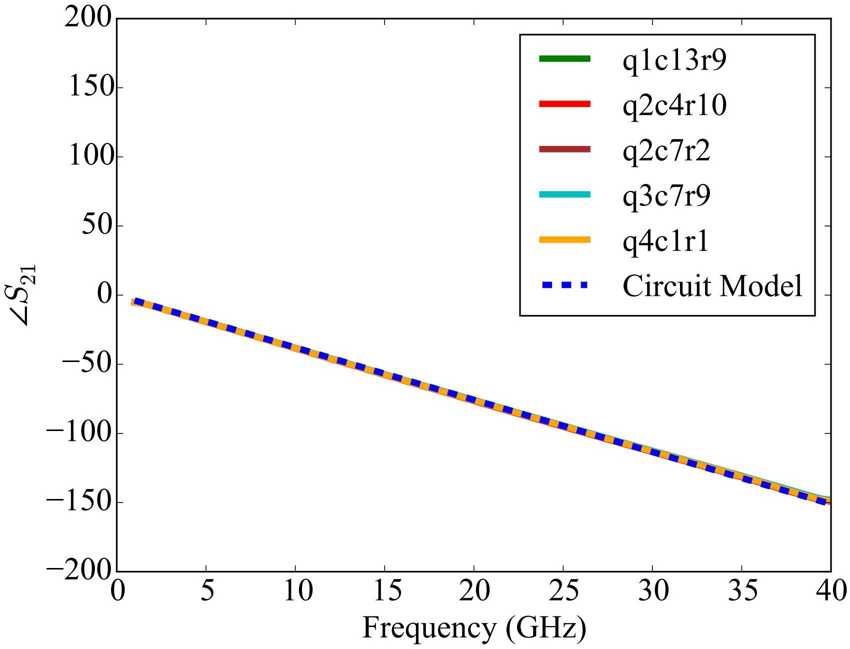

Figure 3.8: Insertion loss phase characteristics of the BCB packaged 50 Ω CPW transmission line measurements and circuit model.

The circuit model demonstrates a good match with the measurement results of packaged 50 Ω CPW transmission lines. The cost function for the curve fitting optimizations of the measurement results (q1c13r9, q2c4r10, q2c7r2, q3c7r9 and q4c1r1) and the circuit model simulations (Figure 3.3) is presented in Equation 3.1.

$$\varepsilon = \sum_{n=1}^{N} \sum_{q=1}^{Q_n} \frac{W_n}{Q_n} \mid G_n(f_q) - M_n(f_q) \mid^{L_n} \tag{3.1}$$

f_q are the analysis frequencies and $\mid G_n - M_n \mid$ is the error parameter. M_n is the magnitude of an S-parameter, W_n is the weight and L_n is the order of the norm. W_n is chosen as 1 and L_n is utilized as 2 in the circuit model optimizations. The error function value at the end of the circuit model parameter optimizations was 2.86×10^{-7}. Circuit model parameter values are determined, as a result of the curve fitting optimizations. Table 3.1 presents the transmission line parameters of the segments for the circuit model in Figure 3.3. Table 3.2 then presents the capacitance values (C_{in} and C_{out}) of the circuit model.

Table 3.1: Optimized transmission line parameter values of the circuit model in 3.3.

	Z_0 (Ω)	length (μm)	ϵ_{eff}	Loss (dB/m)
50 Ω CPW TL	46.5	197.5	2.6	195.0
BCB Transition	47.0	200.0	5.1	300.1
Si Transition	47.1	50.0	5.7	483.8
Si Cavity	44.6	700.0	2.6	207.7

Table 3.2: Optimized capacitance values for the circuit model in Figure 3.3.

	C_{in} (fF)	C_{out} (fF)
BCB Packaged 50 Ω CPW TL	0.1	0.3

The parameters in Table 3.1 summarizes the characteristics of the planar feedthrough transitions. The lengths of the transmission line segments are already fixed numbers based on the packaged 50 Ω CPW transmission lines. One of the most crucial parameters is the loss values for the line segments. By obtaining the losses per unit length for these segments, it becomes possible to predict the total loss effect of a package. Moreover, the per-unit loss of the Si cavity region is only 0.1 dB/m higher than the 50 Ω CPW transmission line. These parameter values indicate the insignificant effect of the Si on top of the Si cavity region.

Furthermore, the Si transition region has a higher per unit length loss value. The Si on top of the transition entrance and exit is responsible for this increase. Finally, the BCB transition region has the highest per unit length loss value. The BCB layer and high-resistivity Si layer on top of the CPW transmission line account for the extra loss. The higher loss tangents of BCB and high-resistivity Si than air demonstrate their effect.

The characteristic impedances of the line segments indicates a good matching performance. The return loss performance of the packaged 50 Ω CPW transmission lines in Figure 3.4 also indicates this situation. The effective permittivity values also demonstrate consistent behavior. Utilizing BCB and high-resistivity Si instead of air on top of transmission line segments increases the effective permittivity of the corresponding line.

CHAPTER 4

SWITCH PACKAGING AND PERFORMANCE ANALYSIS

Chapter 3 presented the performance of an RF package, based on packaged CPW transmission line results. A package must have a minimal effect on the upstate and downstate performance of an RF MEMS switch. The return loss and insertion loss characteristics must be compensated by design variations considering the upstate performance. Furthermore, the operating frequency of the packaged switch might change. Tuning may be required to compensate for the isolation characteristics considering the downstate performance.

One of the most crucial parts of a design procedure is to set design specifications both for upstate and downstate performance of an RF MEMS switch. The compensating design variations for the RF MEMS switch becomes meaningful only by setting the performance goals. Therefore, design specifications should govern the return loss and insertion loss characteristics in the upstate and the isolation characteristics in the downstate. Table 4.1 presents the design specifications, set before the start of the BCB packaged RF MEMS switch design.

Table 4.1: Design specifications for upstate and downstate performances of the BCB packaged RF MEMS devices.

Switch State	**Design Specifications**
upstate	Return Loss $\geq$ 20 dB between 0-40 GHz
	Insertion Loss $\leq$ 0.5 dB @ 35 GHz
downstate	Tuned Isolation @ 35 GHz
	Isolation $\geq$ 20 dB @ 35 GHz

The design procedure for the RF MEMS switch itself is not within the scope of this dissertation. [54] presents an elaborated description of the design procedure and the RF MEMS switch. The operating frequency of the RF MEMS switch is 35 GHz. The design specifications in Table 4.1 reflect the effect of the operating frequency. Better than 20 dB return loss goal for the packaged RF MEMS switch in the upstate indicates the impedance matching. Planar feedthrough transitions directly affect return loss performance. The insertion loss performance goal in the upstate sets a limit to the additional effect of the RF package. The expected isolation performance in the downstate sets a goal not only for the switch itself but also for the RF package. Tuning the isolation performance to 35 GHz may require a design compensation for the RF MEMS switch.

This chapter focuses on the package design for the 35 GHz RF MEMS switch and a discussion on the performance of the end product. Section 4.1 presents the design procedure principles for a packaged RF MEMS switch. Section 4.2 describes the performed design variations for the RF MEMS switch. Section 4.3 then focus on the performance analysis.

4.1 Package Design Procedure for a Capacitive Contact RF MEMS Switch

The packaging concept relies on wafer bonding of a cap wafer onto the device wafer by using BCB as an adhesive interlayer. A systematic design procedure addressing the major decision points is of great importance. One of the major decisions is to choose the adhesive interlayer. The electrical and mechanical properties of the adhesive interlayer directly affect the design phase. For instance, the discontinuity capacitances on the CPW transmission lines strongly depends on the electrical permittivity of the interlayer. First of all, one of the most critical decisions is the thickness of the adhesive interlayer. The thickness of the interlayer directly affects the discontinuity capacitances.

Moreover, step-up coverage tolerance is another factor. The hermeticity of the package depends on the width of the adhesive interlayer. Provided that the BCB ring width increases, the hermeticity level improves. The bonding strength depends on the BCB ring width as well, because the bonding area increases with the BCB ring width. The material choice, which will be in contact with the BCB layer is significant. The bonding quality strongly depends on the BCB layer interactions with other layers. Secondly, planar feedthrough design is another essential concept. The return loss performance (impedance matching) directly depends on this choice. Finally, the downstate performance of the packaged switch strongly depends on inductive tuning. Inductive tuning serves as a compensation mechanism for the RF MEMS switches without affecting the upstate performance. This mechanism tunes the isolation performance according to the desired operating frequency. Therefore, this mechanism compensates the unwanted effects of the RF package. These decisions define the design procedure for the zero-level RF MEMS switch packaging.

The itemized systematic design procedure for a packaged RF MEMS switch is as follows:

1. Choice of adhesive interlayer properties,
   - The thickness of the interlayer considering,
     - Discontinuity capacitances,
     - Step-up coverage,
   - The width of the interlayer considering,
     - Hermeticity,
     - Bonding strength,
   - Material choice for bonding area other than the adhesive interlayer,
     - Bonding strength,
2. Planar feedthrough design,
   - Impedance matching (transition design) for the CPW transmission line under the cap and the interlayer,
3. Inductive tuning,
   - Compensating package effects at downstate.

4.2 Package Design for 35 GHz RF MEMS Switch

This section will elaborate on the design steps of the package structure for 35 GHz capacitive RF MEMS switch. The design phase relies on the acquired data from the microwave characterization of the package. For instance, the planar feedthrough transitions are identical to the packaged 50 Ω CPW transmission line case. Not only the planar feedthroughs but also both package structures are almost identical. There is only a small difference between the width of the packages. However, this change does not affect electrical performance. 3D EM simulations of the unpackaged and packaged RF MEMS switches are performed in ANSYS HFSS. Before going into details about the package design, demonstrating the EM simulation results of the unpackaged RF MEMS switch is useful. Figure 4.1 presents the 3D EM model of the unpackaged 35 GHz capacitive RF MEMS switch. The model employs radiation boundary conditions and lumped ports for excitation. The EM model does not indicate airboxes.

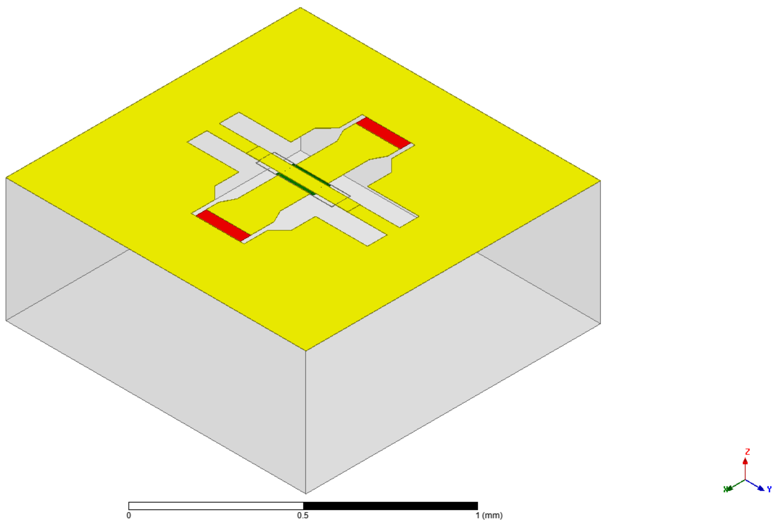

Figure 4.1: 3D EM model of the unpackaged 35 GHz capacitive RF MEMS switch.

Unpackaged switch performance is critical because it provides a reference for the packaged one. The additive RF effects of the package structure reveal themselves in a comparison between the unpackaged and packaged switch performances. Figure 4.2 and Figure 4.3 present the return loss and insertion loss characteristics of the unpackaged RF MEMS switch in the upstate, respectively.

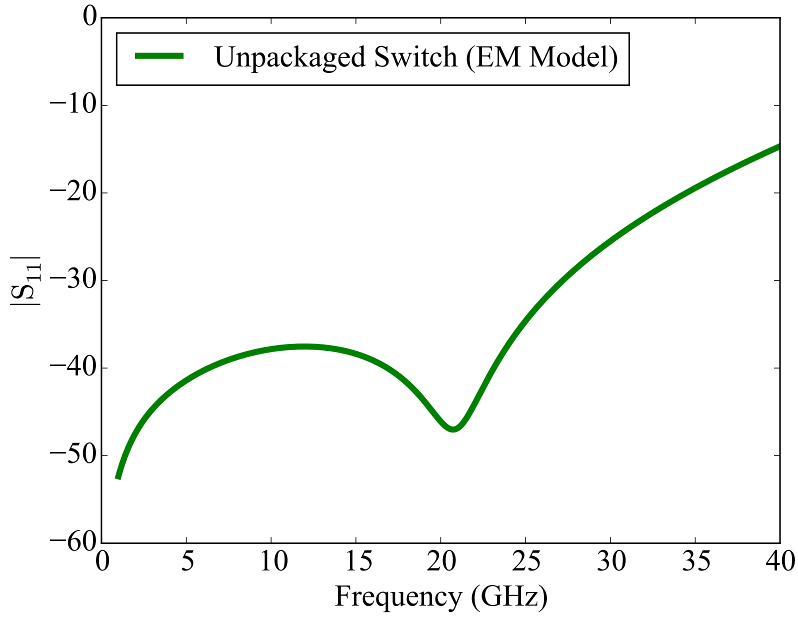

Figure 4.2: Return loss performance of the unpackaged 35 GHz RF MEMS switch in the upstate.

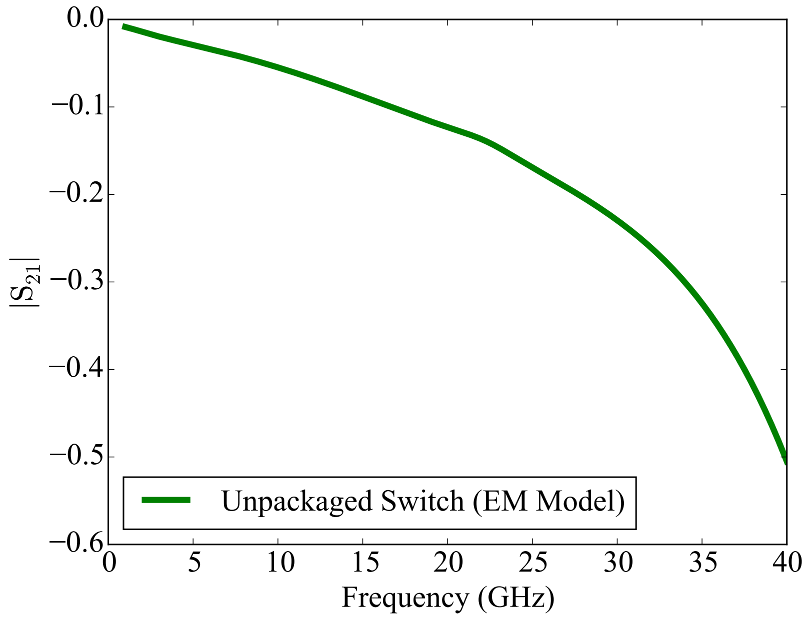

Figure 4.3: Insertion loss performance of the unpackaged 35 GHz RF MEMS switch in the upstate.

The return loss performance of the unpackaged switch indicates a good impedance match within the entire frequency band. Return loss becomes worse as the frequency approaches 40 GHz. This type of return loss performance is opted, instead of having an excellent return loss performance in a narrow band around 35 GHz. The insertion loss at 35 GHz is around 0.3 dB. The 0.5 dB insertion loss goal seems possible for the packaged switch performance. Figure 4.4 then presents the isolation characteristics of the unpackaged RF MEMS switch in the downstate.

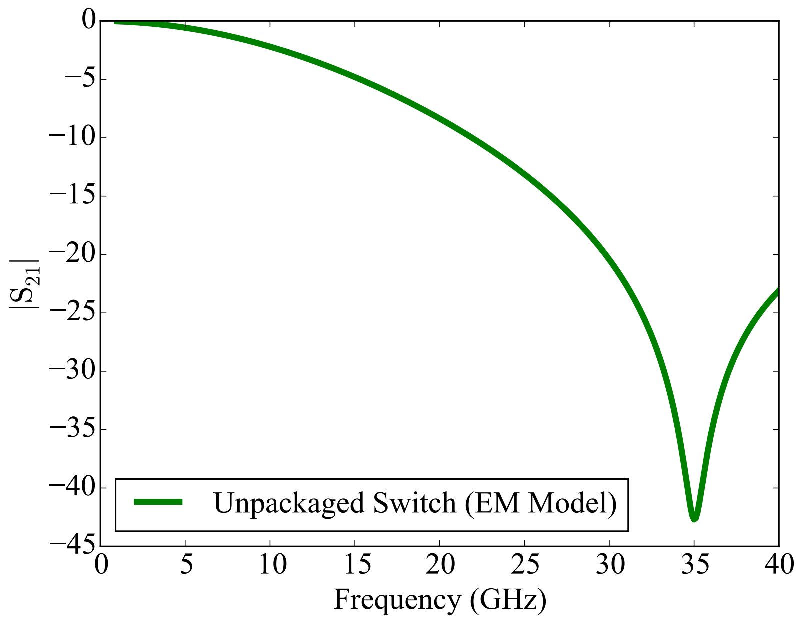

Figure 4.4: Isolation performance of the unpackaged 35 GHz RF MEMS switch in the downstate.

The isolation performance of the unpackaged switch is tuned to 35 GHz as expected. Furthermore, the isolation seems to be better than 40 dB at 35 GHz.

Section 3.1 presented the dimensions of the optimized package structure for the 50 Ω CPW transmission lines. Almost an identical package structure houses the RF MEMS switch, where the small differences do not affect the package performance. Figure 4.5 presents the 3D EM model of the packaged 35 GHz capacitive RF MEMS switch. The model employs radiation boundary conditions and lumped ports for excitation. The EM model does not indicate airboxes.

The EM model in Figure 4.5 is simulated utilizing ANSYS HFSS. The EM simula-

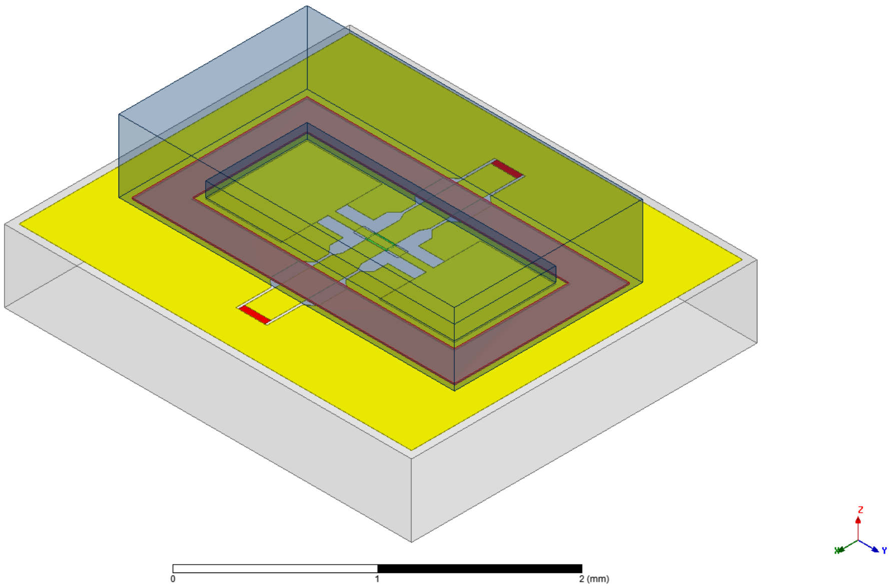

Figure 4.5: 3D EM model of the packaged 35 GHz capacitive RF MEMS switch.

tions provided the upstate and downstate performances of the packaged RF MEMS switch. Figure 4.6 and Figure 4.7 indicate the return loss and insertion loss of both the unpackaged and packaged RF MEMS switches, respectively.

Figure 4.6 indicates an improvement in the return loss performance after the packaging nearing 40 GHz. On the other hand, the return loss worsens in the 0-27 GHz frequency band. As a result, the return loss is better than 20 dB on the entire frequency band. The return loss goal in Table4.1 seems to be verified according to EM simulation results. Figure 4.7 demonstrates an increase in the insertion loss. This situation arises due to the additional loss provided by the package structure. First of all, the planar transition regions add some extra insertion loss since these areas are lossier than 50 Ω CPW transmission lines. Table 3.1 presented the loss per unit length values for planar feedthrough regions and 50 Ω CPW transmission lines. Secondly, the physical length of the RF MEMS switch increased from 600 µm to 1695 µm. Not only the planar feedthroughs increased the length, but also the existence of the package required an increase in the RF port lengths. Otherwise, it would be not possible to do measurements by utilizing RF probes. Nevertheless, the insertion loss of the packaged RF MEMS switch seems to be around 0.5 dB at 35 GHz.

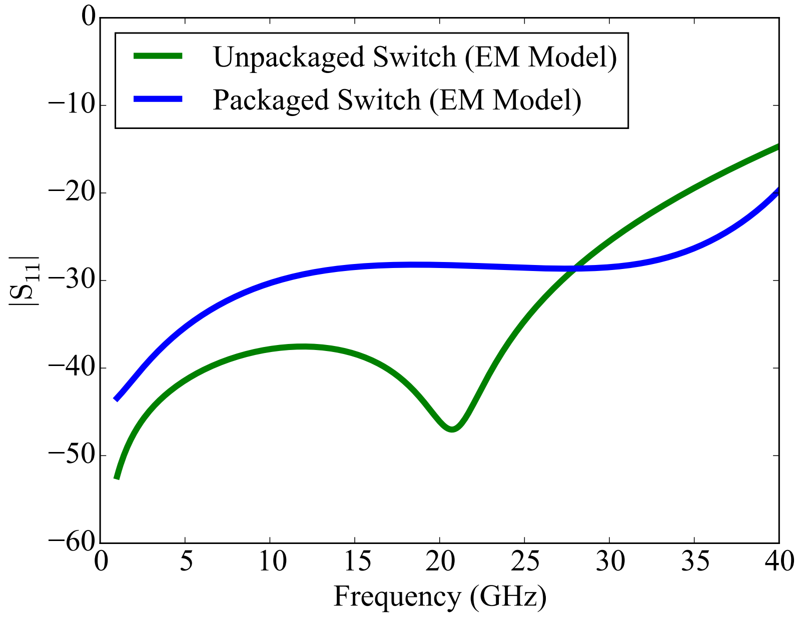

Figure 4.6: Return loss performance of the unpackaged and packaged 35 GHz RF MEMS switch in the upstate according to EM simulations.

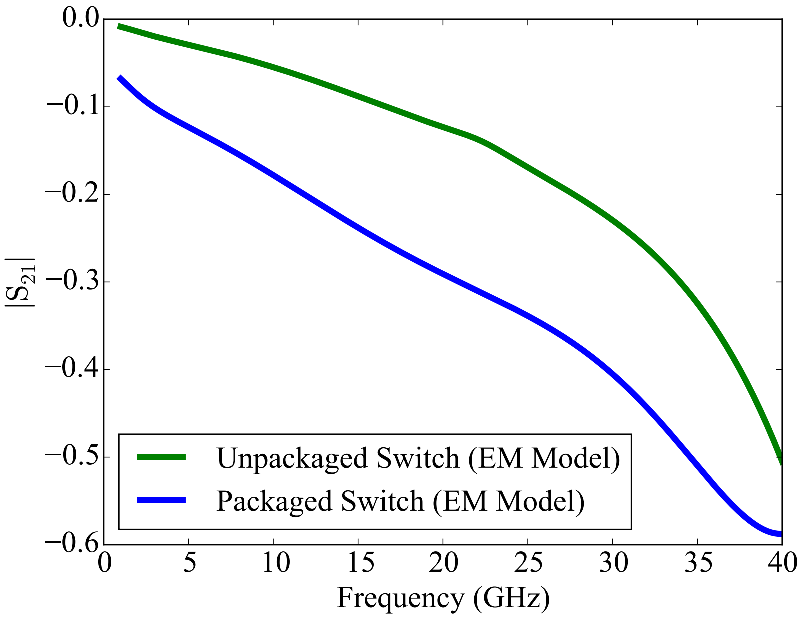

Figure 4.7: Insertion loss performance of the unpackaged 35 GHz RF MEMS switch in the upstate according to EM simulations.

A high-resistivity Si package housing the MEMS bridge alters the isolation performance of the switch. Although the package structure is identical to the 50 Ω CPW transmission line case, the isolation performance needs tuning in the downstate. Therefore, the inductive tuning recesses in Figure 4.1 are altered. The depth of the inductive tuning recesses (the distance into the ground planes of the CPW) is increased from 163 µm to 185 µm. Figure 4.8 presents the isolation performances of the unpackaged and packaged RF MEMS switches in the downstate.

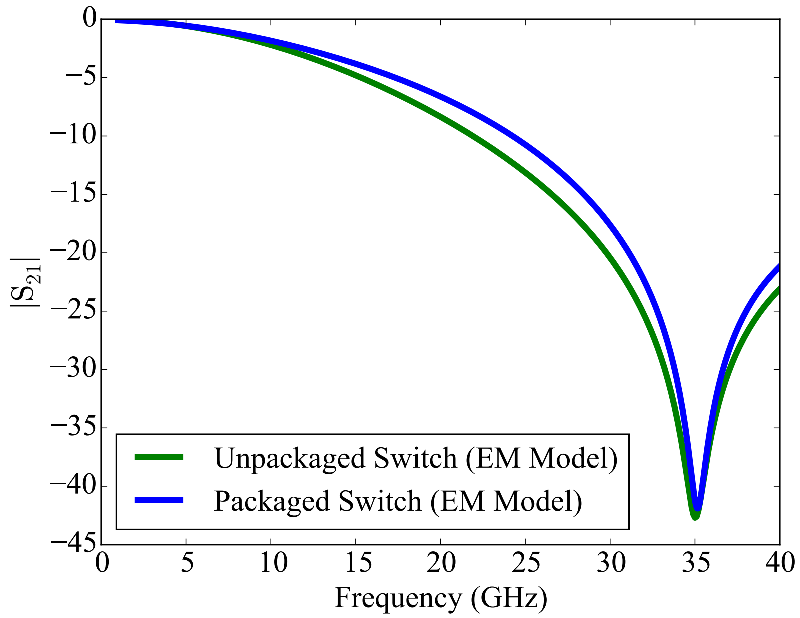

Figure 4.8: Isolation performance of the unpackaged 35 GHz RF MEMS switch in the downstate according to EM simulations.

Figure 4.8 presents tuned performances at 35 GHz both for the unpackaged and packaged RF MEMS switches. Increasing the inductive tuning recess depths narrowed the isolation window slightly. However, the -25 dB isolation window is still accurate in 33-38 GHz frequency band. The effect does not disturb the performance goals at all, and the result is tolerable. The isolation still seems to be better than 40 dB at 35 GHz even after the packaging. According to EM simulation results, the designed package verifies the preset goals in Table 4.1.

Following the completion of the design procedure, the RF MEMS switches were fabricated and packaged. Various measurements and analysis will indicate the overall performance of the packaged switches.

4.3 Performance Analysis for BCB Packaged 35 GHz RF MEMS Switch

This section will elaborate on the performance analysis of the packaged RF MEMS switch. Section 4.3 then focus on the performance analysis. Section 4.3.1 presents the shear force measurements and the durability analysis results. Section 4.3.2 presents the optical profiler measurements and the mechanical analysis results. Section 4.3.3 then presents the C-V measurements and the actuation analysis results. Section 4.3.4 focuses on the S-parameter measurements and the RF performance analysis results. Section 4.3.5 describes the switching-time measurements and the transient analysis results. Finally, Section 4.3.6 presents the lifetime measurements and the reliability analysis results.

4.3.1 Shear Force Tests and Endurance Analysis

The developed packaging approach relies on BCB as the bonding interlayer. However, the adhesion between a Au layer and BCB layer is not particularly strong. A Si_xN_y layer between these Au and BCB layers may prove useful since the adhesion of Si_xN_y to the other layers is stronger. Moreover, a Si_xN_y layer already exists within the RF MEMS switch fabrication process. Utilizing a Si_xN_y layer between the Au and BCB layers may increase the endurance of the packaging approach without adding a mask to the fabrication process. This method and reasoning provided the solution for a stronger package structure.

The shear force method is a way of measuring the durability and strength of a package. Figure 4.9 presents the schematic of a shear force measurement system.

The bottom glass substrate needs fixing against a horizontal movement. Then the cartridge applies a controlled horizontal force from a side of the Si cap wafer. The system increases the horizontal force until the cap wafer detaches from the fixed bottom substrate. The detachment force gives a measure of the adhesion strength of the package.

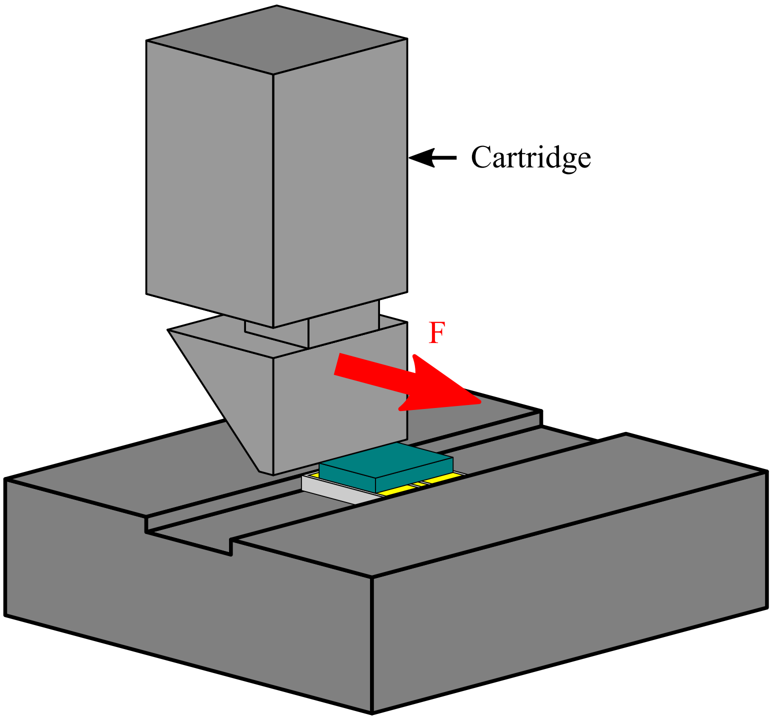

Figure 4.9: Shear force measurement scheme for packaged RF MEMS switches.

DAGE 4000 Bondtester system is utilized to measure five packaged RF MEMS switches (q4c5r4, q2c10r5, q4c8r7, q4c7r4, and q1c9r7). Table 4.2 presents the shear force measurement results of the tested packaged switches.

Table 4.2: Shear force test results for five packaged RF MEMS switches.

Switch ID	**Break Force (N)**	**Break Pressure (MPa)**
q4c5r4	30.7	26.9
q2c10r5	17.3	15.2
q4c8r7	16.7	14.6
q4c7r4	19.3	16.8
q1c9r7	20.8	18.2
Average	$\sim$ 21.0	$\sim$ 18.3

The packaged switches require 21 N average force for the detachment of the caps. Dividing the exerted force with the BCB area gives the detaching pressure. Therefore, the packaged switches demonstrate 18.3 MPa average pressure to detach the caps. The detaching pressure for one of the packaged switches (q4c5r4) reached 26.9 MPa. This value is a record among similar packaging approaches in the literature. Only one study [44] that uses BCB in the packaging scheme can provide 25-30 MPa detaching pressure: however, the BCB bonding is supported by silver epoxy bonding in this case. Table 4.3 presents the detaching pressures of the packaging studies that employs BCB as the bonding interlayer.

Table 4.3: Comparison list of BCB packaging methods in terms of shear strength.

Reference	**Break Pressure (MPa)**
[14]	$\sim$10.0
[33]	$\sim$4.0
[44]	25-30
[15]	20 (max)
[18]	26.9 (max)

4.3.2 Optical Profiler Measurements and Mechanical Analysis

The packaged capacitive contact RF MEMS switches involve a fixed-fixed beam as the MEMS bridge. One of the main problems which can occur during the zero-level packaging process is the buckling of these fixed-fixed beam MEMS bridges. This phenomenon occurs due to the high temperatures during the packaging processes. Although BCB has a relatively low bonding temperature (250 °C), this may still have irreversible effects. The buckling may reach the plastic deformation limit of the MEMS bridge structure. Thereby an irreversible mechanical deflection may occur.

The mechanical design plays a crucial role to minimize the effects of the packaging process. Section 2.1.2 gave details of the MEMS bridge fabrication. The sandwich structure (Si_xN_y-Au-Si_xN_y) forms the basis for the RF MEMS switch fabrication and the zero-level packaging. This mechanical design is symmetric in Z-axis since the deposition conditions of the Si_xN_y layers are identical. Therefore, the MEMS bridge becomes more stable against mechanical changes. In other words, it becomes less prone to possible deflections due to temperature changes.

A differential observation of the MEMS bridge deflection before and after the zero-level packaging process can reveal the mechanical effects of the packaging. Measuring the mechanical state of the MEMS bridges during the fabrication just before the BCB packaging process, forms a reference point. Afterward, measuring the mechanical state of the same switches after the BCB packaging process gives us the required data. Optical profilometer measurements play a crucial role in determining the deflection of the MEMS bridges. The optical profiler measurements require the removal of the caps on the RF MEMS switches.

Optical profiler measurements of three switches (q1c9r1, q3c1r8, and q1c9r5) were performed utilizing Veeco Wyko NT1100 system. The procedure included measuring the deflections before and after the packaging. The optical profiler measurements required the removal of their caps after the packaging. Then, the difference between the mechanical states before and after the packaging gives the buckling amount of the MEMS bridges. The difference between the measurements indicated 71 nm average buckling at the center of the MEMS bridges as a result of the BCB packaging process. Figure 4.10 and Figure 4.11 present the optical profiler measurement results of one of the switches (q1c9r5) before and after the BCB packaging process. The buckling amount at the center of the MEMS bridge is 70 nm for this switch (q1c9r5). Optical profiler measurements form the basis of the mechanical analysis. Even so, an actuation analysis supporting the optical profiler measurements is essential.

4.3.3 C-V Measurements and Actuation Analysis

C-V measurements form the basis for analyzing the actuation voltages of RF MEMS switches. Although the RF-measurement results can provide the actuation voltages as well, the C-V analysis gives additional information on the upstate and downstate capacitances. The actuation analysis utilized C-V measurements only before the packaging in this study. Nevertheless, RF-measurements provided the actuation analysis after the packaging. As the name implies, a setup monitors the capacitance while the potential difference changes. The upstate and downstate capacitances can give valuable information about the mechanical state of the MEMS bridges as well.

Just like the mechanical analysis, the actuation analysis requires measurement results

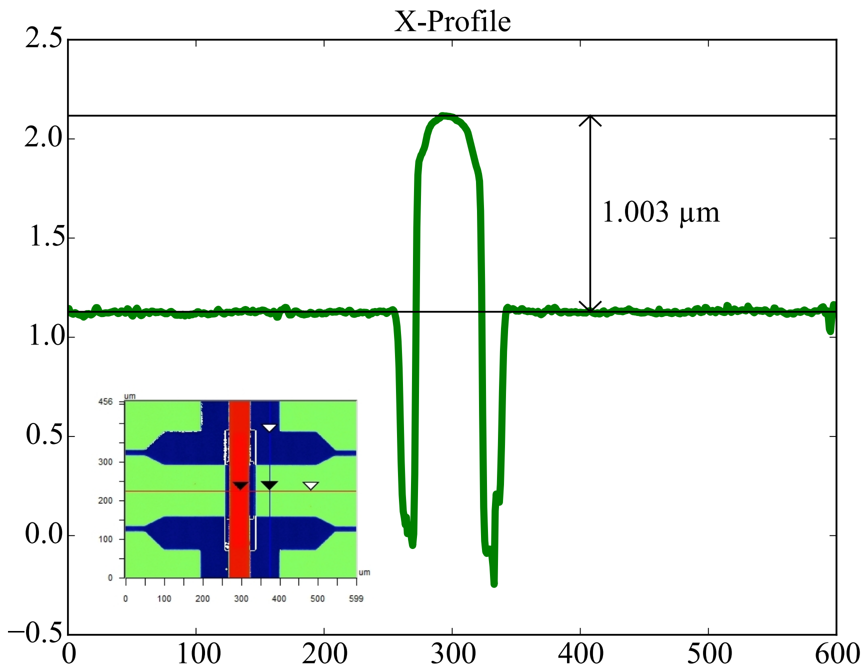

Figure 4.10: Optical profiler measurement result for an RF MEMS switch (q1c9r5) before packaging. The inlet shows the measured RF MEMS switch before the packaging process where the colors indicate thicknesses.

of the RF MEMS switches before and after the packaging. The C-V measurements of 9 switches were performed utilizing Agilent 4294A PIA (Precision Impedance Analyzer) and a DC probe station. The impedance analyzer swept the potential difference between -40 V and 40 V continuously. Since the expected actuation voltages reside in this range, the RF MEMS bridges pulled down in every cycle. Therefore, the setup provided both the upstate and downstate capacitances of the RF MEMS switches.

Table 4.4 presents the actuation voltages of the measured RF MEMS switches before and after the packaging. The C-V measurement results provided the actuation voltages of the switches before the packaging, whereas the RF measurements provided the actuation voltages of the switches after the packaging.

The average actuation voltage of the RF MEMS switches before and after the BCB

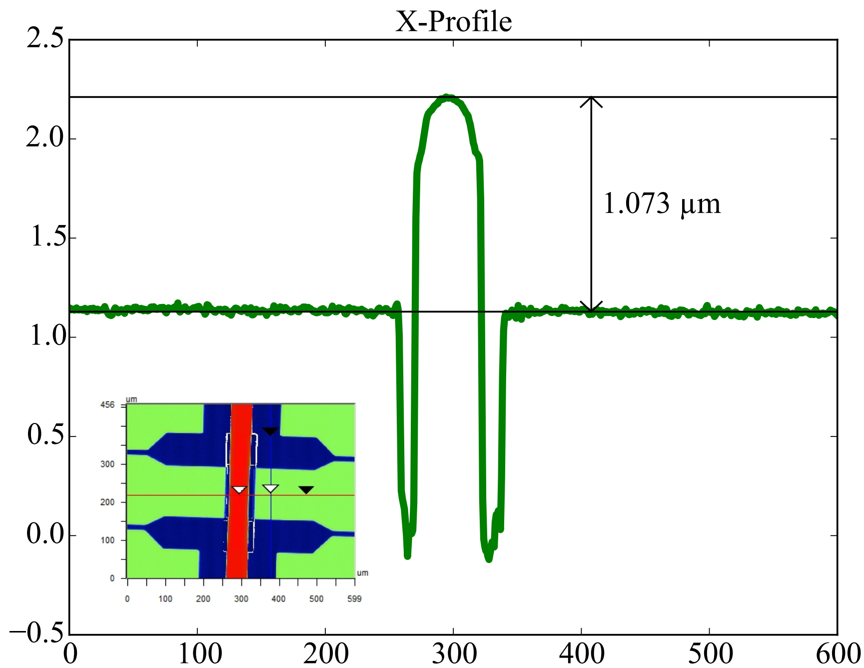

Figure 4.11: Optical profiler measurement result for an RF MEMS switch (q1c9r5) after packaging. The inlet shows the measured RF MEMS switch after the packaging process where the colors indicate thicknesses.

packaging is 28.8 V and 32.7 V, respectively. Therefore, the average increase in the actuation voltages is 3.9 V as a result of the BCB packaging process. Moreover, the deviance of the actuation voltages decreased after the packaging. That is, the actuation voltages got stabilized after the annealing process due to BCB packaging. Moreover, the center deflection of the BCB packaged switches should confirm the increase in the actuation voltages. Equation 4.1 presents the expression for the pull-in voltage of a capacitive RF MEMS switch (fixed-fixed beam).

$$V_{PI} = \sqrt{\frac{8k}{27\varepsilon_0 ws} g_0^3} \tag{4.1}$$

where, ε_0 is the electrical permittivity of free space, w is the width MEMS bridge, s is the width of the signal trace of the CPW transmission line under the MEMS bridge

Table 4.4: The actuation voltages of nine switches before and after BCB packaging process.

Switch ID	**Actuation Voltage (V)**	
	Before Packaging	After Packaging
q1c5r3	28.4	32.3
q1c9r5	29.1	33.0
q1c13r8	30.8	32.8
q1c15r2	28.4	33.8
q2c9r1	27.6	31.3
q3c6r7	28.0	33.3
q3c7r1	27.6	33.0
q3c11r3	28.4	32.3
q4c6r3	31.2	32.3
Mean	$\sim$ 28.8	$\sim$32.7
σ	1.24	0.68

and g_0 is the distance between the bottom surface of the MEMS bridge and the top surface of the silicon nitride layer under the MEMS bridge. Considering the MEMS switch q1c9r5, where the center deflection is measured before and after the BCB packaging, and the average pull-in voltages before and after the packaging given in Table 4.4. Substituting $V_{PI} = 28.8\ V$, $g_0 = 1.003{\times}10^{-6}\mu m$, $\varepsilon_0 = 8.85{\times}10^{-12}\ F/m$, $w = 50\ \mu m$, $s = 180\ \mu m$, $k \sim 225\ N/m$ may be calculated. Assuming the spring constant (k) did not change before and after the packaging much, the pull-in voltage after the packaging may be calculated by substituting $g_0 = 1.074 \times 10^{-6}\mu m$ into Equation 4.1. The pull-in voltage after the packaging can be calculated as $32.2\ V$ in confirmation with the value $32.7\ V$, which is the presented average pull-in voltage in Table 4.4.

Figure 4.12, Figure 4.13, Figure 4.14, and Figure 4.15 present the C-V measurements results of randomly chosen q1c5r3, q1c13r8, q1c15r2, and q3c7r1 switches, respectively.

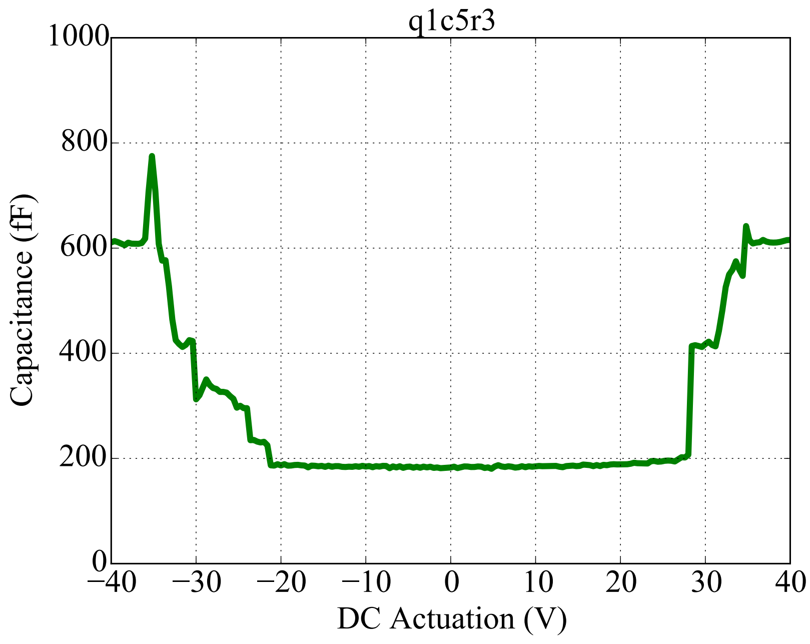

Figure 4.12: C-V measurement results of the RF MEMS switch (q1c5r3) before the BCB packaging process.

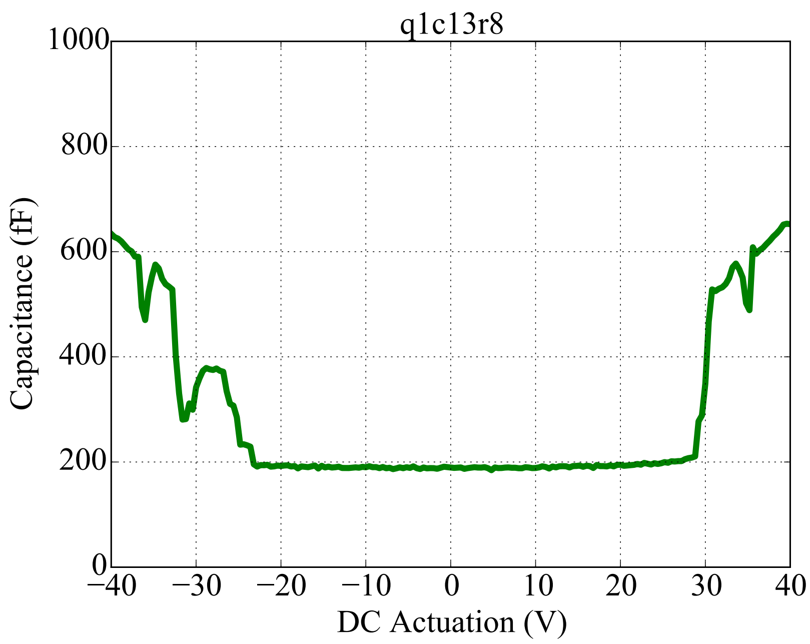

Figure 4.13: C-V measurement results of the RF MEMS switch (q1c13r8) before the BCB packaging process.

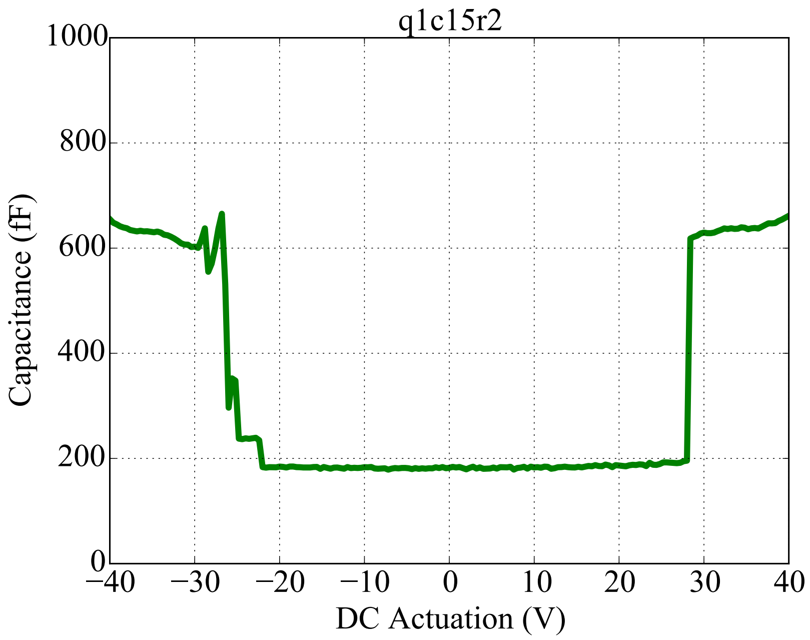

Figure 4.14: C-V measurement results of the RF MEMS switch (q1c15r2) before the BCB packaging process.

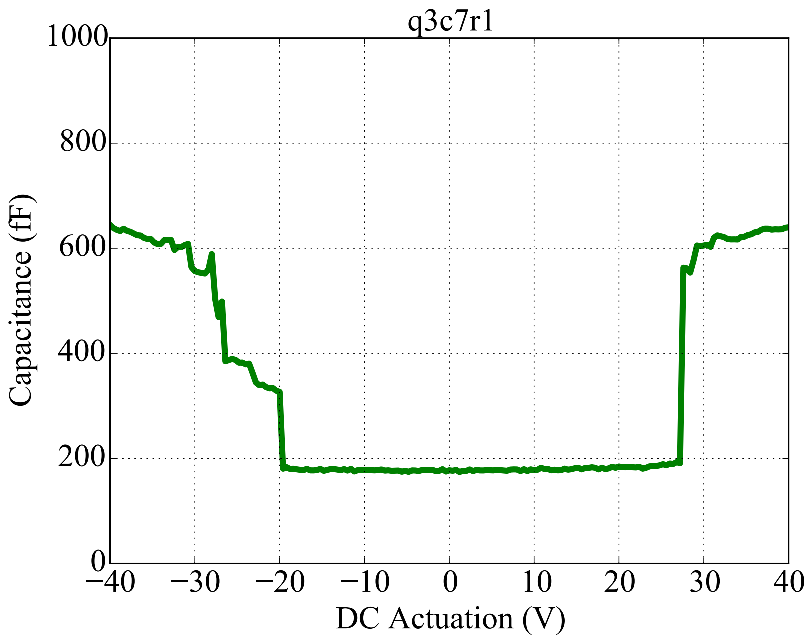

Figure 4.15: C-V measurement results of the RF MEMS switch (q3c7r1) before the BCB packaging process.

Although there are some differences between the mechanical behavior of the RF MEMS switches, the level of the upstate and downstate capacitances seem similar. Furthermore, the actuation voltages do not differ too much between the switches.

4.3.4 S-Parameter Measurements and RF Performance Analysis

An SPST RF MEMS switch has two operational states. In case of a capacitive RF MEMS switch with a fixed-fixed beam, the switch has to permit RF power transfer in the upstate. Moreover, the switch has to prevent RF power transfer from one port to the other in the downstate. In other words, the impedance matching and isolation play a crucial role in upstate and downstate, respectively.

Figure 4.6, Figure 4.7, and Figure 4.8 have already presented the EM simulation results of the packaged RF MEMS switch. The RF performance analysis investigates the S-parameter measurement results of nine predetermined packaged RF MEMS switches (the actuation analysis utilized the performances of the same switches) in comparison with the previously indicated EM simulation results. The compatibility of the EM simulation and S-parameter measurement results indicate the reliability of the EM simulation tool and the EM model. Moreover, this demonstrates the smooth realization of the simulated RF MEMS switch.

The S-parameter measurements were performed by the use of Cascade Microtech Summit 9000 Analytical Probe Station and Agilent E8361A Vector Network Analyzer (VNA). The VNA is calibrated by a Short-Open-Load-Thru (SOLT) calibration method in 1-40 GHz frequency band, utilizing Cascade 101-190 Impedance Standard Substrate (ISS). Figure 4.16 presents the measurement setup utilized in the S-parameter measurements of the 35 GHz BCB packaged RF MEMS switches. The Falco System WMA-300 high gain amplifier amplifies the actuation signal generated by Agilent 33220A function generator by a factor of 50, where Two Picosecond 5542 bias-T combines the actuation and RF signals generated by the function generator and the Agilent E8361A Vector Network Analyzer. The bias-T have the duty to protect the VNA from the actuation signals.

The package itself is crucial for the impedance matching performance of the RF

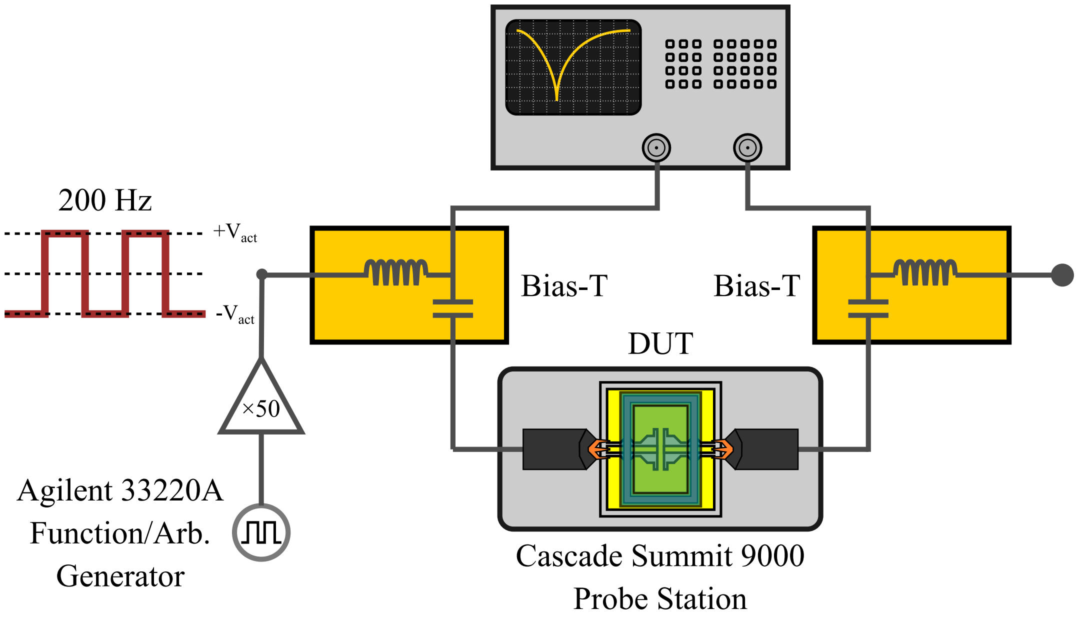

Figure 4.16: S-parameter measurement setup for the 35 GHz BCB packaged RF MEMS switches.

MEMS switches. The planar feedthrough designs include the impedance loading effects of the BCB and high-resistivity Si layers on top of the CPW transmission lines. Therefore, the presence of the package on top of the planar feedthroughs ensures impedance matching in these regions.

Figure 4.17 presents the S_{11}, and Figure 4.18 presents $\angle S_{11}$ characteristics of the EM model and nine predetermined packaged RF MEMS switches in the upstate, respectively. The worst performing switch among the nine (q2c9r1) indicates 20.7 dB return loss at 35 GHz. One of the switches (q3c7r1) reached 30 dB return loss at 35 GHz. Moreover, all of the switches have better than 17.1 dB return loss in 1-40 GHz frequency band. All of the measured switches demonstrate expected return loss characteristics, which confirms the EM simulation results and the BCB package design.

Figure 4.19 presents the $|S_{21}|$, and Figure 4.20 presents $\angle S_{21}$ characteristics of the EM model and nine predetermined packaged RF MEMS switches in the upstate, respectively. All of the packaged switches indicate better than 0.6 dB insertion loss in 1-40 GHz frequency band. The insertion loss is around 0.4 dB for all of the switches at 35 GHz. The phase of the insertion loss also indicates the good match between the EM simulation and the measurements of the packaged RF MEMS switches.

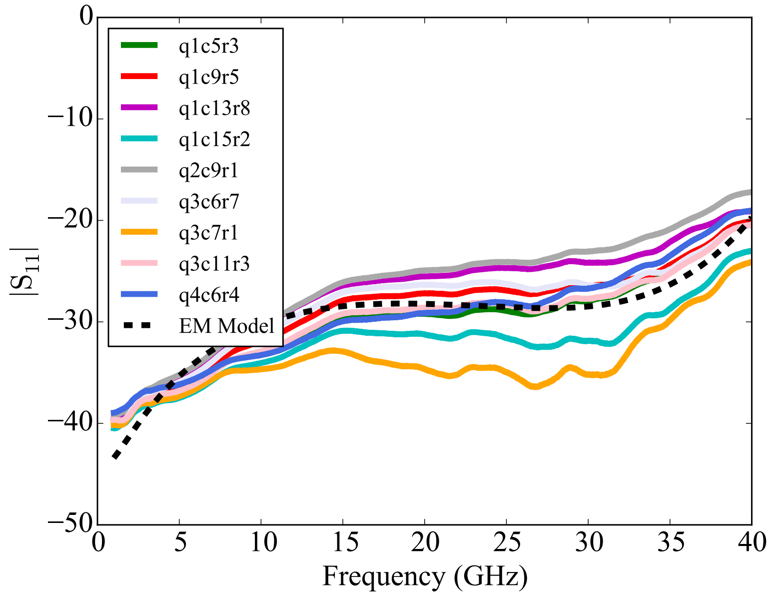

Figure 4.17: Return loss magnitude characteristics of the EM model and nine predetermined BCB packaged RF MEMS switches in the upstate.

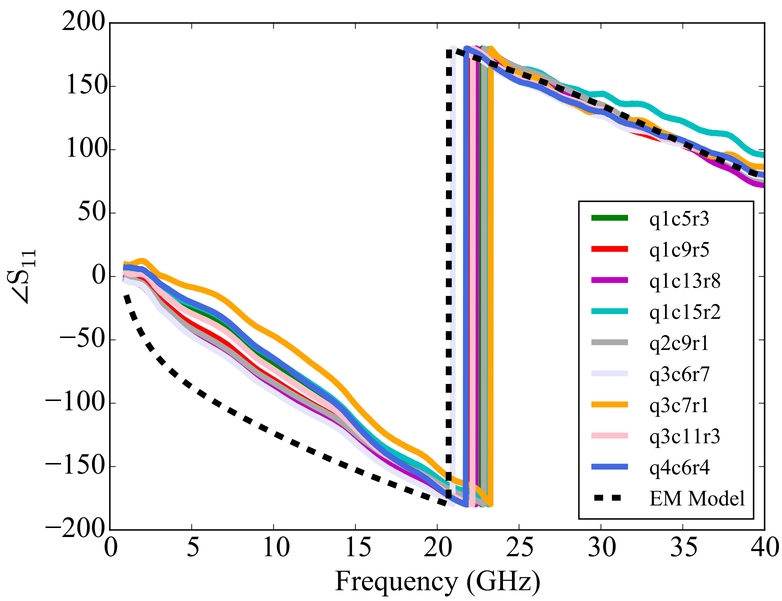

Figure 4.18: Return loss phase characteristics of the EM model and nine predetermined BCB packaged RF MEMS switches in the upstate.

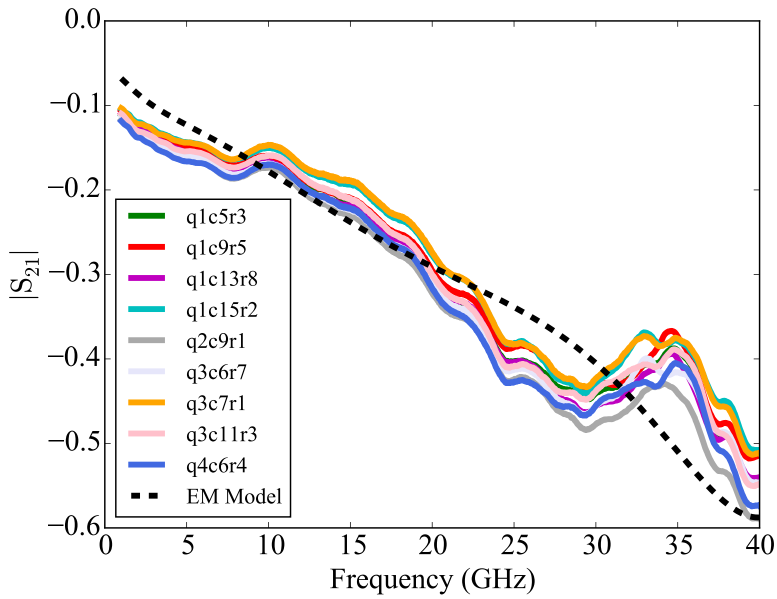

Figure 4.19: Insertion loss magnitude characteristics of the EM model and nine predetermined BCB packaged RF MEMS switches in the upstate.

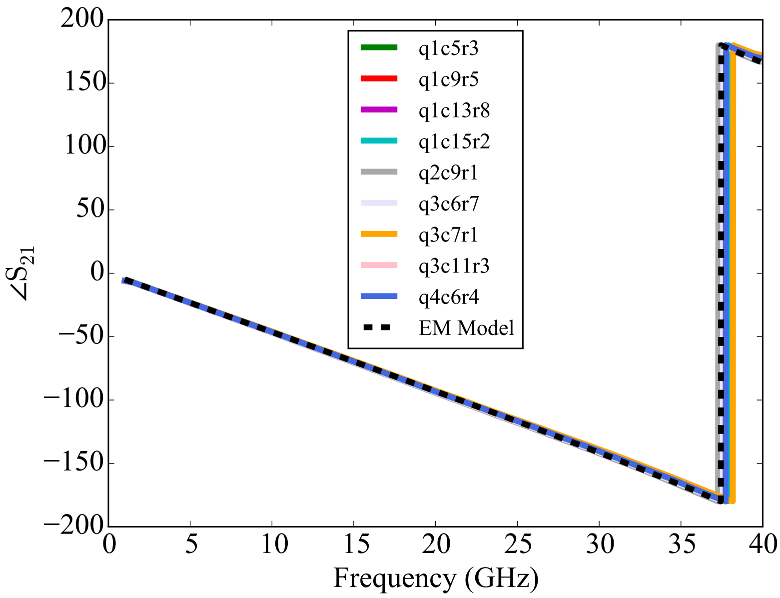

Figure 4.20: Insertion loss phase characteristics of the EM model and nine predetermined BCB packaged RF MEMS switches in the upstate.

Figure 4.21 presents the $|S_{21}|$, and Figure 4.22 presents $\angle S_{21}$ characteristics of the EM model and nine packaged RF MEMS switches in the downstate, respectively.

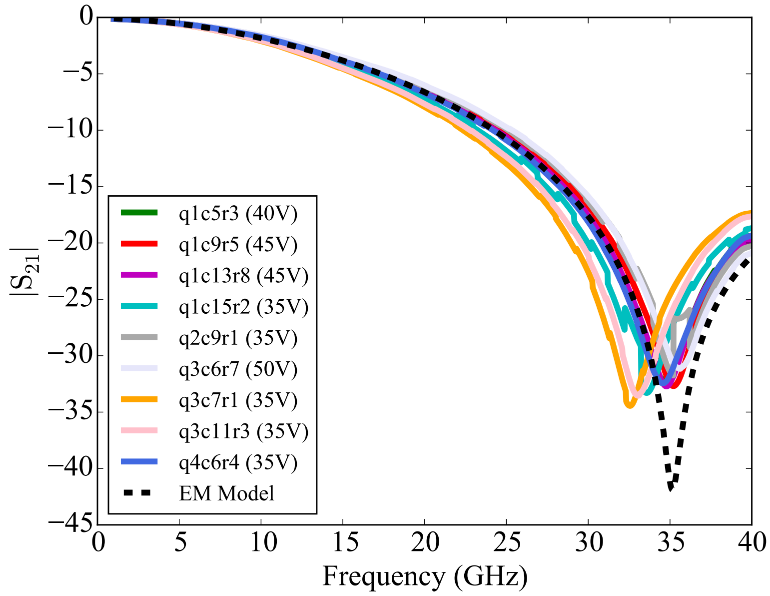

Figure 4.21: Isolation magnitude characteristics of the EM model and nine predetermined BCB packaged RF MEMS switches in the downstate.

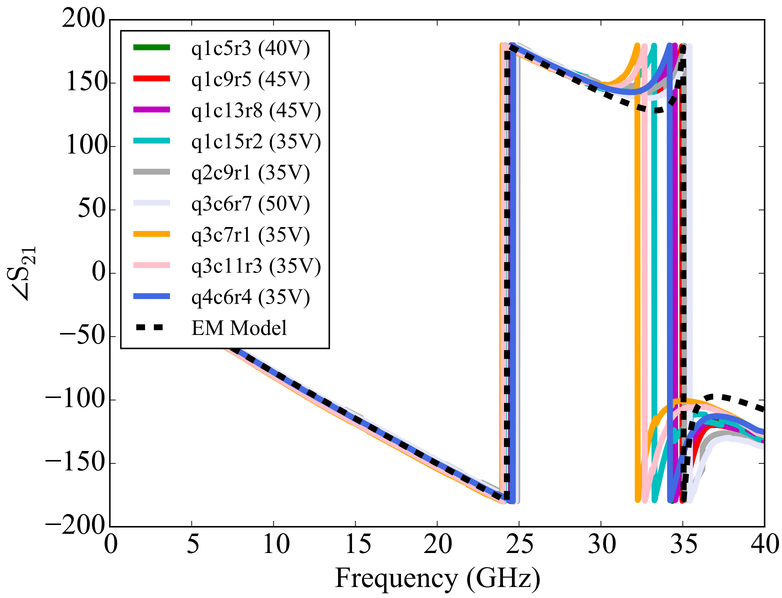

Figure 4.22: Isolation phase characteristics of the EM model and nine predetermined BCB packaged RF MEMS switches in the downstate.

It is possible to tune the isolation characteristics of all of the packaged switches to 35 GHz by applying potential differences between 35 V and 50 V. The worst performing switch in terms of isolation characteristics (q3c7r1) shows 24.6 dB isolation at 35 GHz. The isolation characteristics also demonstrate a good agreement between the EM simulation and S-parameter measurement results.

4.3.5 Switching-Time Measurements and Transient Analysis

Figure 4.23 presents the switching-time and lifetime measurement setup for BCB packaged RF MEMS switches. The setup consists of a Suss-Microtech PMV200 vacuum probe station with Suss-|Z| probes, an Agilent E8267D RF generator, an Agilent 33220A function generator, a Falco Systems WMA-300 high-voltage amplifier, a Picosecond 5542 bias-T, two WR-42 waveguide blocks, a Krytar 202A detector and an Agilent DSO6102A oscilloscope. Although the Suss-Microtech PMV200 vacuum probe station can adjust the conditions within its closed chamber, the measurements were performed at 25 °C and under 1 atm pressure. The setup applies two distinct electrical signals to the packaged RF MEMS switches during the measurements. Firstly, the Agilent E8267D RF generator provides an RF signal at 35 GHz for assessing the millimeter-wave performance of the RF MEMS switches at a single frequency. Secondly, the Agilent 33220A function generator provides a bias voltage for controlling the state of the switches. The Falco Systems WMA-300 high-voltage amplifier multiplies this bias voltage by a factor of 50. This amplified bias signal is responsible for actuating the packaged switches. The Picosecond 5542 bias-T combines the millimeter-wave signal and the bias signal, then applies the combination to the switch. The RF MEMS switch changes its state according to the bias voltage, and this generates an amplitude modulation in the 35 GHz signal. This modulated signal specifies the upstate insertion loss and the downstate isolation performance of the packaged switches. The modulated signal at the output port of the RF MEMS switch then enters the WR-42 waveguide block. This block acts as a high-pass filter: filters the low-frequency part of the modulated signal, and slightly attenuates the high-frequency part. Krytar 202A detector then filters the envelope of the output signal from the waveguide block. Agilent DSO6102A oscilloscope monitors this low-frequency envelope and can be utilized to analyze the switching-time performance and states of the switch.

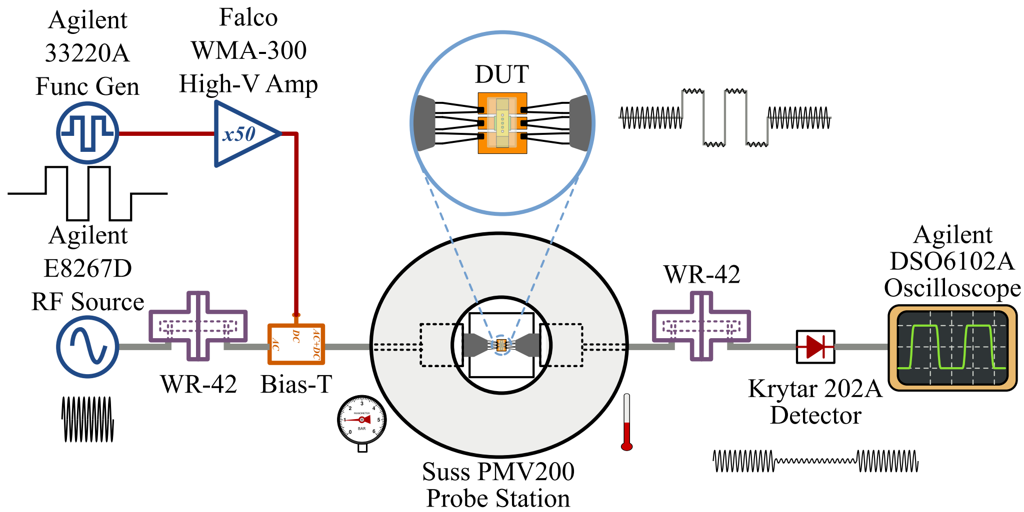

Figure 4.23: Utilized setup for the switching-time and lifetime measurements of 35 GHz BCB packaged RF MEMS switches.

Figure 4.24 presents the bias signal for actuating the packaged RF MEMS switch. When Agilent 33220A function generator set to a low-frequency (f_s) square wave with a modulated polar carrier signal (f_d), the RF MEMS switch may change state with a frequency of f_s. The RF MEMS switch stays in upstate under 0 V bias and enters downstate under $\pm V_p$. The dual-polarized square wave minimizes dielectric charging. Table 4.5 presents the characteristics of the utilized bias signal during the tests.

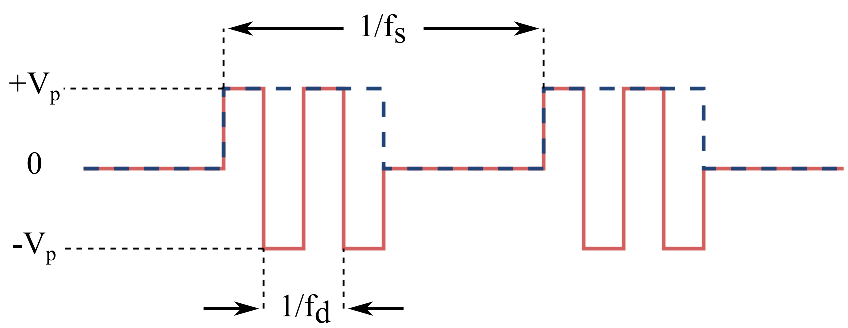

Figure 4.24: The bias signal utilized for actuating the RF MEMS switches.

The switching-time measurements were performed at 25 °C and under 1 atm. The 35 GHz carrier signal, which the RF source applies, has 16 dBm power. Excluding the cable losses ($\sim$ 10 dB), the RF MEMS switch experience 4 mW power. This value is

Table 4.5: Characteristics of the bias signal for RF MEMS switches during switching-time tests.

	f_s (kHz)	f_d (kHz)	V_p (V)
Bias Waveform	6	12	37.5

far from generating nonlinear effects.

The BCB packaged RF MEMS switches exhibit 3.5 μs fall-time (upstate to downstate) and 10 μs rise-time (downstate to upstate). Furthermore, there is 5 μs delay between the application of the bias signal and the response. Therefore, the change from downstate to upstate (rise-time) takes 8.5 μs in total for $V_p = 37.5\,V$.

4.3.6 Lifetime Measurements and Reliability Analysis

One of the BCB packaged RF MEMS switches were investigated in order to determine the lifetime and possible limiting factors of the switches. With this object in mind, the changes in the detector voltage are monitored while a BCB packaged RF MEMS switch is subject to continuous bias signal under the expressed conditions.

The performance of the RF MEMS switch undergoes some changes during the lifetime measurements. Although the switch stayed similar times in upstate and downstate in the early stages of the test, the length of the measurements favored the downstate time. The duty cycle of the square detector signal was 50.6 $\%$ after 23.7 hours of the continuous test. The duty cycle decreased to 43.4 $\%$ after 133 hours, to 31.4 $\%$ after 472 hours. This means that the switch stays longer in downstate, which is reasonable due to increasing dielectric charging effect. The charges accumulated within the silicon nitride layer continues to pull the bridge downwards even when the bias signal is 0 V. Thus, it becomes harder for the switch to change the state from downstate to upstate. The increase in the rise-time during the lifetime tests also verify this effect. Besides these changes in the performance, the RF performance of the packaged RF MEMS switch at 35 GHz hardly alters. Table 4.6 presents a comparison of the BCB packaged METU RF MEMS switch in terms of lifetime performances of the capacitive contact RF MEMS switches and capacitors in the literature.

Table 4.6: Reliability and package information of the capacitive contact RF MEMS switches and capacitors [55, 56].

	Actuator	Material	Substrate	Pull-in	Package	Lifetime	Downstate Time (h)	RF Power	Cycle Frequency
MEMtronics [57]	Bridge	Al	Glass	25-40 V	Wafer Level Liquid	>100 b	4̃8	20 dBm	20-40 kHz
Raytheon [8, 58]	Bridge	Al	Si	30-40 V	Hermetic Wafer Cap	>200 b	N/A	20 dBm	5 kHz
WISPRY [55]	Cantilever	Al	Si	35 V	Semihermetic Wafer Cap	N/A	N/A	N/A	N/A
UCSD [60]	Cantilever	Au	Fused Silica	30-40 V	Unpackaged	>10 b	186	29 dBm	8 kHz
UCSD [61]	Bridge	Au	Fused Silica	30-40 V	Unpackaged	>20 b	N/A	30 dBm	50 kHz
Limoges [62]	Cantilever	Au	Fused Silica	60 V	Unpackaged	>20 b	N/A	10 dBm	N/A
NXP [63]	Bridge	Al-Cu	Si	30 V	Hermetic Wafer Cap	N/A	N/A	N/A	N/A
METU [18]	Bridge	Au	Glass	30-50 V	Semihermetic Wafer Cap	>10 b	236	16 dBm	12 kHz

4.3.7 Power Handling of RF MEMS Switches

As expressed the switching-time and lifetime measurements were performed under 16 dBm power. Although the power handling capability of the RF MEMS switch is not investigated by applying different power levels, it is possible to approximately calculate it using the self-actuation concept [55].

The return loss of the BCB packaged RF MEMS switches at 35 GHz is around 30 dB. Therefore, the characteristic impedance of the switch might be assumed to be 50.1 Ω. Equation 4.2 expresses the DC-equivalent potential difference for the RF signal for self actuation to occur, where V_{pk} is the peak amplitude value of the RF signal. In this regard it is assumed that the MEMS bridge did not deflect before pull-in. The C-V measurement curves in Figure 4.12, Figure 4.13, Figure 4.14, and Figure 4.15 supports this idea, where the upstate capacitance is almost contant until actuation voltage is reached.

$$V_{DC-eq} = \frac{V_{pk}}{\sqrt{2}} = \sqrt{P \times Z_0} \tag{4.2}$$

For $P = 4$ mW RF power and $Z_0 = 50.1\ \Omega$, $V_{DC-eq} = 0.316$ V may be calculated. This clearly shows that the effect of the self-actuation mechanism is far from affecting the pull-in voltages expressed in Table 4.4. In order to have the BCB packaged RF-MEMS switch to self actuate, $V_{DC-eq} \geq V_{PI}$ must be satisfied. In this regard, for the BCB packaged RF MEMS switches to self actuate, an RF signal with $V_{pk} = 46.24$ V or $P = 21.34$ W must be applied during the measurements.

CHAPTER 5

SENSITIVITY ANALYSIS FOR THE BCB PACKAGE

Process variations due to equipment drifts and process condition differences might often be encountered during a fabrication. These variations may degrade the performance of the fabricated devices. While a parameter drift might not affect the performance at all, another might do. Therefore, analyzing the sensitivity of a component according to possible process variations is significant.

Working on this concept by fabricating components and measuring their performances would take so much time and effort. Therefore, this method is not appropriate. Using EM simulation tools would be a faster and easier method. Considering the consistency between the EM simulation results and RF measurement results of the BCB packaged RF MEMS switches, it is meaningful to use the EM simulation tools.

The fabrication process of the RF MEMS switches is complicated when compared with the BCB packaging process. On the other hand, the packaging process only needs two masks, where the BCB layer and the cavities on the cap wafer are patterned. This simple process flow decreases any possible process variations. In this study, four possible variations are considered, which might occur during the fabrication. These four possible variations might occur in BCB thickness, BCB lane width, $\mathrm{Si_xN_y}$ thickness, and cavity depth. Moreover, a fifth possible BCB permittivity (ϵ_{BCB}) variation is considered. The process variations might not change the BCB permittivity. However, it is useful to investigate the effects of such a change. The utilized relative permittivity for the BCB layer in EM simulations is 2.6. This value is an assumption at 35 GHz because it does not take the frequency dependence of the dielectric permittivity into account.

Each possible process variation (process variable) is expected to affect the package performance differently. Therefore, first of all, the effects of each process variable should be independently observed. A set of simulations should sweep a single variable for achieving such a feat. Investigating each simulation result can reveal the worst-case scenario for the package performance. The worst-case may not be the combination of worst-performing parameter values. The parameter effects supporting each other will form the worst-case scenario.

This chapter presents the investigation results of each process variable under the corresponding sections. Section 5.1 presents the effects of BCB thickness variations. Section 5.2 then indicates the effects of BCB lane width variations. The effects of $\mathrm{Si_xN_y}$ thickness on the package performance is presented in Section 5.3. Section 5.4 focuses on the effects of cavity depth variations. Section 5.5 gives detailed information on the effects of BCB permittivity variations on package performance. Finally, Section 5.6 investigates the combined effects of all these independent parameters as the worst-case.

5.1 BCB Thickness Variations

The process conditions (i.e., spin coating speed) were optimized, aiming 10 µm BCB thickness. However, a non-uniformity on the wafer may result in a slightly different BCB thickness. Equipment settings might also lead to a possible thickness variation. The variations in the BCB thickness may have an impact on the RF performance of the package. Therefore, BCB thickness is swept in the EM simulations.

The BCB thickness is decreased down to 9 µm by 0.5 µm steps and increased up to 11 µm again by 0.5 µm steps. In other words, each BCB thickness required a different EM simulation. A 1 µm difference in the targeted thickness is not logical. Nevertheless, the analysis has to include the worst possible cases. Both upstate and downstate performances of the 35 GHz BCB packaged RF MEMS switch are parts of the analysis. Five variation points require ten EM simulations considering the upstate and downstate of the switch. Figure 5.1, Figure 5.2, and Figure 5.3 present $|\mathrm{S}_{11}|$ and $|\mathrm{S}_{21}|$ graphs in upstate and $|\mathrm{S}_{21}|$ in downstate, respectively.

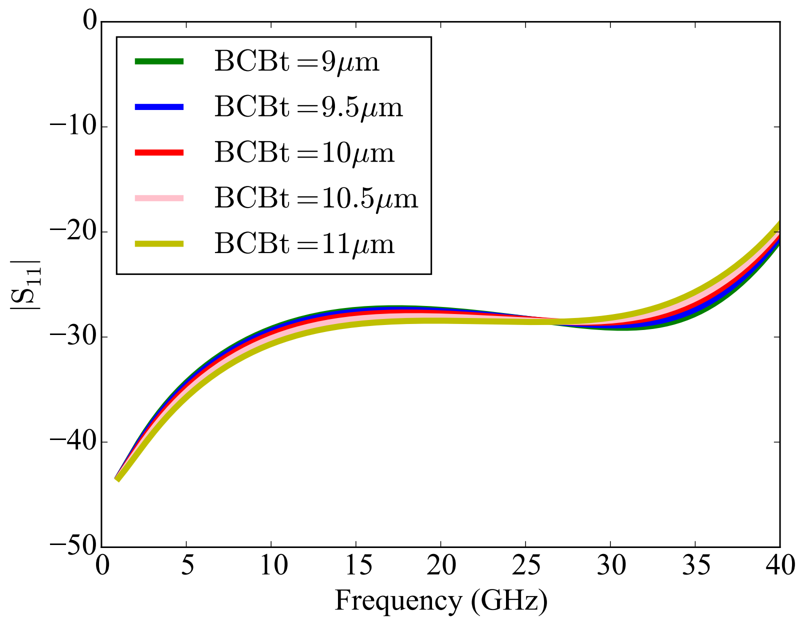

Figure 5.1: $|S_{11}|$ performance of the BCB packaged 35 GHz RF MEMS switch in the upstate while the BCB thickness is swept from 9 μm to 11 μm.

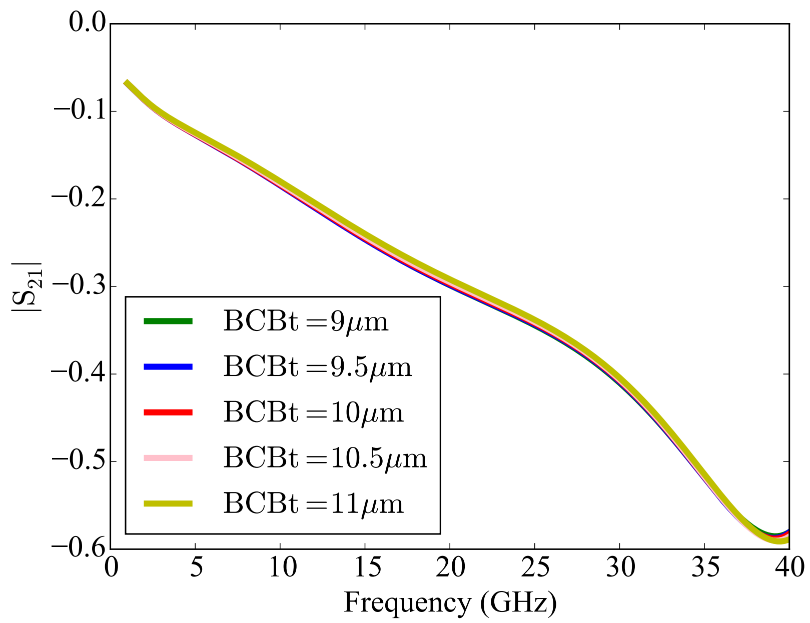

Figure 5.2: $|S_{21}|$ performance of the BCB packaged 35 GHz RF MEMS switch in the upstate while the BCB thickness is swept from 9 μm to 11 μm.

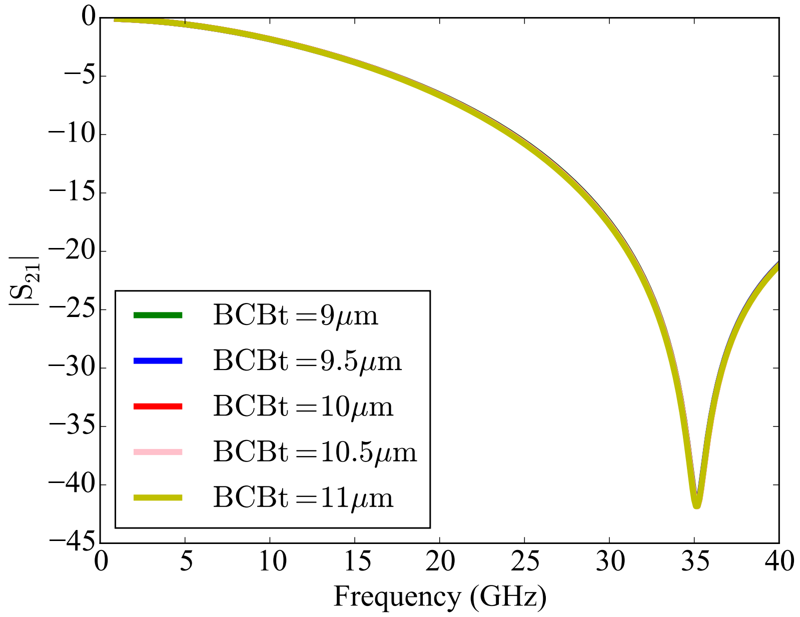

Figure 5.3: $|S_{21}|$ performance of the BCB packaged 35 GHz RF MEMS switch in the downstate while the BCB thickness is swept from 9 µm to 11 µm.

As expected from the BCB thickness change, the parameter did not affect the upstate or downstate performance of the RF MEMS switch. It is the MEMS bridge which is responsible for tuning the frequency. Although altering the BCB thickness disturbs the return loss performance in the upstate, the effect is not severe. Since BCB thickness changes the characteristic impedance of the BCB transition region, this result is also expected. Nevertheless, the change is insignificant — the worst-case shows itself when the BCB thickness is 9 µm. The return loss is still better than 25 dB at 35 GHz for 9 µm BCB thickness. Therefore, it is safe to say that the BCB package structure is insensitive against BCB thickness variations.

5.2 BCB Lane Width Variations

The BCB width in the developed BCB package is chosen to be 200 µm. However, it is possible to obtain a slightly different BCB width due to overexposure during the mask alignment step. Moreover, just because of the applied force at 250 °C, during the BCB bonding process, the width of the BCB lanes might increase. The BCB width is increased up to 240 µm by 10 µm steps in the EM simulations, in order to observe the effects of these possible changes. In other words, there were five different width points, for which EM simulations were performed. Again it is not probable to have 40 µm extension in the BCB width, but the analysis is done for worst possible cases. The analysis is made for both upstate and downstate performances of the 35 GHz BCB packaged RF MEMS switch. $|S_{11}|$, and $|S_{21}|$ graphs in the upstate and $|S_{21}|$ graphs in the downstate are presented in Figure 5.4, Figure 5.5, and Figure 5.6, respectively.

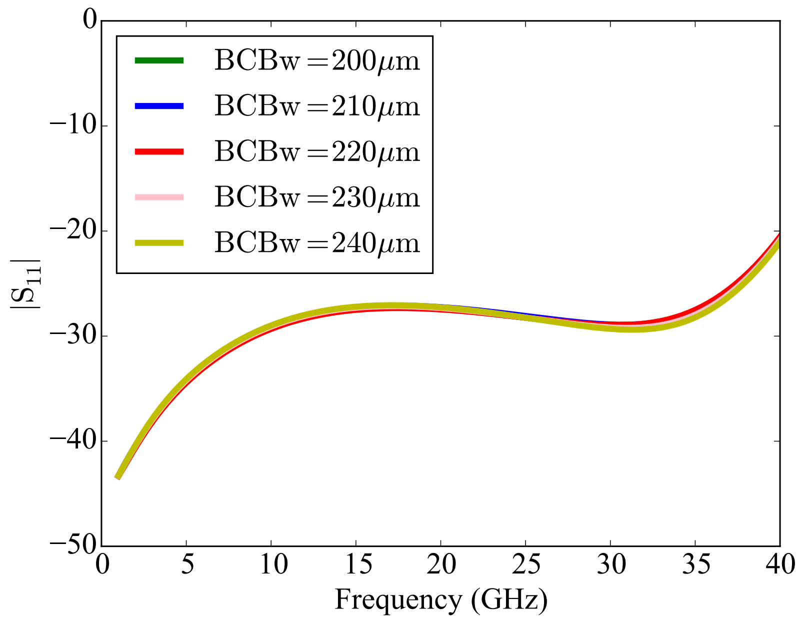

Figure 5.4: $|S_{11}|$ performance of the BCB packaged 35 GHz RF MEMS switch in the upstate while the BCB lane width is swept from 200 µm to 240 µm.

As expected from the BCB lane width change, the parameter did not affect the upstate or the downstate performance of the RF MEMS switch. Although it is not serious, the return loss performance is disturbed as we alter the BCB width. This result is expected because a change in the BCB width did alter the characteristic impedance of the Si transition sections in Figure 3.2. Nevertheless, the change is insignificant due to the Si ($\epsilon_{r,Si} = 11.9$) presence on top of the low permittivity BCB ($\epsilon_{r,BCB} = 2.6$) layer. The worst case is observed when the BCB width is increased to 250 µm, and return loss was still better than 30 dB at 35 GHz. Therefore, it is safe to say that the BCB package structure is insensitive against BCB lane width variations.

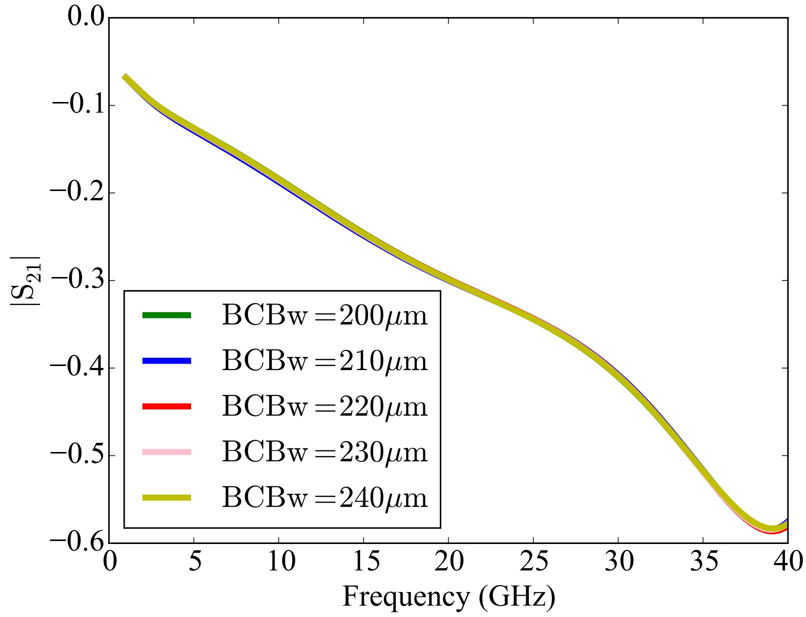

Figure 5.5: $|S_{21}|$ performance of the BCB packaged 35 GHz RF MEMS switch in the upstate while the BCB lane width is swept from 200 µm to 240 µm.

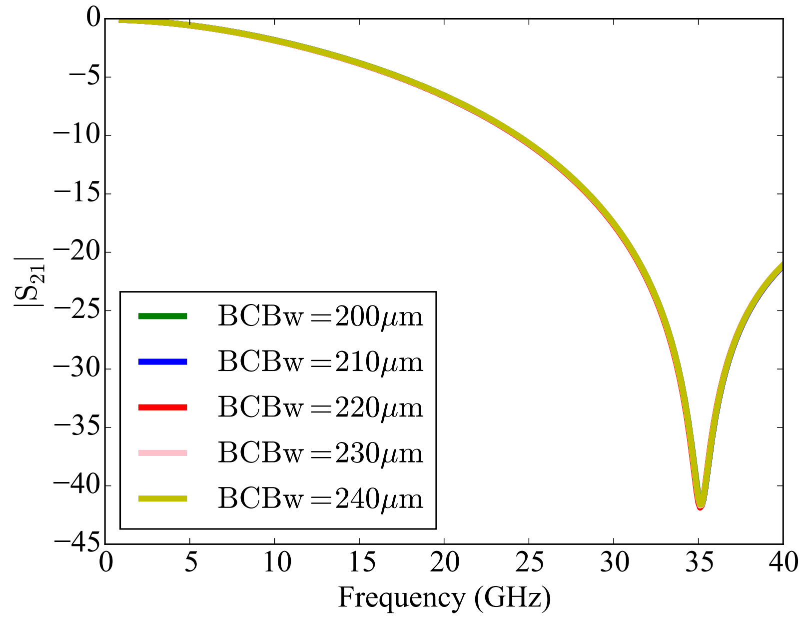

Figure 5.6: $|S_{21}|$ performance of the BCB packaged 35 GHz RF MEMS switch in the downstate while the BCB lane width is swept from 200 µm to 240 µm.

5.3 Si_xN_y Thickness Variations

The Si_xN_y thickness in the packaged RF MEMS switch is chosen to be 0.2 µm under the BCB ring. The Si_xN_y thickness under the MEMS bridge is 0.3 µm. However, it is possible to obtain a slightly different Si_xN_y thickness due to PECVD equipment drifts. Furthermore, the TMAH etching step may decrease the Si_xN_y thickness as well. The Si_xN_y thickness is swept from 0.18 µm to 0.22 µm, with 0.01 µm steps. In other words, there were 5 different thickness points, for which EM simulations were performed. 0.02 µm alteration in the Si_xN_y thickness is possible in the worst case and this is accounted for in the simulations. The analysis is made for both upstate and downstate performances of the 35 GHz BCB packaged RF MEMS switch. $|S_{11}|$ and $|S_{21}|$ graphs in the upstate and $|S_{21}|$ in the downstate are presented in Figure 5.7, Figure 5.8, and Figure 5.9, respectively.

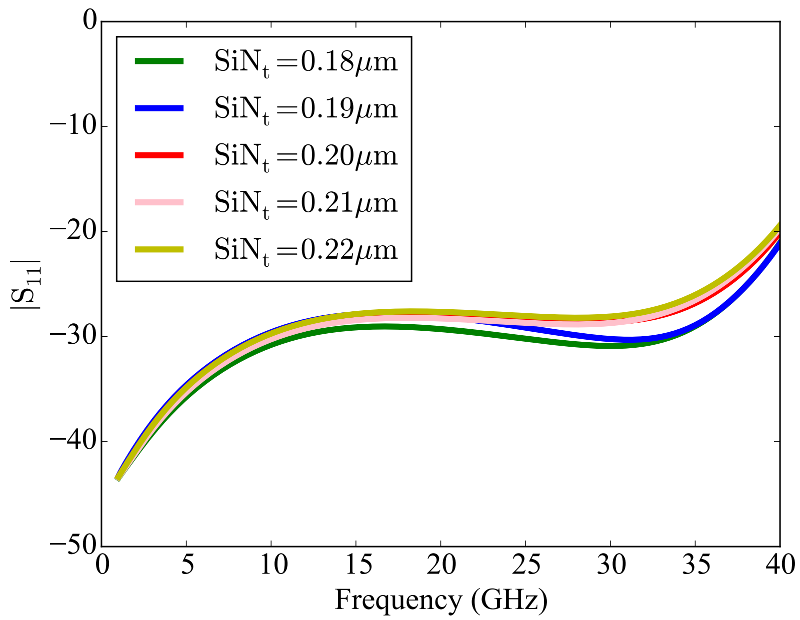

Figure 5.7: $|S_{11}|$ performance of the BCB packaged 35 GHz RF MEMS switch in the upstate while the Si_xN_y thickness is swept from 0.18 µm to 0.22 µm.

The Si_xN_y is not only utilized under the BCB rings for better adhesion but also it is utilized under the MEMS bridges for electrical isolation. So changing the thickness of the Si_xN_y layer alters two different mechanisms. Therefore, both mechanisms should be investigated. The Si_xN_y thickness seemed not to affect the return loss and insertion

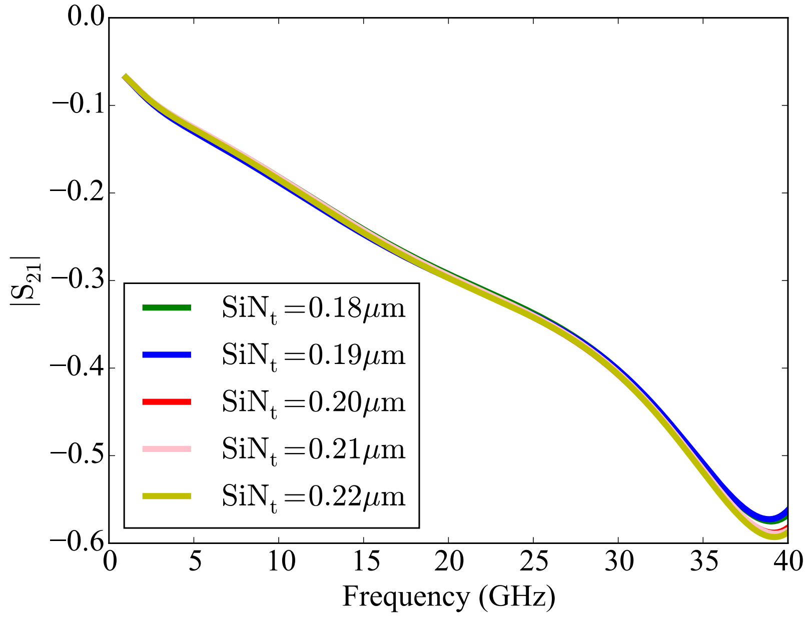

Figure 5.8: $|S_{11}|$ performance of the BCB packaged 35 GHz RF MEMS switch in the upstate while the Si_xN_y thickness is swept from 0.18 µm to 0.22 µm.

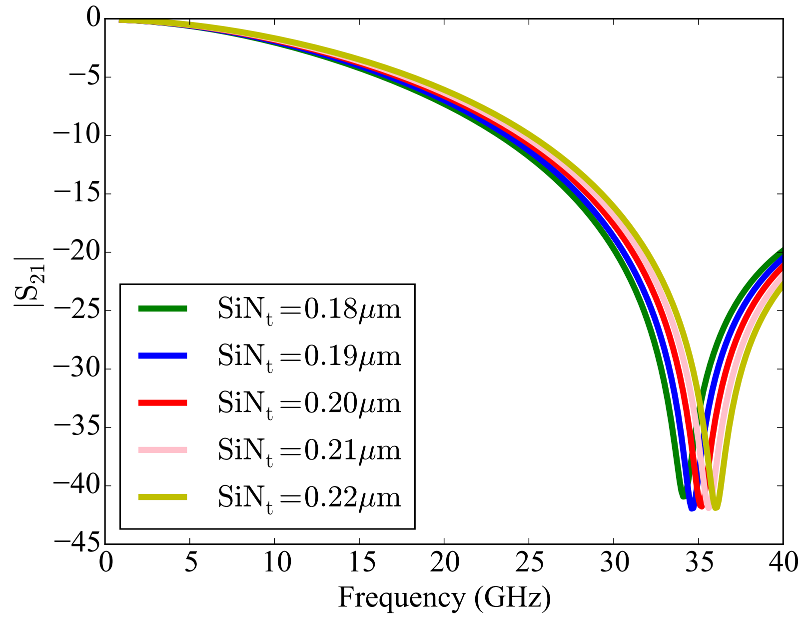

Figure 5.9: $|S_{21}|$ performance of the BCB packaged 35 GHz RF MEMS switch in the downstate while the Si_xN_y thickness is swept from 0.18 µm to 0.22 µm.

loss of the packaged RF MEMS switch in the upstate significantly. Both mechanisms affected the return loss and insertion loss in the upstate. First of all, the change in the thickness of the isolation dielectric (Si_xN_y) altered the upstate capacitance. Secondly, the impedance of the planar feedthroughs was affected, which altered the performances in the upstate.

Moreover, the isolation performance of the packaged RF MEMS switch in the downstate was affected significantly. The shift in the frequency is mostly due to the change in the downstate capacitance. The downstate capacitance is changed because of the thickness of the isolation dielectric (Si_xN_y) and the downstate capacitance is directly related. The change in the planar feedthrough regions does not expect to affect the isolation performance. The change in the thickness of the isolation dielectric is a process variable for the fabrication of the RF MEMS switches. Thus, the package itself can be assumed to be insensitive against Si_xN_y thickness changes.

5.4 Cavity Depth Variations

The cavity depth in the packaged RF MEMS switch is chosen to be 100 µm. However, it is possible to obtain a slightly different cavity depth due to DRIE non-uniformity through the wafer and, equipment drifts are also plausible. The cavity depth is swept from 50 µm to 150 µm, with 25 µm steps. In other words, there were five different thickness points, for which EM simulations were performed. 50 µm alteration in the cavity depth is possible but not likely; however, the worst case is accounted for in the simulations. The analysis is made for both upstate and downstate performances of the 35 GHz BCB packaged RF MEMS switch. $|S_{11}|$ and $|S_{21}|$ graphs in the upstate, and $|S_{21}|$ graph in downstate are presented in Figure 5.10, Figure 5.11, and Figure 5.12, respectively.

As expected from the cavity depth change, the parameter did only affect the upstate performance of the RF MEMS switch slightly. This result is expected because a change in the cavity depth did alter the characteristic impedance of the Si cavity section in Figure 3.2. However, when the cavity depth is over 50 µm, its effect is negligible. The BCB package is stable against cavity depth changes.

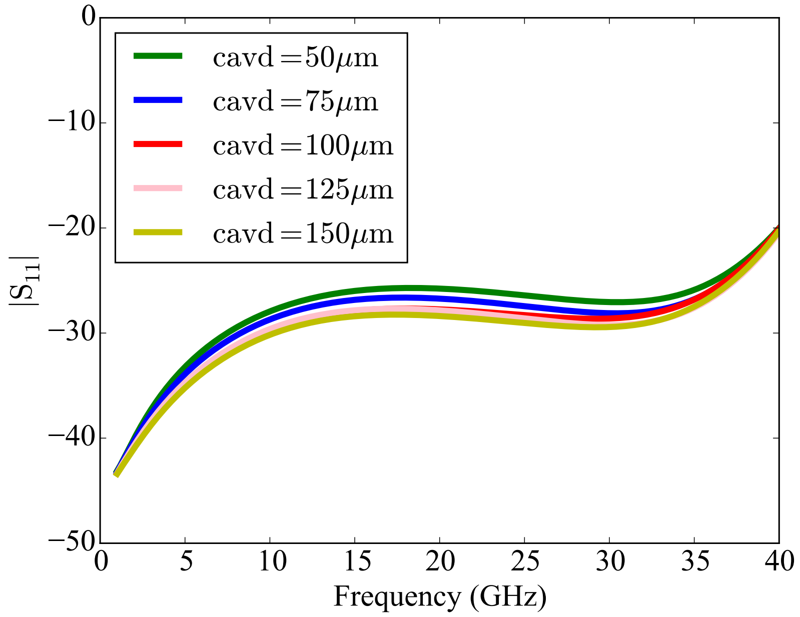

Figure 5.10: $|S_{11}|$ performance of the BCB packaged 35 GHz RF MEMS switch in the upstate while the cavity depth is swept from 50 µm to 150 µm.

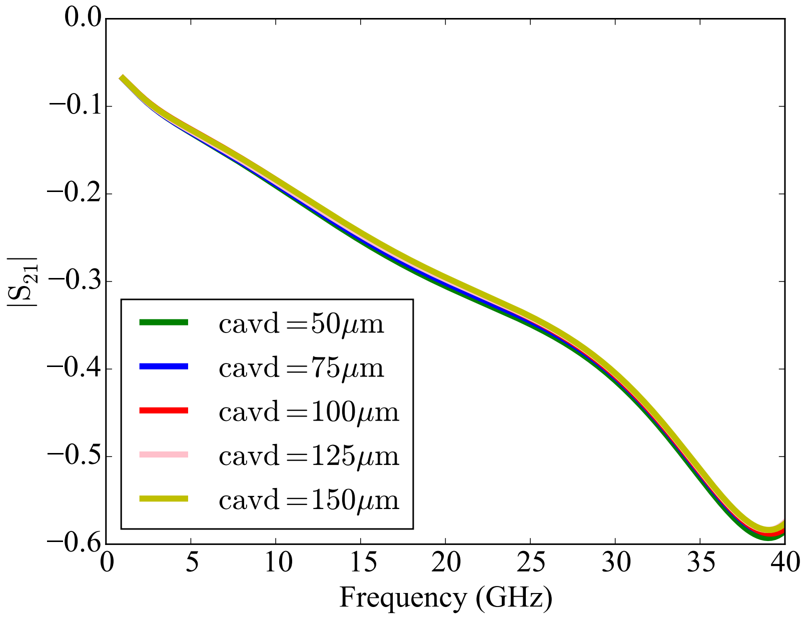

Figure 5.11: $|S_{21}|$ performance of the BCB packaged 35 GHz RF MEMS switch in the upstate while the cavity depth is swept from 50 µm to 150 µm.

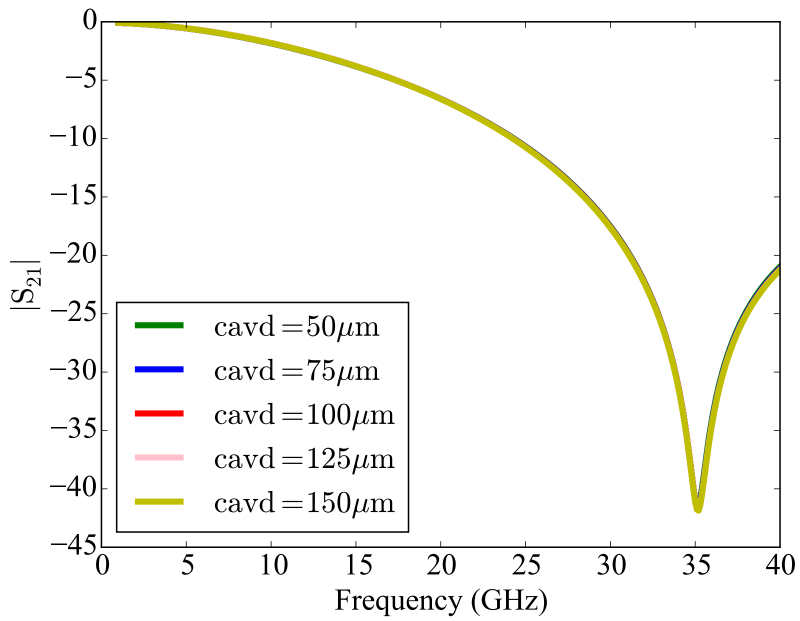

Figure 5.12: $|S_{21}|$ performance of the BCB packaged 35 GHz RF MEMS switch in the downstate while the cavity depth is swept from 50 µm to 150 µm.

5.5 BCB Relative Permittivity Variations

The BCB relative permittivity is taken to be 2.6 in the EM model. However, it is possible to have a different BCB relative permittivity when the frequency effect is considered. Until the BCB characterizations are extended up to 35 GHz, it is not possible to give an exact number for its value. The BCB relative permittivity is swept from 2.4 to 2.6, with 0.5 steps. In other words, there were five different points, for which EM simulations were performed. The analysis is made for both upstate and downstate performances of the 35 GHz BCB packaged RF MEMS switch. $|S_{11}|$ and $|S_{21}|$ graphs in upstate and $|S_{21}|$ graphs in downstate are presented in Figure 5.13, Figure 5.14, and Figure 5.15, respectively.

Sweeping the relative permittivity of the BCB almost did not affect the insertion loss and return loss performance in the upstate and isolation performance in the downstate. These results indicate the insensitivity of the BCB package against changes in the relative permittivity of the BCB.

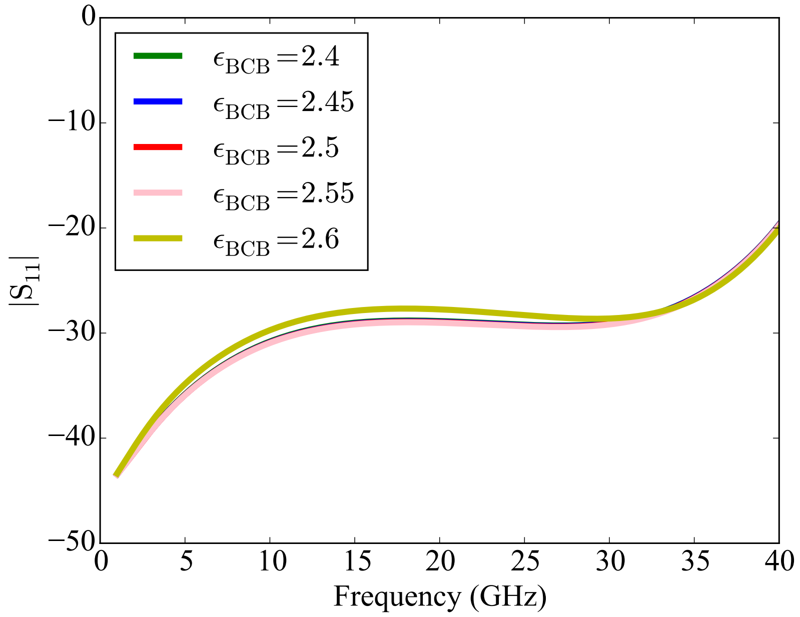

Figure 5.13: $|S_{11}|$ performance of the BCB packaged 35 GHz RF MEMS switch in the upstate while the BCB relative permittivity is swept from 2.4 to 2.6.

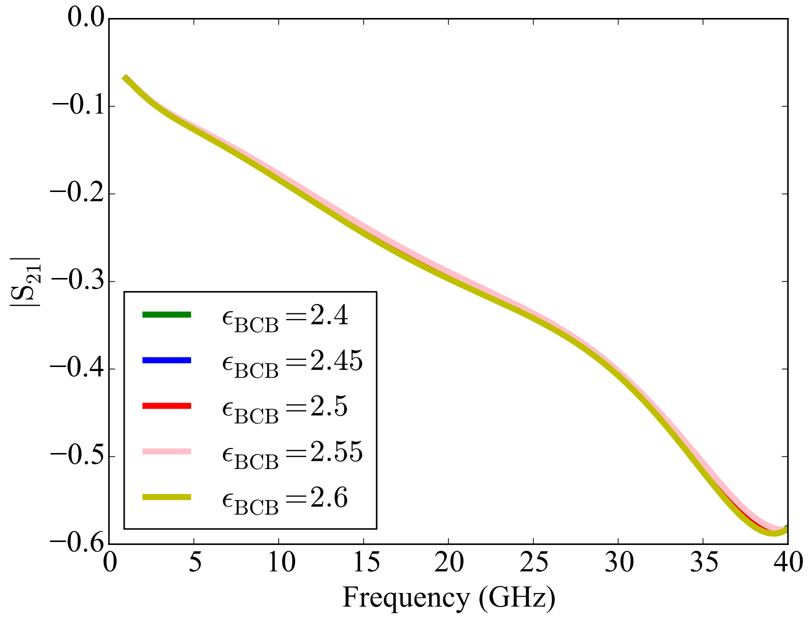

Figure 5.14: $|S_{21}|$ performance of the BCB packaged 35 GHz RF MEMS switch in the upstate while the BCB relative permittivity is swept from 2.4 to 2.6.

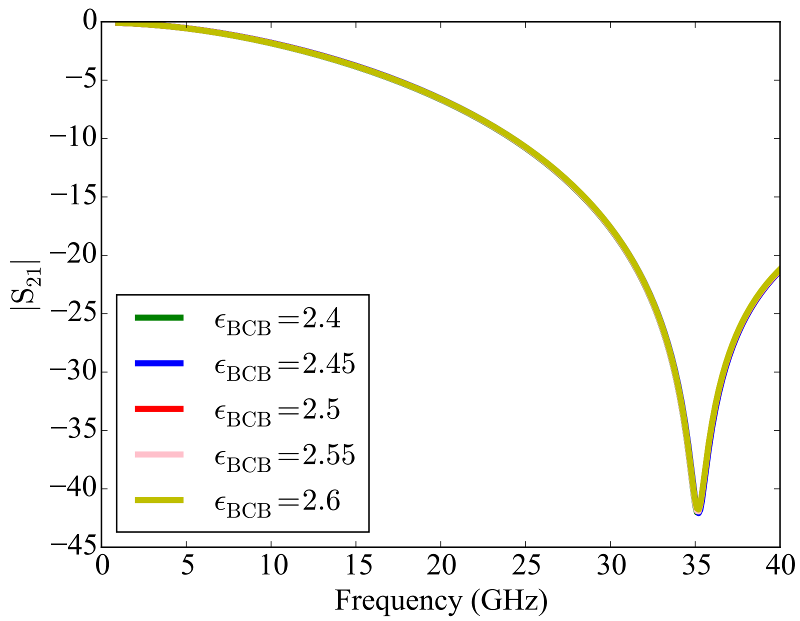

Figure 5.15: $|S_{21}|$ performance of the BCB packaged 35 GHz RF MEMS switch in the downstate while the BCB relative permittivity is swept from 2.4 to 2.6.

5.6 The Worst Case Scenario

In the worst-case scenario, it is assumed that all the alterations in the BCB thickness, BCB width, Si_xN_y thickness, cavity depth, and BCB relative permittivity are the least expected values. Nevertheless, care has been taken in order not to cancel each discrete effect. For instance, the BCB relative permittivity is kept at 2.6 instead of 2.4. Otherwise, decreasing the BCB thickness would be less effective in the overall switch performance. Table 5.1 presents the tabulated worst-case parameter values.

The analysis is made for both upstate and downstate performances of the 35 GHz BCB packaged RF MEMS switch. In order to have a reference, the worst-case scenario performances are drawn together with the designed switch performances. $|S_{11}|$ and $|S_{21}|$ graphs in the upstate and $|S_{21}|$ graph in the downstate are presented in Figure 5.16, Figure 5.17, and Figure 5.18, respectively.

The performance of the BCB packaged RF MEMS switch in the upstate is affected in the worst-case scenario. Especially, the return loss performance is altered. However, a 3 dB change around 30 dB return loss is negligible. Moreover, the insertion

Table 5.1: Parameter values of the BCB packaged 35 GHz RF MEMS switch considering the worst case scenario.

PARAMETER	VALUE
BCB Thickness (BCB_t)	9 µm
BCB Lane Width (BCB_w)	240 µm
SixNy Thickness (Si_xN_y)	0.18 µm
Cavity Depth (cav_d)	50 µm
Relative Permittivity of BCB (ϵ_{BCB})	2.6

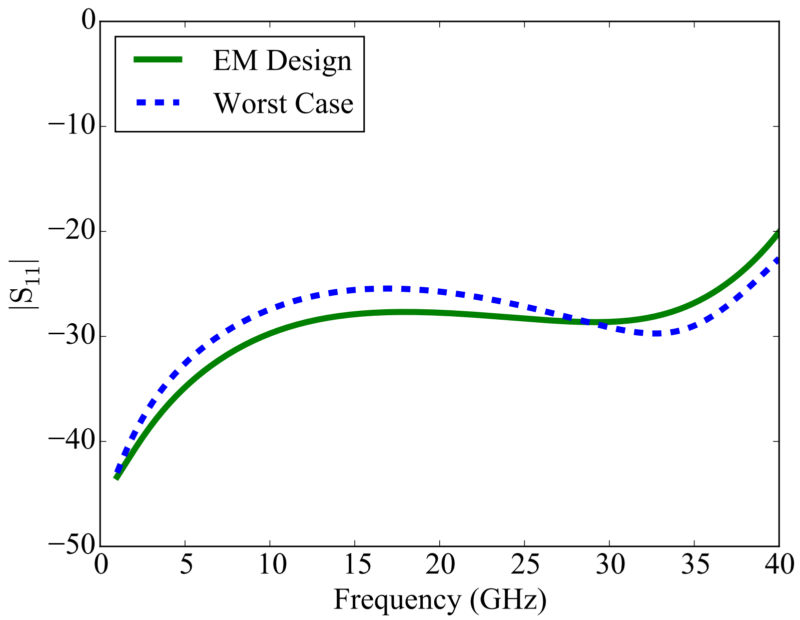

Figure 5.16: $|S_{11}|$ performance of the BCB packaged 35 GHz RF MEMS switch in the upstate for the worst case scenario and for its regular design.

loss is not affected significantly as expected from the return loss characteristics. On the other hand, tuned downstate performance is shifted to lower frequencies. None of the parameters did affect the isolation of the packaged switch except the Si_xN_y thickness. Thus, the change in the isolation is due to the change in isolation dielectric thickness under the MEMS bridge. For the worst-case scenario, the Si_xN_y thickness is decreased to 0.18 µm from 0.20 µm. This alteration explains the shift to lower frequencies, where the downstate capacitance of the RF MEMS switch is increased.

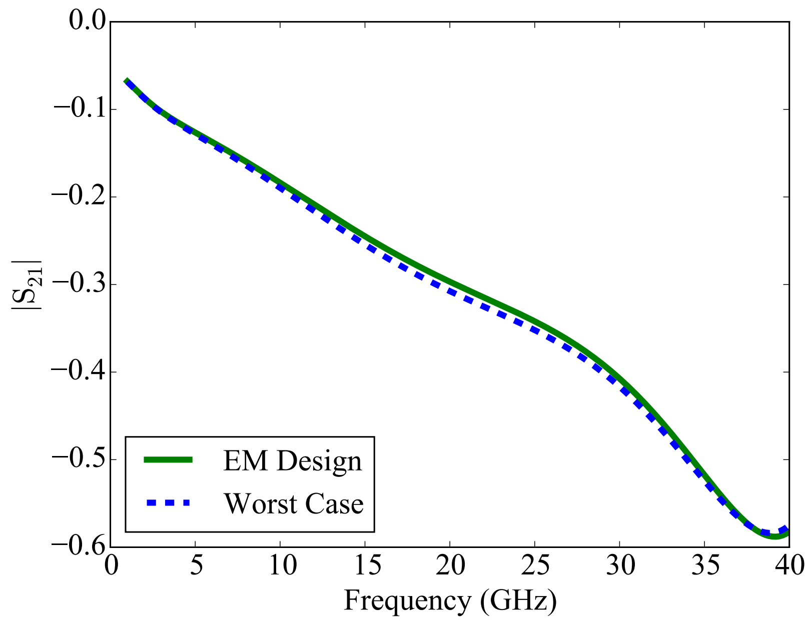

Figure 5.17: $|S_{21}|$ performance of the BCB packaged 35 GHz RF MEMS switch in the upstate for the worst case scenario and for its regular design.

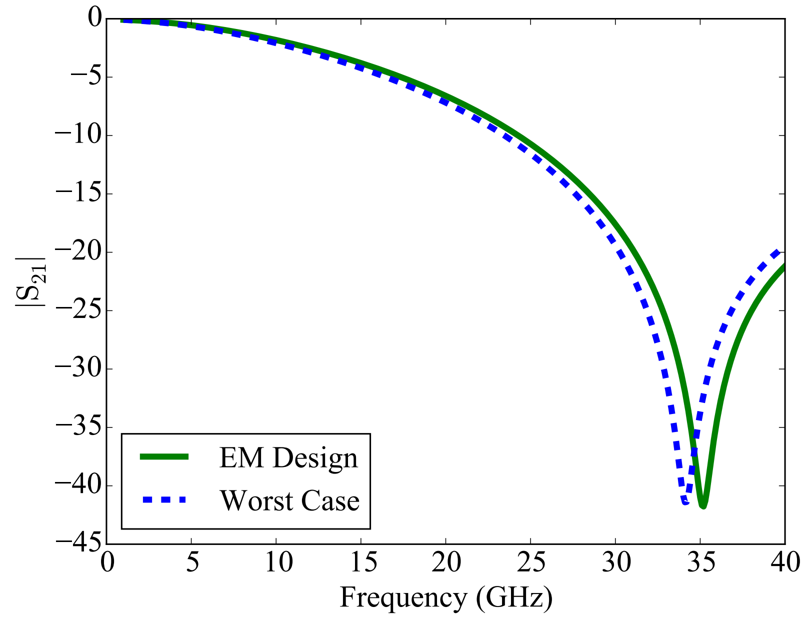

Figure 5.18: $|S_{21}|$ performance of the BCB packaged 35 GHz RF MEMS switch in the upstate for the worst case scenario and for its regular design.

CHAPTER 6

INVESTIGATION OF THE DISPERSIVE BEHAVIOR OF GLASS AND HIGH-RESISTIVITY SILICON SUBSTRATES

Knowing the properties of the utilized materials in a fabrication cycle has an undeniable significance. Accurately characterized materials are crucial for estimating the performance of a device. Moreover, reliable and accurate designs depend on the accuracy of the material characterization. The characterization has even more significance when RF components of any sort are under consideration. This situation is due to the frequency dependence of the material properties. The permittivity of a dielectric may strongly depend on the frequency of operation. This dependence may alter performance significantly.

Utilized substrate (i.e., silicon, glass, quartz) has a significant effect on the RF performance of the devices. The BCB packaging process presented in Chapter 2 is valuable, and it is insensitive against process variations. Nevertheless, utilized substrates should be characterized to have better control over it. In the developed BCB packaging approach, a glass substrate carries the RF MEMS switches. Afterward, a high-resistivity ($\geq 10000\ \Omega$.cm) Si cap wafer is bonded to the glass wafer by using BCB as the adhesive interlayer. Therefore, having frequency-dependent permittivity data of both glass and high-resistivity Si will lead to more correct and reliable designs.

This chapter proposes a novel wideband characterization method to investigate the frequency-dependent nature of the utilized glass and high-resistivity Si wafers. The BCB packaged RF MEMS switches operate at 35 GHz. Although it is possible to use the characterization method for broader frequency bands, this study investigates the frequency-dependent behavior of the substrates in the 1-40 GHz band. The procedure depends on the measurement results of CPW transmission lines on glass and high-resistivity Si wafers. Before going into details with the characterization structures, Section 6.1 presents the general view of the characterization procedure using CPW transmission lines.

6.1 Wideband Characterization Procedure Based on CPW Transmission Line Measurements

The wideband characterization method aims to obtain frequency-dependent effective permittivity of substrate materials, which carry some test structures. Specifically, the BCB packaged RF MEMS switches utilize glass and high-resistivity Si wafers. Therefore, the method targets to obtain frequency-dependent permittivity data and observe the dispersive behavior of the glass and high-resistivity Si. The characterization method bases on measured S-parameters of CPW transmission lines. Although other test structures might be utilized, CPW transmission lines prove worthy owing to their simplicity in fabrication and modeling. Moreover, CPW transmission lines are the basis for the BCB packaged RF MEMS switches.

The itemized procedure for the wideband characterization method is as follows:

- The S-parameter measurements of the test structures (CPW transmission lines) fabricated on glass and high-resistivity Si wafers,
- Piecewise circuit modeling of the CPW transmission lines based on measured S-parameters. Obtaining TL models (Z_0, ε_{eff}, loss and the center frequency of corresponding window (f_c)) by simultaneously solving three identical transmission lines with different physical lengths. Simplex algorithm of AWR Microwave Office is utilized for this purpose,
- Utilizing analytical formulations, based on conformal mapping techniques, to obtain frequency-dependent electrical permittivity of the utilized substrate material.

Furthermore, the same procedure is applied to EM simulation results of CPW transmission lines. Therefore, a comparison can be made on electrical permittivity data of the EM models and the measurement results, which reveals the dispersion characteristics of the substrates. Section 6.1.1, Section 6.1.2 and Section 6.1.3 present the elaborated description of each item within the within the wideband piecewise characterization procedure.

6.1.1 Fabrication and S-Parameter Measurements of CPW Transmission Lines

CPW transmission lines are fabricated on 4” glass and high-resistivity ($\geq$ 10000 Ω.cm) Si wafers in order to characterize both substrate materials. A Cr/Au (25 nm/1 µm) metal layer is sputtered on both wafers and patterned by the use of a photolithography step and wet etching.

There are four sets of CPW transmission lines, in which transmission lines with three different physical lengths exist. There are two 50 Ω CPW transmission line sets. One of them is designed for glass wafers, and the other set is designed for high-resistivity silicon wafers. Furthermore, there are 75 Ω CPW transmission line sets. One of the sets is designed for glass wafers, and the other set is designed for high-resistivity silicon wafers. Figure 6.1 presents the physical dimensions and their abbreviations in the bracelets for a CPW transmission line.

Table 6.1 presents the physical dimensions (Figure 6.1) of the CPW transmission lines for each separate set. The same mask set is fabricated both on high-resistivity silicon wafers and glass wafers. Thus, we would have all of the required test structures with fabricating glass and high-resistivity silicon wafers.

The S-parameter measurements were performed by the use of Cascade Microtech Summit 9000 Analytical Probe Station and Agilent E8361A Vector Network Analyzer (VNA). The VNA is calibrated by a Short-Open-Load-Thru (SOLT) calibration method in 1-40 GHz frequency band, utilizing Cascade 101-190 Impedance Standard Substrate (ISS).

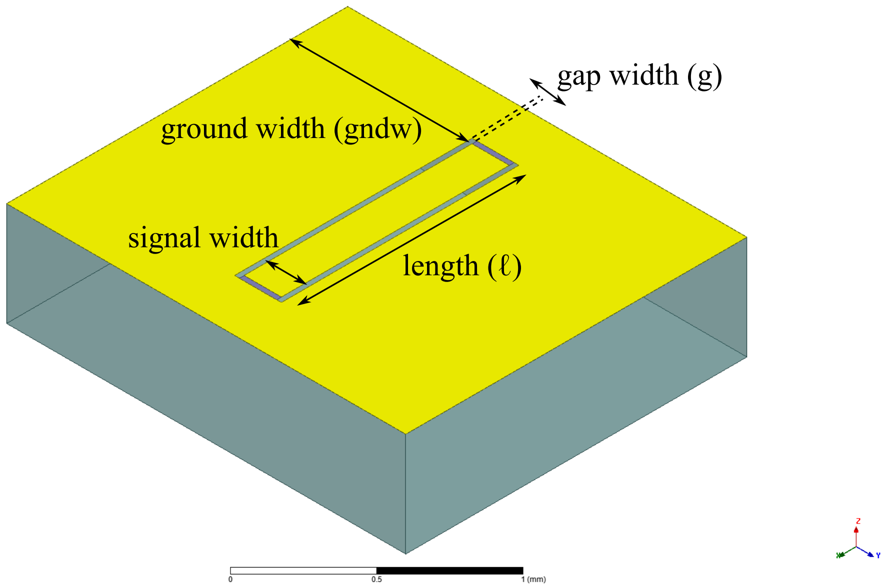

Figure 6.1: Physical dimensions of the CPW transmission line along with their abbreviations within the bracelets.

6.1.2 Piecewise Transmission Line Modeling of Measured S-Parameters

The CAD models simulating the performance of the transmission lines rely on the effective permittivity (ϵ_{eff}), characteristic impedance (Z_0), and loss of the system. The standard procedure for the characterization of these transmission lines is to pursue a single value for the transmission line parameters within the entire frequency band. In other words, simple CAD models neglect the frequency dependency of the parameters, such as effective permittivity. The measurement equipment at hand dictates the frequency band of operation, which is 1-40 GHz for BCB packaged RF MEMS switches and characterization structures. The developed piecewise characterization method employs a different approach. Instead of characterizing the material within the entire frequency band in one sweep, the band is split into many windows. Each window has a width of 2 GHz. Then, the method calculates the effective permittivity at the center frequency of each window. Figure 6.2 presents the windowing action and the center frequency point of the moving window. The circuit model parameters of the transmission line from 2 GHz to 39 GHz are then obtained by 1 GHz steps.

For instance, the material parameter values at 2 GHz was characterized by the use

Table 6.1: Dimensions and lengths of the CPW transmission lines for different sets.

	Abbr.	CPW TL 1 (µm)	CPW TL 2 (µm)	CPW TL 3 (µm)
50 Ω (Glass)	ℓ	1920	6866	11902
	s	180	180	180
	g	23	23	23
	gndw	500	500	500
75 Ω (Glass)	ℓ	2120	7066	12102
	s	100	100	100
	g	55	55	55
	gndw	500	500	500
50 Ω (Si)	ℓ	1268	4540	7870
	s	100	100	100
	g	55	55	55
	gndw	500	500	500
75 Ω (Si)	ℓ	2120	7066	12102
	s	40	40	40
	g	100	100	100
	gndw	500	500	500

of measurement results in the 1-3 GHz band. In other words, a piecewise approach is adopted. The 2 GHz wide window moves to higher frequencies in 1 GHz steps. Thus, the center frequency moves in 1 GHz steps, and frequency-dependent parameter values can be obtained. At first glance, it may seem like decreasing the window size may yield better results. Nevertheless, this does not only increase the workload, but it also decreases accuracy. In other words, the windowing system became more unreliable due to unwanted ripples on the measurement data. Due to these ripples, small windows give ambiguous results.

The utilized procedure does not adopt to obtain the permittivity directly from the measured S-parameters. Instead, by using AWR Microwave Office, a transmission line model was fit to the measured S-parameters as the first step. The curve fitting optimization of a transmission line model and the measured S-parameters of a CPW

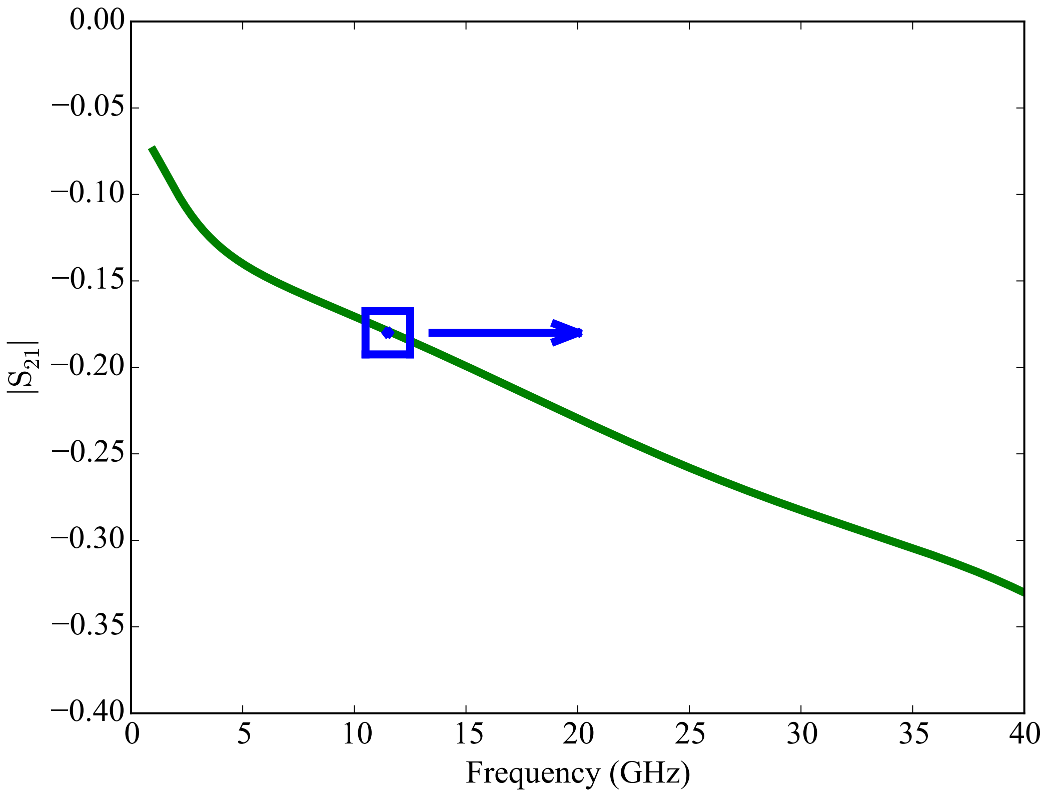

Figure 6.2: A demonstration of the working principle of the piecewise material characterization study based on frequency. A constant width window is moving, while determining the transmission line parameters (Z_0, ϵ_{eff} and loss of the line) on the center frequency of the window.

transmission line gives the model parameters (Z_0, ϵ_{eff}, and loss). The curve fitting is done in 2 GHz windows, and the center frequency of the windows was set as the frequency of the transmission line model.

In order to have more physical (compatible with physical structure) results, three identical transmission lines with different lengths were utilized. The data fitting is done by using the simplex optimization tool of the AWR Microwave Office simultaneously for all three transmission lines. Therefore, the results are more reliable and more physical.

Then, the circuit model parameters (Z_0, ϵ_{eff}, and loss) are utilized in the analytical model formulations, and permittivity of the materials were obtained.

6.1.3 Extracting Frequency Dependent Electrical Permittivity of Substrate Materials

A practical CPW transmission line consists of three metal plates (a signal and two ground planes) staying on top of a dielectric substrate. The center metal acts as the signal strip between two finite-width ground planes. Grounded CPW (GCPW) transmission lines, where there exists a third ground plane at the bottom of the finite-width dielectric substrate, found themselves application areas. The BCB packaged RF MEMS switches studied within this dissertation bases on conventional CPW transmission lines. Therefore, GCPW transmission lines are not the focus of this study. Figure 6.3 present a demonstration of conventional practical CPW transmission lines with finite-width ground planes and dielectric substrates.

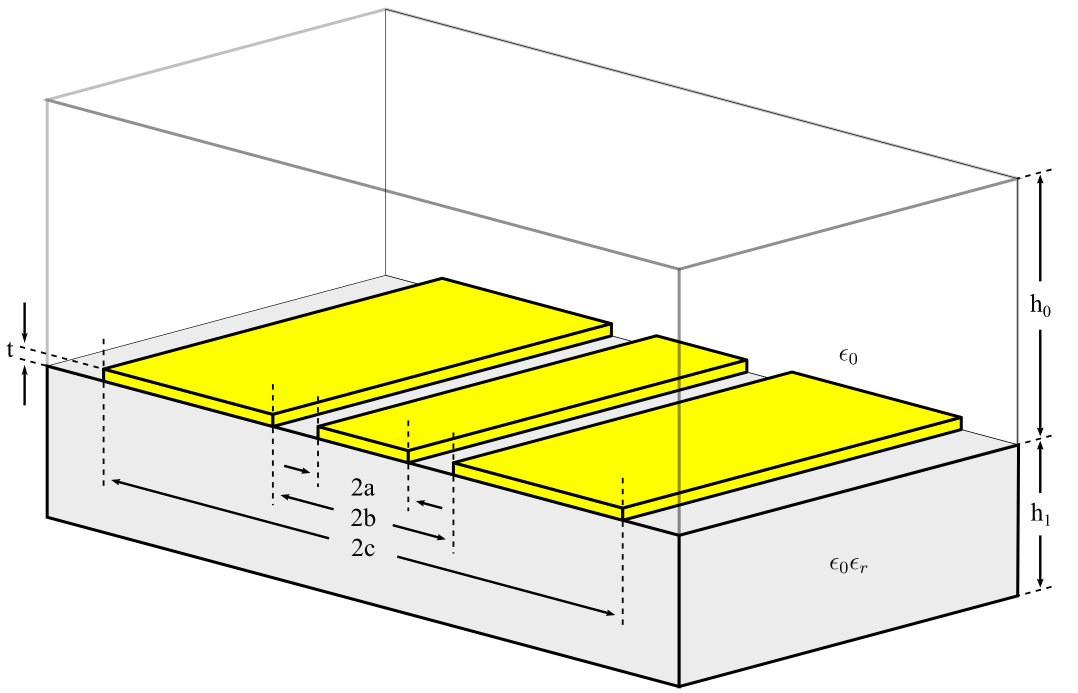

Figure 6.3: Conventional single layer CPW with finite width ground planes.

The wideband characterization procedure for investigating the dispersive nature of the glass and high-resistivity silicon substrates utilizes conventional CPW transmission lines at its basis. The modeling of the CPW transmission lines plays a crucial role in obtaining the frequency-dependent electrical permittivity of the employed dielectric substrates. Conformal mapping techniques based on a propagating quasi-static TEM mode assumption presented closely approximate results in modeling the CPW transmission lines. The total capacitance of the CPW transmission line (C), presented in Figure 6.3, is the sum of the partial capacitances C_air and C_1 of the partial regions indicated in Figure 6.4a and Figure 6.4b, respectively. Equation 6.1 presents this relation between the partial capacitances (C_{air} and C_1) and the total CPW capacitance (C).

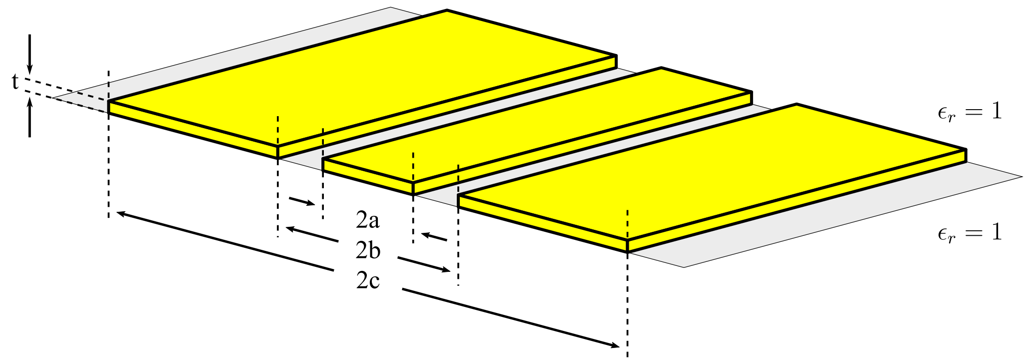

(a)

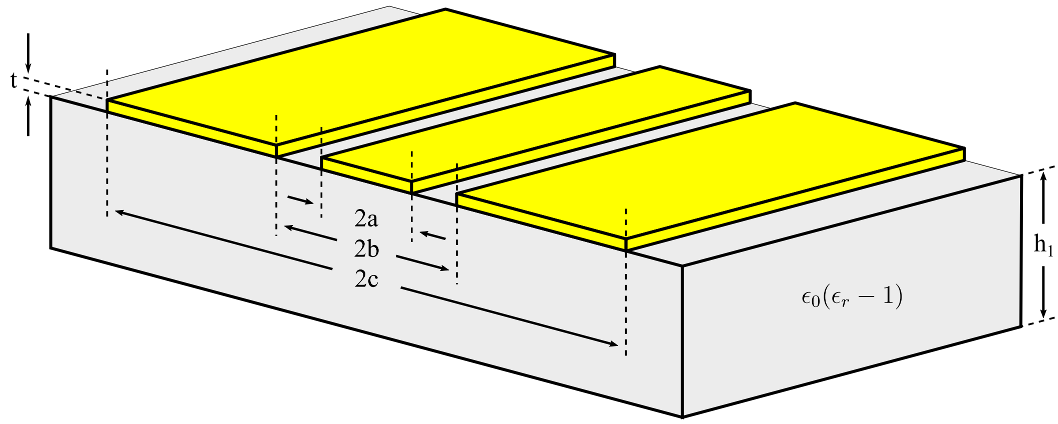

(b)

Figure 6.4: Configurations for finding the capacitance values: (a) C_{air}, (b) C_1.

$$\epsilon_{eff} = \frac{C}{C_{air}} \tag{6.1}$$

By using the quasi-static TEM mode approximation, the effective permittivity of the

CPW transmission lines can be expressed by Equation 6.2.

$$C = C_{air} + C_1 \tag{6.2}$$

The partial capacitance of Figure 6.4a in the absence of the dielectric region can be expressed as in Equation 6.3 by the use of elliptic integrals of the first kind (K). Equation 6.4 and Equation 6.5 present the expressions for the arguments (k and k') of the elliptic integral (K), respectively.

$$C_{air} = 4\epsilon_0 \frac{K(k')}{K(k)} \tag{6.3}$$

$$k = \frac{c}{b}\sqrt{\frac{b^2 - a^2}{c^2 - a^2}} \tag{6.4}$$

$$k' = \sqrt{1 - k^2} \tag{6.5}$$

Equation 6.6 formulates the partial capacitance of the dielectric region (Figure 6.4b) in terms of elliptic integral (K) of first kind, where Equation 6.7 and Equation 6.8 present the expressions for arguments k_1 and k_1', respectively.

$$C_1 = 2\epsilon_0(\epsilon_1 - 1)\frac{K(k_1')}{K(k_1)} \tag{6.6}$$

$$k_1 = \frac{\sinh\left(\frac{\pi c}{2h_1}\right)}{\sinh\left(\frac{\pi b}{2h_1}\right)}\sqrt{\frac{\sinh^2\left(\frac{\pi b}{2h_1}\right) - \sinh^2\left(\frac{\pi a}{2h_1}\right)}{\sinh^2\left(\frac{\pi c}{2h_1}\right) - \sinh^2\left(\frac{\pi a}{2h_1}\right)}} \tag{6.7}$$

As a result of the given formulations, Equation 6.8 presents the relation between the effective permittivity (ϵ_{eff}) and ϵ_1 [49].

$$\epsilon_{eff} = 1 + \frac{\epsilon_1 - 1}{2}\frac{K(k_0')K(k_1)}{K(k_0)K(k_1')} \tag{6.8}$$

From Equation 6.8, Equation 6.9 can be written, where the CPW-dispersive electrical permittivity of the dielectric (glass or high-resistivity silicon) is calculated from.

$$\epsilon_1 = 1 + 2(\epsilon_{eff} - 1)\frac{K(k_0)K(k_1')}{K(k_0')K(k_1)} \tag{6.9}$$

6.2 Calculated Frequency Dependent Permittivity of Glass and High-Resistivity Silicon

The itemized procedure in Section 6.1 is applied for 50 Ω and 75 Ω CPW transmission lines on glass wafer. Firstly, the piecewise transmission line modeling is implemented and the effective permittivity of the 50 Ω and 75 Ω CPW structures on the glass are obtained between 2-39 GHz. Tabulated data points were entered into a python script, where the frequency-dependent electrical permittivity value of the glass was calculated. It should be noted that, obtained electrical permittivity includes the dispersive effects of the CPW transmission line structure and the glass substrate. *Due to the CPW related dispersion effects, these set of values cannot be assumed as the electrical permittivity of the glass substrate. The extracted data will be named as CPW-dispersive electrical permittivity within the context of this thesis.* Nevertheless, obtained permittivity performance, including the dispersive effects of both the CPW structure and the glass substrate itself is valuable. For assessing the substrate related dispersive behavior, EM simulations of the same CPW transmission lines (Table 6.1) were conducted in ANSYS HFSS. The relative electrical permittivity of glass is taken as 4.6 in the EM simulations. This way, only the dispersive behavior of the CPW transmission line structure itself is taken into account. The same piecewise wideband characterization procedure is applied to EM simulation results as well. Therefore, by comparing the EM simulation-based and CPW transmission line measurement-based CPW-dispersive electrical permittivity data, it becomes possible to assess the dispersive behavior of the utilized substrate.

Figure 6.5 presents the obtained frequency-dependent CPW-dispersive electrical permittivity of glass substrates for 50 Ω CPW transmission lines based on both EM simulations and CPW transmission line measurements. Figure 6.6 presents the difference between measurement and simulation-based CPW-dispersive permittivity data.

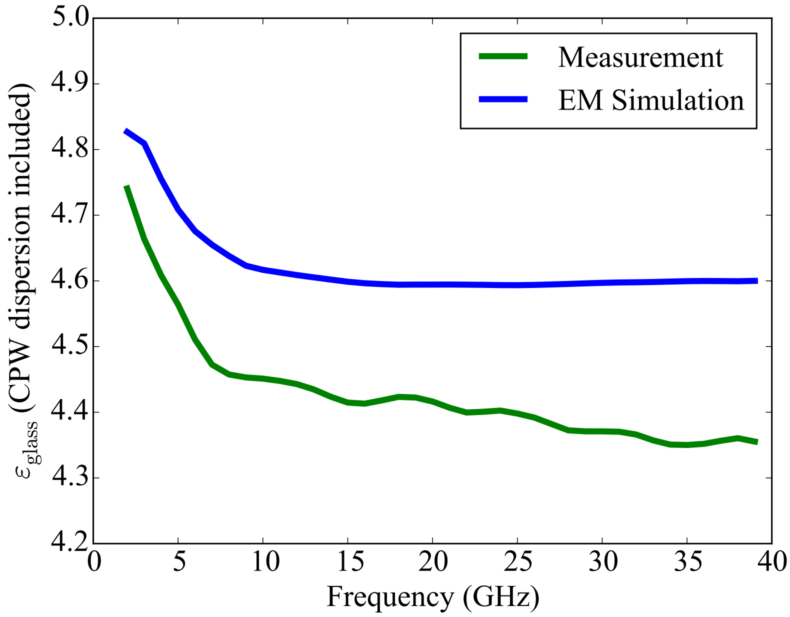

Figure 6.5: Calculated frequency-dependent CPW-dispersive permittivity of glass for the frequency band of 2-39 GHz with 1 GHz steps.

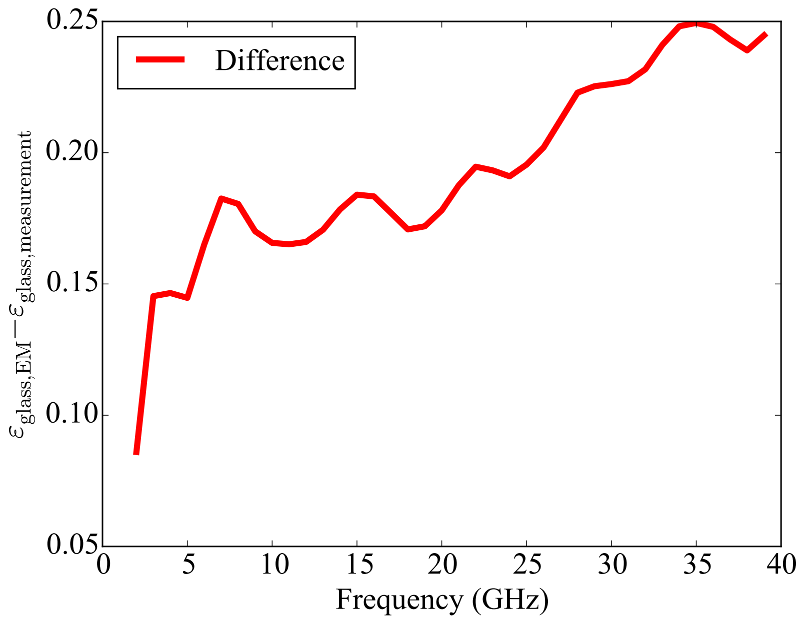

Figure 6.6: The difference between the calculated CPW-dispersive permittivity based on the EM model and the measurements for 50 Ω glass CPW transmission lines.

The primary behavioral difference between the EM simulation-based and measurement-based CPW-dispersive electrical permittivity can be observed better at higher frequencies of the 1-40 GHz band. Figure 6.6 presents the increasing difference between measurement and EM simulation-based data. The difference is due to the dispersive behavior of the glass material. As Figure 6.5 and Figure 6.6 indicate, the electrical permittivity of glass decreases with increasing frequency within the 1-40 GHz frequency band.

Figure 6.7 presents the obtained frequency-dependent CPW-dispersive electrical permittivity of glass substrates for 75 Ω CPW transmission lines based on both EM simulations and CPW transmission line measurements. The difference of the measurement and simulation-based CPW-dispersive electrical permittivity data is presented in Figure 6.8. The results indicate a similar behavior for the glass substrate. If a comparison is made between Figure 6.5 and Figure 6.7, the ripples in the 75 Ω seems more dominant. This behavior is due to the increased dispersive behavior of the CPW transmission lines for higher impedances.

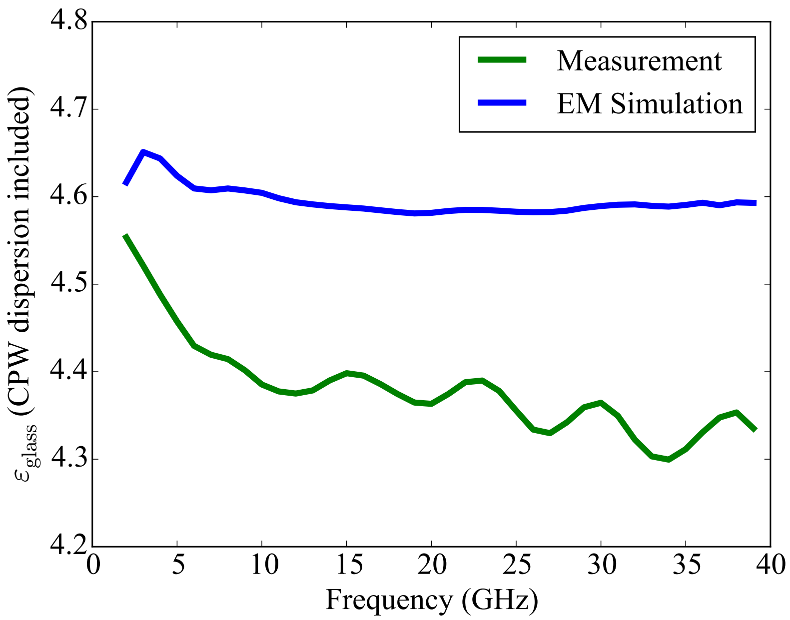

Figure 6.7: Calculated frequency-dependent CPW-dispersive permittivity of glass for the frequency band of 2-39 GHz with 1 GHz steps.

Precisely the same procedure is applied with the 50 Ω and 75 Ω CPW transmis-

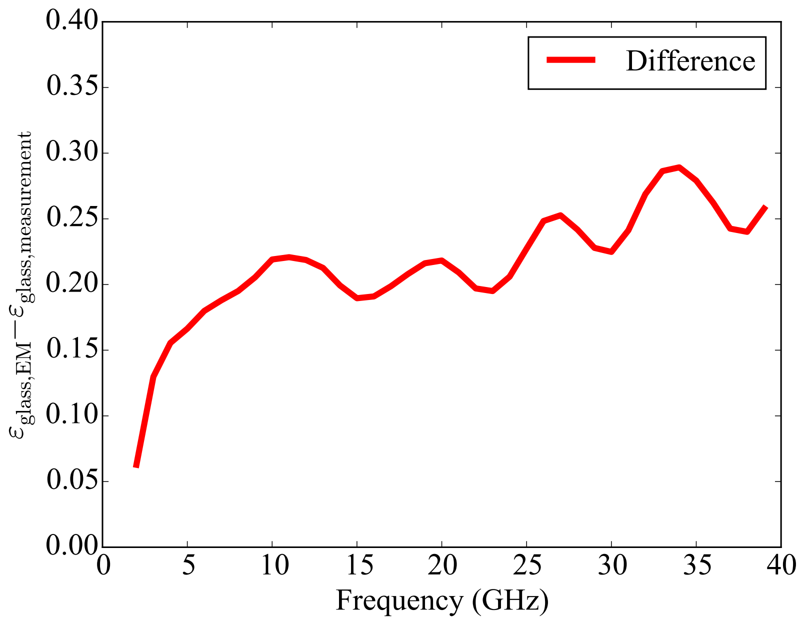

Figure 6.8: The difference between the calculated CPW-dispersive permittivity based on the EM model and the measurements for 75 Ω glass CPW transmission lines.

sion lines on high-resistivity silicon substrates. The relative electrical permittivity of high-resistivity silicon is taken as 11.9 in the EM simulations. Similar behaviors are observed for high-resistivity silicon wafers as in the case of glass substrates. Figure 6.9 presents the obtained frequency-dependent CPW-dispersive electrical permittivity of high-resistivity silicon substrates for 50 Ω CPW transmission lines based on both EM simulations and CPW transmission line measurements. The difference of the measurement and simulation-based CPW-dispersive electrical permittivity data is presented in Figure 6.10.

Moreover, Figure 6.11 presents the obtained frequency-dependent CPW-dispersive electrical permittivity of high-resistivity silicon substrates for 75 Ω CPW transmission lines based on both EM simulations and CPW transmission line measurements. The difference of the measurement and simulation-based CPW-dispersive electrical permittivity data is presented in Figure 6.12. Regarding the obtained data from both 50 Ω and 75 Ω CPW transmission lines, the electrical permittivity of high-resistivity silicon decreases with increasing frequency within 1-40 GHz frequency band. The case with the high-resistivity silicon is identical to the case with glass.

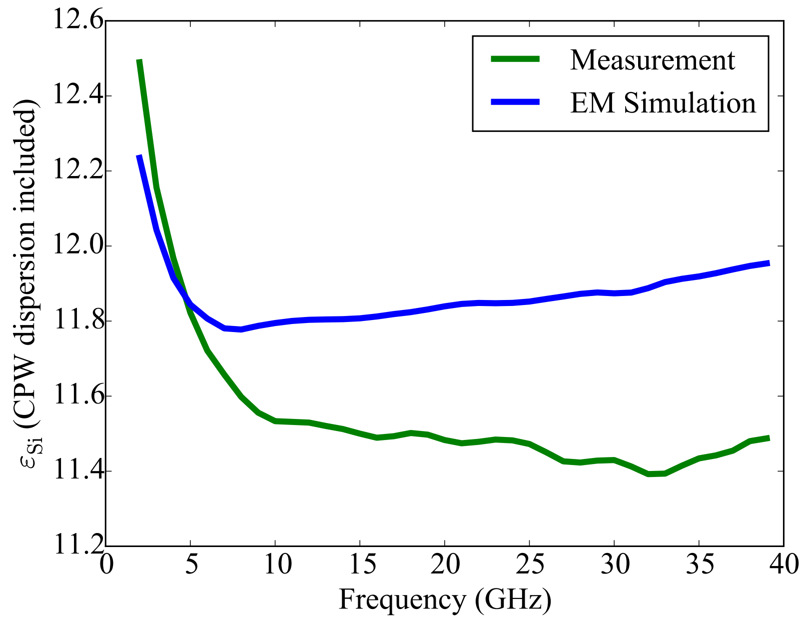

Figure 6.9: Calculated frequency-dependent CPW-dispersive permittivity of glass for the frequency band of 2-39 GHz with 1 GHz steps.

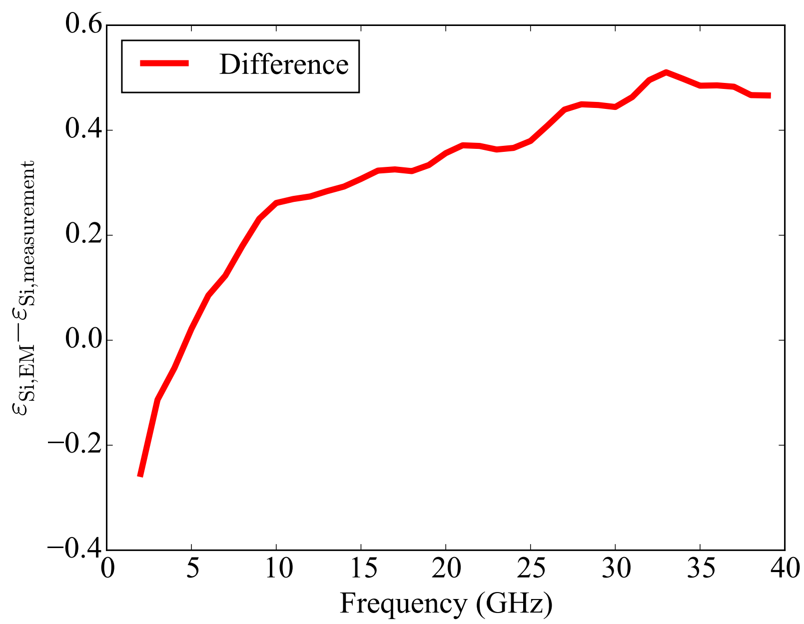

Figure 6.10: The difference between the calculated CPW-dispersive permittivity based on the EM model and the measurements for 50 Ω silicon CPW transmission lines.

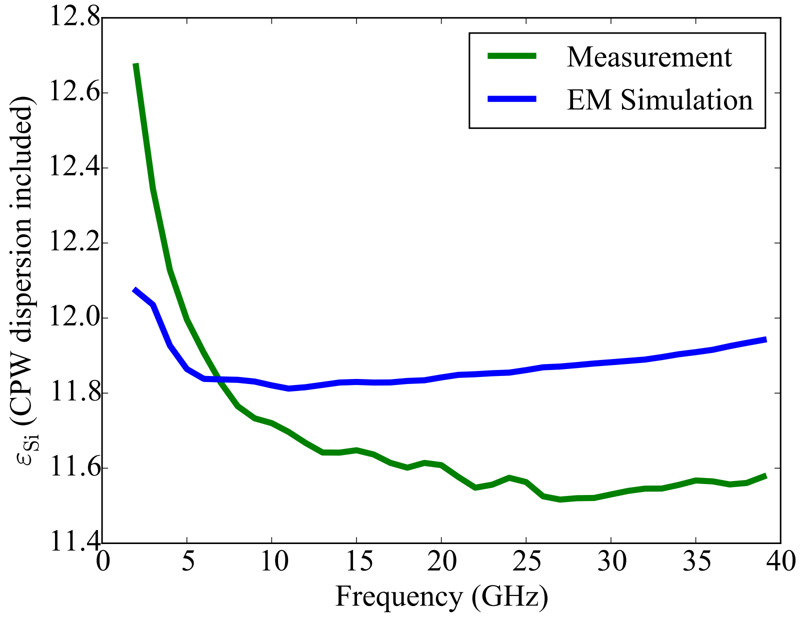

Figure 6.11: Calculated frequency-dependent CPW-dispersive permittivity of glass for the frequency band of 2-39 GHz with 1 GHz steps.

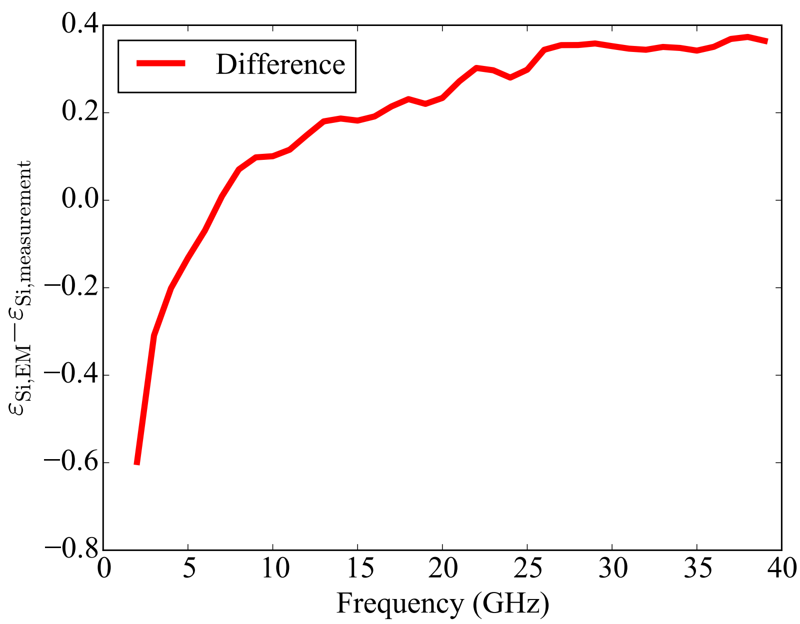

Figure 6.12: The difference between the calculated CPW-dispersive permittivity based on the EM model and the measurements for 75 Ω silicon CPW transmission lines.

CHAPTER 7

CONCLUSION AND FUTURE WORK

This thesis presents separate studies which aim to develop, characterize, and assess a zero-level packaging concept, which utilizes BCB as the bonding interlayer between the glass and high-resistivity silicon wafers. The first study focuses on the development of the BCB packaging concept. Package development includes the EM design of the package structure, construction of the packaging process steps and integration of the packaging process to METU RF MEMS switch fabrication cycle. The initial step in developing the zero-level packaging concept was to investigate the processibility and RF performance of the package structure. These two considerations were studied simultaneously, and both influenced each other. As a result of the performed development studies, the packaging concept was implemented on simple CPW transmission lines. The comparison between the EM simulation results and the RF performance of the packaged CPW transmission lines, especially the planar transition regions, indicated a proper matching with each other. The application of the packaging concept to the RF MEMS switch, on the other hand, proved to be much more challenging. The switch fabrication process underwent some changes during the integration with the developed packaging process. As a result, a new switch fabrication process was designed to make the RF MEMS bridges (sandwiched bridge structure) compatible with the harsh packaging process step. The second study complemented the first study by characterizing the package structure in terms of its RF performance. A circuit model of the BCB packaged CPW transmission line revealed the effects of individual sections of the package structure. Moreover, a novel piecewise wideband characterization method proved the dispersive nature of the glass and the high-resistivity silicon wafers. The technique utilizes various CPW transmission lines on glass and high-resistivity silicon wafers as samples and provides a frequency-dependent electrical permittivity in wideband. The third study explores the process sensitivity of the developed package structure based on EM simulation results. The sensitivity analysis investigates the package in respect to BCB thickness, BCB lane width, $\mathrm{Si_xNi_y}$ thickness, cavity depth, and BCB relative permittivity variations, by perturbing these parameters around the nominal process parameters. Although all the parameters are individually perturbed, a worst-case scenario for the package is studied and presented.

The following items present conclusions concerning the studies performed within the scope of this thesis:

1. A zero-level packaging concept, in which a high-resistivity silicon wafer is bonded to a glass device wafer by the use of BCB as the bonding interlayer is developed. The thesis presents a design procedure of the developed packaging methodology.

2. The zero-level packaging is realized, and the process steps are optimized for a robust, repeatable, and efficient fabrication cycle. Furthermore, the packaging process cycle is integrated with METU RF MEMS switch fabrication process. As a result, a 4" complete fabrication cycle to obtain zero-level packaged RF MEMS switch which utilizes nine masks is developed. Although the packaging is implemented with CPW transmission lines and an RF MEMS switch, the concept is not limited with these two relatively simple structures. This packaging approach applies to much more complex RF MEMS components as well.

3. A circuit model containing cascaded transmission lines proved to be useful in exploring the effects of the package parts on the RF performance. Employing packaged CPW transmission line measurement results, curve fitting algorithms optimized the circuit model parameters. The impact of the planar transmission regions on the insertion loss performance of the packaged CPW transmission lines is the most critical loss factor. The BCB and high-resistivity silicon layers on top of the planar transitions contributed to the insertion loss of the packaged component.

4. The packaging methodology is applied to package a 35 GHz shunt, capacitive

contact RF MEMS switch. The thesis presents many attributes of the package and the switch by using various analysis.

- The endurance analysis consists of the shear strength measurements for the bonded caps on top of RF MEMS switches. The packaged switches require 21 N average force for the detachment of the caps. A $\mathrm{Si_xN_y}$ layer between the BCB ring and the gold layer of the CPW structures enhanced the adhesion between these layers. This enhanced adhesion increased the shear strength of the BCB package, where similar studies lack this advantage.
- A comparison between the optical profiler measurements of the MEMS bridges before and after the BCB packaging revealed the amount of center deflection due to the harsh packaging process conditions. 71 nm average center deflection is noted among three packaged switches. The alterations in the METU RF MEMS switch fabrication, sandwiched gold bridge between $\mathrm{Si_xN_y}$, for the integration of packaging process steps bear fruit in this regard.
- A comparative actuation analysis by the use of C-V measurements before and after the packaging indicated a 3.9 V average increase in the actuation voltages. The BCB bonding process, which takes place at 250 $^\circ\mathrm{C}$, effected the mechanical structure of the MEMS bridges slightly.
- S-parameter measurements indicated the expected RF performance of the packaged RF MEMS switches. The nine packaged switches have similar and repeatable performances. The worst performing switch in the upstate (q2c9r1) has 20.7 dB return loss and around 0.4 dB insertion loss at 35 GHz. Moreover, the worst-performing switch in the downstate (q3c7r1) demonstrated 24.6 dB isolation at 35 GHz.
- The transient analysis presented the switching times for the RF MEMS switches. The switch has a 3.5 µs fall-time (upstate to downstate) and 10 µs rise-time (downstate to upstate). Together with the five µs delay between the application of the bias signal and the response of the switch, there is a total of 8.5 µs fall-time (upstate to downstate).
- The BCB packaged RF MEMS switch performed for a total time of 472

hours, where the switch stays at downstate for 236 hours. During the lifetime tests, the switch performed for 10.2 billion cycles. The duty cycle of the signal decreased to 31.4 $\%$ at the end of 472 hours of operation from 50.6 $\%$. The tests ended due to a power blackout, which means the switch could have performed more.

5. A piecewise wideband characterization method is developed and applied for determining the dispersive nature of the glass and the high-resistivity silicon wafers. The method solely depends on CPW transmission lines as test structures and compares the frequency-dependent electrical permittivity data of EM simulations and transmission line measurements. The dispersive nature of the utilized substrate becomes obvious. This method come forward among the similar work, due to its dependence on measurement results and its easy application to any substrate.

The derived conclusions from the studied subjects can be improved further by the following future work assignments:

- Various aspects of the BCB packaging fabrication steps might be improved. For instance, just by increasing the thickness of the BCB layer, the dielectric loading effect on the planar transition regions might be decreased. Furthermore, the step-up coverage of the BCB layer would increase with the outlined change.
- Although lifetime tests indicated 10.2 billion cycles of switching operation, a hermeticity test is not applied to the BCB packaged RF MEMS switch. Therefore, there is no absolute leak rate value for the BCB package. Hermeticity tests for the BCB packaged RF MEMS switches may be performed.
- The packaged RF MEMS switch occupies an area of 1.70×1.22 mm^2. Although the BCB packaging method was studied on small components, there is no electrical restriction in the utilization of the package for larger chips or components. A more complex RF MEMS component, such as a phase shifter, might be packaged with the developed packaging methodology.
- The piecewise wideband characterization method might be improved by modeling and extracting the dispersive behavior of the CPW transmission lines from

the obtained frequency-dependent electrical permittivity data. By this way, the frequency-dependent electrical permittivity of a material may be available to be used as a material definition within EM solvers.

- The piecewise wideband characterization method might be extended to include conductor and dielectric loss effects. By this way not only the electrical permittivity but also the frequency-dependent tangent loss of a dielectric may be determined.

- The dispersive behavior of the glass, high-resistivity silicon or any other material might be investigated. A physical and mathematical model would prove useful in the utilization of these materials.

REFERENCES

[1] G. Rebeiz, *RF MEMS: Theory, Design and Technology*, New Jersey: John Wiley and Sons Publication, 2003.

[2] Z. J. Yao, S. Chen, S. Eshelman, D. Denniston, and C. Goldsmith, "Micromachined low-loss microwave switches," *J. Microelectromech. Syst.*, vol. 8, pp. 129–134, 1999.

[3] J. B. Muldavin and G. M. Rebeiz, "High-isolation CPW MEMS shunt switches: Modeling and design," *Microwave Theory and Techniques, IEEE Transactions* on, vol. 48, pp. 1045-1056, 2000.

[4] R. E. Mihailovich, M. Kim, J. B. Hacker, E. A. Sovero, J. Studer, J. A. Higgins, and J. F. DeNatale, "MEM relay for reconfigurable RF circuits," *Microwave and Wireless Components Letters, IEEE*, vol. 11, pp. 53-55, 2001.

[5] S. Majumder, J. Lampen, R. Morrison, and J. Maciel, "A packaged, high-lifetime ohmic MEMS RF switch," in *IEEE MTT-S Int. Microwave Symp. Dig.*, 2003, vol. 3, pp. 1935–1938.

[6] H. C. Lee, J. Y. Park, and J. U. Bu, "Piezoelectrically actuated RF MEMS DCcontact switches with low voltage operation," *IEEE Microwave Wireless Component Letters*, vol. 15,no. 4, pp. 202–204, Apr. 2005.

[7] J. Lampen, S. Majumder, R. Morrison, A. Chaudhry, and J. Maciel, "A wafer-capped, high-lifetime ohmic MEMS RF switch," *Int. J. RF Microw. Comput. Aided Eng.*, vol. 14, no. 4, pp. 338–344, 2004.

[8] S. Duffy, C. Bozler, S. Rabe, J. Knecht, L. Travis, P. Wyatt, C. Keast, and M. Gouker, "MEMS microswitches for reconfigurable microwave circuitry," *Microwave and Wireless Components Letters, IEEE*, vol. 11, pp. 106-108, 2001.

[9] M. Unlu, "Novel impedance tuner, phase shifter, and vector modulators us-

ing RF MEMS technology," Ph.D. dissertation, Dept. Elect. Elec- tron. Eng., Middle East Techn. Univ., Ankara, Turkey, 2009.

[10] M. Unlu, S. Demir, and T. Akin, "A 15-40-GHz Frequency Reconfigurable RF MEMS Phase Shifter," *IEEE Transactions on Microwave Theory and Techniques*, vol. 61, no. 8, pp. 2865–2877, Aug. 2013.

[11] S. Barker and G. M. Rebeiz, "Distributed MEMS true-time delay phase shifters and wide-band switches," *IEEE Trans. Microw. Theory Tech.*, vol. 46, pp. 1881–1889, November 1998.

[12] G. Bartolucci, S. Catoni, F. Giacomozzi, R. Marcelli, B. Margesin and D. Pochesci, G. Bartolucci, S. Catoni, and F. Giacomozzi, "Realization of distributed RF MEMS phase shifter with very low number of switches," *Electro. Lett.*, vol. 43, pp. 1290-1292, November 2007.

[13] F. Maury, A. Pothier, J. C. Orlianges, D. Mardivirin, T. Reveyrand, and F. Conseil, "Ku band DMTL medium power phase shifters," *IEEE MTT-S Int. Microwave Symp. Dig.*, 7-12 June 2009, pp. 1153-1156.

[14] H. A. C. Tilmans et al., "Wafer-level packaged RF-MEMS switches fabricated in a CMOS fab," in *International Electron Devices Meeting. Technical Digest (Cat. No.01CH37224)*, 2001, pp. 41.4.1-41.4.4.

[15] A. Jourdain, H. Ziad, P. D. Moor, and H. A. C. Tilmans, "Wafer-scale 0-level packaging of (RF-)MEMS devices using BCB," in *Symposium on Design, Test, Integration and Packaging of MEMS/MOEMS 2003.*, 2003, pp. 239-244.

[16] W. M. van Spengen, P. Czarnecki, R. Puers, J. T. M. van Beek, and I. D. Wolf, "The influence of the package environment on the functioning and reliability of RF-MEMS switches," in 2005 *IEEE International Reliability Physics Symposium, 2005. Proceedings. 43rd Annual.*, 2005, pp. 337-341.

[17] U. Zaghloul, G. Papaioannou, B. Bhushan, F. Coccetti, P. Pons, and R. Plana, "On the reliability of electrostatic NEMS/MEMS devices: Review of present knowledge on the dielectric charging and stiction failure mechanisms and novel characterization methodologies," *Microelectronics Reliability*, vol. 51, no. 9-11, pp. 1810-1818, Sep. 2011.

[18] I. Comart, C. Cetintepe, E. Sagiroglu, S. Demir, and T. Akin, "Development and Modeling of a Wafer-Level BCB Packaging Method for Capacitive RF MEMS Switches," *Journal of Microelectromechanical Systems*, vol. 28, no. 4, pp. 724–731, Aug. 2019.

[19] A. Jourdain, K. Vaesen, J. M. Scheer, J. W. Weekamp, J. T. M. van Beek, and H. A. C. Tilmans, "From zero- to second-level packaging of RF-MEMS devices," in *18th IEEE International Conference on Micro Electro Mechanical Systems, 2005. MEMS 2005.*, Miami Beach, FL, USA, pp. 36-39.

[20] K. D. Leedy, R. E. Strawser, R. Cortez, and J. L. Ebel, "Thin-film encapsulated RF MEMS switches," *J. Microelectromech. Syst.* vol. 16, no. 2, pp. 304-309, Apr. 2007.

[21] I. Forehand and C. L. Goldsmith, "Wafer level micropackaging for RF MEMS switches," in *Proc. IPACK*, San Francisco, CA, USA, 2005, pp. 1-5.

[22] F. Barriere, A. Pothier, A. Crunteanu, M. Chatras, and P. Blondy, "A zero-level packaged RF-MEMS switch with large contact force," in *Proc. 41st Eur. Microw. Conf. (EuMC)*, Oct. 2011, pp. 1229-1232.

[23] F. Barriere, A. Crunteanu, A. Bessaudou, A. Pothier, F. Cosset, D. Mardivirin, et al., "Zero-level metal thin film package for RF MEMS," in *Proc. Topical Meeting Silicon Monolithic Integr. Circuits RF Syst. (SiRF)*, Jan. 2010, pp. 148-151.

[24] I. Comart, "Zero-Level packaging of microwave and millimeterwave MEMS components," M.S. Thesis, Dept. Electrical and Electronics Eng., Middle East Technical Uni., Cankaya, Turkey 2010

[25] E. S. Topalli, K. Topalli, S. E. Alper, T. Serin, and T. Akin, "Pirani Vacuum Gauges Using Silicon-on-Glass and Dissolved Wafer Processes for the Characterization of MEMS Vacuum Packaging," *IEEE Sensors J.*, vol. 9, no. 3, pp. 263-270, Mar. 2009.

[26] R. Knechtel, "Glass frit bonding: A universal technology for wafer level encapsulation and packaging," *Microsyst. Technol.*, vol. 12, nos. 1-2, pp. 63-68, Dec. 2005.

[27] M. Fujii, I. Kimura, T. Satoh, and K. Imanaka, "RF MEMS switch with wafer level package utilizing frit glass bonding," in *Proc. 32nd Eur. Microw. Conf.*, 2002, pp. 1–3.

[28] I. Comart, K. Topalli, S. Demir, and T. Akin, "Microwave Characterization of a Wafer-Level Packaging Approach for RF MEMS Devices Using Glass Frit Bonding," *IEEE Sensors Journal*, vol. 14, no. 6, pp. 2006-2011, Jun. 2014.

[29] F. Souchon, D. Saint-Patrice, J. L. Pornin, D. Bouchu, C. Baret, nd B. Reig, "Thin Film Package Redundancy RF MEMS Switches for Space Applications, " *Transducers 2017..*

[30] G. Wu, D. Xu, B. Xiong, Y. Wang, and Y. Ma, "Wafer-level vacuum packaging for MEMS resonators using glass frit bonding," *J. Microelectromech. Syst.,*, vol. 21, no. 6, pp. 1484-1490, Dec. 2012.

[31] P. Pieters, "Wafer level packaging of micro/nanosystems," in Proc. *5th IEEE Conf. Nanotechnol.*, vol. 1, Jul. 2005, pp. 130-133.

[32] D. Peyrou, P. Pons, A. Nicolas, J. w Tao, H. Granier, and R. Plana, "Foturan Cap and BCB Sealing-Ring for RF MEMS Packaging Applications," in *2006 European Microwave Integrated Circuits Conference*, 2006, pp. 456-459.

[33] S. Seok, N. Rolland, and P. A. Rolland, "A Novel Zero-Level Packaging Using BCB Adhesive Bonding and Glass Wet-Etching for Millimeter-Wave Applications," *TRANSDUCERS 2007 - 2007 International Solid-State Sensors, Actuators and Microsystems Conference*, 2007, pp. 2099-2102.

[34] G. J. Carchon, A. Jourdain, O. Vendier, J. Schoebel, and H. A. C. Tilmans, "Integration of 0/1-Level Packaged RF-MEMS Devices on MCM-D at Millimeter-Wave Frequencies," *IEEE Transactions on Advanced Packaging*, vol. 30, no. 3, pp. 369-376, Aug. 2007.

[35] A. Jourdain, X. Rottenberg, G. Carchon, and H. A. C. Tilmans, "Optimization of 0-level packaging for RF-MEMS devices," in *TRANSDUCERS, Solid-State Sensors, Actuators and Microsystems, 12th International Conference on, 2003*, 2003, vol. 2, pp. 1915-1918 vol. 2.

[36] X. Li, Z. Liu, Z. Wang, Y. Huang, and L. Li, "A pre-shaped wafer level packing strategy for RF MEMS," in *2010 11th International Conference on Electronic Packaging Technology High Density Packaging*, 2010, pp. 135-137.

[37] C. Cetintepe, E. S. Topalli, S. Demir, O. A. Civi, and T. Akin, "A fabrication process based on structural layer formation using Au–Au thermocompression bonding for RF MEMS capacitive switches and their performance," *International Journal of Microwave and Wireless Technologies*, vol. 6, no. 05, pp. 473-480, Oct. 2014.

[38] O. D. Gurbuz, S. Demir, and T. Akin, "Reliability Improvement of RF MEMS devices based on lifetime measurements," M.S. Thesis, Dept. Electrical and Electronics Eng., Middle East Technical Uni., Cankaya, Turkey 2010.

[39] W. Zhou, J. He, X. He, H. Yu, and B. Peng, "Dielectric charging induced drift in micro device reliability-a review," *Microelectronics Reliability*, vol. 66, pp. 1-9, Nov. 2016.

[40] W. M. van Spengen, P. Czarnecki, R. Puers, J. T. M. van Beek, and I. D. Wolf, "The influence of the package environment on the functioning and reliability of RF-MEMS switches," in *2005 IEEE International Reliability Physics Symposium, 2005. Proceedings, 43rd Annual.*, 2005, pp. 337-341.

[41] A. Jourdain, P. D. Moor, K. Baert, I. D. Wolf, and H. A. C. Tilmans, "Mechanical and electrical characterization of BCB as a bond and seal material for cavities housing (RF-)MEMS devices," *J. Micromech. Microeng.*, vol. 15, no. 7, p. S89, 2005.

[42] A. Jourdain, P. D. Moor, S. Pamidighantam, and H. A. C. Tilmans, "Investigation of the hermeticity of BCB-sealed cavities for housing (RF-)MEMS devices," in *Technical Digest. MEMS 2002 IEEE International Conference. Fifteenth IEEE International Conference on Micro Electro Mechanical Systems (Cat. No.02CH37266)*, 2002, pp. 677-680.

[43] A. Jourdain, H. Ziad, P. D. Moor, and H. A. C. Tilmans, "Wafer-scale 0-level packaging of (RF-)MEMS devices using BCB," in *Symposium on Design, Test, Integration and Packaging of MEMS/MOEMS 2003.*, 2003, pp. 239–244.

[44] Kim K., J. Kim M., and Kim J. M., "Packaging method for RF MEMS devices using LTCC capping substrate and BCB adhesive bonding," *IEEE 13th International Conference on Solid-State Sensors, Actuators and Microsystems*, Seoul, Korea, June 2005, pp. 1092-1095.

[45] A. Jourdain, S. Brebels, W. De Raedt, and H. A. C. Tilmans, "Influence of 0-level Packaging on the Microwave Performance of RF-MEMS Devices," in *European Microwave Conf., London, 2001*, pp. 403-406, 419.

[46] J. Zhang and T. Y. Hsiang, "Dispersion Characteristics of Coplanar Waveguides at Subterahertz Frequencies," Journal of Electromagnetic Waves and Applications, vol. 20, no. 10, pp. 1411–1417, Jan. 2006.

[47] P. Seiler, B. Klein, and D. Plettemeier, "Analytical and experimental investigation of substrate permittivity and loss up to 67 GHz," in *The 20th Asia-Pacific Conference on Communication (APCC2014)*, 2014, pp. 123–128.

[48] M. D. Janezic and D. F. Williams, "Permittivity characterization from transmission-line measurement," in *1997 IEEE MTT-S International Microwave Symposium Digest*, 1997, vol. 3, pp. 1343–1346 vol.3.

[49] P. Majumdar and A. K. Verma, "CAD models of dispersion and losses for multilayer coplanar waveguide," in *2016 Asia-Pacific Microwave Conference (APMC)*, 2016, pp. 1–4.

[50] A. K. Verma, P. Singh, and R. Bansal, "Computation of static and frequency-dependent line parameters of multilayer CPW using static SDA and single layer reduction method: Static and Frequency Frequency-Dependent Line Parameters," *International Journal of RF and Microwave Computer-Aided Engineering*, vol. 24, no. 1, pp. 18–29, Jan. 2014.

[51] C. D. Abeyrathne, M. N. Halgamuge, P. M. Farrell, and E. Skafidas, "Performance Analysis of On-Chip Coplanar Waveguide for In Vivo Dielectric Analysis," *IEEE Transactions on Instrumentation and Measurement*, vol. 62, no. 3, pp. 641–647, Mar. 2013.

[52] S. Gevorgian, T. Martinsson, A. Deleniv, E. Kollberg, and I. Vendik, "Simple and accurate dispersion expression for the effective dielectric constant of

coplanar waveguides," *Antennas and Propagation IEEE Proceedings - Microwaves*, vol. 144, no. 2, pp. 145–148, Apr. 1997.

[53] T. Chen, L. Wang, G. Goodyear, A. Yializis, and H. Xin, "Broadband Microwave Characterization of Nanostructured Thin Film With Giant Dielectric Response," *IEEE Transactions on Microwave Theory and Techniques*, vol. 63, no. 11, pp. 3768–3774, Nov. 2015.

[54] C. Cetintepe, "Development of MEMS Technology Based Microwave and Millimeter-Wave Components," M.S. Thesis, Dept. Electrical and Electronics Eng., Middle East Technical Uni., Cankaya, Turkey 2010.

[55] G. M. Rebeiz, K. Entesari, I. Reines, S.-J. Park, M. El-Tanani, A. Grichener, and A. Brown, "Tuning in to RF MEMS," in *IEEE MTT-S Int. Microw. Symp. Dig.*, Oct. 2009, vol. 10, no. 6, pp. 55–72.

[56] F. Solazzi, "Novel Design Solutions for High Reliability RF MEMS Switches," Ph.D. Thesis, University of Trento, 2010.

[57] C. L. Goldsmith, D. I. Forehand, Z. Peng, J. C. M. Hwang, and J. L. Ebel,"High-cycle life testing of RF MEMS switches," in *Proc. IEEE MTT-S Int. Microw. Symp. Dig.*, Jun. 2007, pp. 1805–1808.

[58] B. Pillans, J. Kleber, C. Goldsmith, and M. Eberly, "RF power handling of capacitive RF MEMS devices," in *IEEE MTT-S Int. Microw. Symp. Tech. Dig.*, Jun. 2002, vol. 1, pp. 329–332.

[59] H.S. Newman, J.L. Ebel, D. Judy, and J. Maciel, "Lifetime measurements on a high-reliability RF-MEMS contact switch," *IEEE Microw. Wireless Compon. Lett.*, vol. 18, no. 2, pp. 100–102, Feb. 2008.

[60] A. Grichener and G. M. Rebeiz, "High-reliability RF-MEMS switched capacitors with digital and analog tuning characteristics," *IEEE Trans. Microw. Theory Techn.*, vol. 58, no. 10, pp. 2692–2701, Oct. 2010.

[61] B. Lakshminarayanan, D. Mercier, and G. M. Rebeiz, "High-reliability miniature RF-MEMS switched capacitors," *IEEE Trans. Microw. Theory Tech.*, vol. 56, no. 4, pp. 971–981, Apr. 2008.

[62] D. Mardivirin, A. Pothier, A. Crunteanu, B. Vialle, and P. Blondy, "Charging in dielectricless capacitive RF-MEMS switches," *IEEE Trans. Microw. Theory Tech.*, vol. 57, no. 1, pp. 231–236, Jan. 2009.

[63] Th.G S.M. Rijks, J.T.M. van Beek, P.G. Steeneken, M.J.E. Uleaners, J. De Coster and R.Puers, "RF MEMS Tunable Capacitors with Large Tuning Ratio", *IEEE Maastrich*, January 25-29, 2004, pp.777-780.

CURRICULUM VITAE

PERSONAL INFORMATION

Surname, Name: Comart, İlker
Nationality: Turkish (TC)
Date and Place of Birth: 21.04.1983, Tokat
Marital Status: Married
Email: ilker.comart@metu.edu.tr

EDUCATION

Degree	Institution	Year of Graduation
M.S.	METU Electrical and Electronics Eng.	2010
B.S.	METU Electrical and Electronics Eng.	2007
High School	Nazilli Atatürk Lisesi	2001

PROFESSIONAL EXPERIENCE

Year	Place	Enrollment
2019-Present	ASELSAN Inc.	Senior Engineering Specialist
2018-2019	Prodesa Savunma ve Havacılık Inc.	Electronics Engineer
2016-2018	RFSENS Electronic Biotechnology Inc.	CTO
2012-2016	METU	Scientific Project Expert
2009-2012	METU MEMS Center	Scientific Project Expert
2007-2009	METU	Scientific Project Expert

PUBLICATIONS

- I. Comart, K. Topalli, S. Demir, and T. Akin, "Microwave Characterization of a Wafer-Level Packaging Approach for RF MEMS Devices Using Glass Frit Bonding," in *IEEE Sensors Journal*, vol. 14, no. 6, pp. 2006-2011, Jun. 2014.
- I. Comart, C. Cetintepe, E. Sagiroglu, S. Demir, and T. Akin, "Development and Modeling of a Wafer-Level BCB Packaging Method for Capacitive RF MEMS Switches," *Journal of Microelectromechanical Systems*, vol. 28, no. 4, pp. 724–731, Aug. 2019.

International Conference Publications

- I. Comart, C. Cetintepe, S. Demir, and T. Akin, "A 35 GHz High Isolation RF MEMS SPDT Switch," *The 13th International. Symposium on RF MEMS and RF Microsystems (MEMSWAVE 2012)*, Antalya, Turkey, 2-4 July 2012.
- O. Kilic, I. Comart, S. Demir, and T. Akin, "3-bit CPW Phase Shifter Implemented by a Reduced Branch Line Coupler," *The 13th International. Symposium on RF MEMS and RF Microsystems (MEMSWAVE 2012)*, Antalya, Turkey, 2-4 July 2012.
- O. Bayraktar et al., "RF MEMS based millimeter wave phased array for short range communication," in *2015 9th European Conference on Antennas and Propagation (EuCAP)*, 2015, pp. 1-5.
- İ. Comart, A. Kuzubaşlı, S. K. Sömek, ve B. B. Keskin, "Doğal Kaynak Sularında Escherichia Coli Tespiti için RF MEMS Tabanlı Sensör Çalışmaları," *2. International Water and Health Congress*, Antalya, Turkey, 2017.

National Conference Publications

- K. Topallı, İ. Comart, Ş. Demir, and T. Akın, "RF MEMS Yapıların Glass Frit ile 0-seviye Paketlenmesi," *URSI-Türkiye 2008 4. Bilimsel Kongresi*, s. 110-113

- İ. Comart, Ş. Demir, and T. Akın, "RF MEMS Teknolojisi Tabanlı 12 GHZ ve 26 GHZ Çalışma Frekanslarında Tek Giriş Çift Çıkış Anahtar Yapıları", *URSI Ulusal Konferansi 2010*, (2010).